UNIVERSITY OF CALIFORNIA,
IRVINE

Propagation Characteristics of Magnetostatic Volume Waves and Tunable Microwave Devices in Yttrium Iron Garnet-based Magnonic Metamaterials

DISSERTATION

submitted in partial satisfaction of the requirements
for the degree of

DOCTOR OF PHILOSOPHY

in Electrical Engineering and Computer Science

by

Kai-Hung Chi

Dissertation Committee:
Chancellor's Professor Chen Shui Tsai, Chair
Professor Guann-Pyng Li
Professor Payam Heydari

2014

TABLE OF CONTENTS

LIST OF FIGURES

LIST OF TABLES

ACKNOWLEDGMENTS

I would like to express my special appreciations to my advisor, Chancellor's Professor Chen S. Tsai. Professor Tsai suggested the dissertation topic "Magnonics" to me and has continuously proposed the specific topics treated in the research. He has constantly urged me to obtain better and better research results. Furthermore, he has taught me the right attitudes in facing challenges, that is, dedication, diligence, and never give up, which are priceless. The motto "Nothing is Easy" has sustained me when facing difficulties in all challenges. Professor Tsai is not only my mentor but also my role model for life. I would also like to thank my committee members Professor G. P. Li and Professor Payam Heydari for serving as my committee members even with their extremely busy schedule. I would like to thank Dr. Yun Zhu, who has been working with me on the various projects presented in the dissertation. His skill and knowledge in experiments and microwaves make significant contributions in our joint achievements. I also appreciate Dr. Rongwei Mao. His extensive experience and knowledge in semiconductor fabrication help us to produce a high-quality sample for the experiments. Finally, I would also like to thank Professor Shirley C. Tsai for her encouragement and kindness to me and my family.

A special thanks is due to my family. There is no word that can describe my gratefulness for the unconditional supports and sacrifices of my parents and my mother-in-law. At the end, I would like to thank my beloved wife who accompanies and supports me and shares every moments with me in this journey.

The support of UC DISCOVERY Program and Shih-Lin Electric Corp., USA. are gratefully acknowledged.

CURRICULUM VITAE

Kai-Hung Chi

EDUCATION

Ph.D.in Electrical and Computer Eng. **2014**
Irvine, California

University of California, Irvine

M.S. in Graduate Institute of Photonics and Optoelectronics **2007**
Taipei, Taiwan

National Taiwan University

FIELD OF STUDY

Magnonic Metamaterials: Theorey and Application

JOURNAL PUBLICATIONS RESULTS FROM DISSERTATION RESEARCH

1. **Kai H. Chi**, Yun Zhu, Rong W. Mao, James P. Dolas, and Chen S. Tsai. An approach for analysis of magnetostatic volume waves in magnonic crystals. *Journal of Applied Physics*, 109(7):07D320, March 2011.

2. **Kai H. Chi**, Yun Zhu, Rong W. Mao, S. A. Nikitov, Y. V. Gulyaev, and Chen S. Tsai. Propagation Characteristics of Magnetostatic Volume Waves in One- Dimensional Magnonic Crystals with Oblique Incidence. *IEEE Transactions on Magnetics*, 47(9):3708-3711, 2011.

3. **Kai H. Chi**, Yun Zhu, and Chen S. Tsai. Two-Dimensional Magnonic Crystal With Periodic Thickness Variation in YIG Layer for Magnetostatic Volume Wave Propagation. *IEEE Transactions on Magnetics*,49(3): 1000-1004, 2013.

4. **Kai H. Chi**, Yun Zhu, and Chen S. Tsai. Confinement of Magnetostatic Forward Volume Waves in Two-Dimensional Magnonic Crystals with Line Defects. *Journal of Applied Physics*, 115(17): 17D125, 2014.

5. Y. Zhu, **K. H. Chi**, and C. S. Tsai. Magnonic Crystals-Based Tunable Microwave Phase Shifters. *Applied Physics Letters*, 105(2): 022411, 2014.

JOURNAL PUBLICATION IN ASSOCIATED PROJECTS

1. Yun Zhu, Gang Qiu, **Kai H. Chi**, B. S. T Wang, and Chen S. Tsai. A Tunable X-Band Band-Pass Filter Module Using YIG/GGG Layer on RT/Duroid Substrate. *IEEE Transactions on Magnetics*, 45(10):4195-4198, 2009.

2. Yun Zhu, Gang Qiu, **Kai H. Chi**, B. S. T Wang, and Chen S. Tsai. A Compact XBand Tunable Bandpass Filter Module Using a Pair of Microstrip Composite Bandpass Filters in Cascade. *IEEE Transactions on Magnetics*, 46(6):1424- 1427, 2010.

ABSTRACT OF THE DISSERTATION

Propagation Characteristics of Magnetostatic Volume Waves and Tunable Microwave Devices in Yttrium Iron Garnet-based Magnonic Metamaterials

By

Kai-Hung Chi

Doctor of Philosophy in Electrical Engineering and Computer Science

University of California, Irvine, 2014

Chancellor's Professor Chen Shui Tsai, Chair

The so-called magnonic crystals (MCs), the new metamaterial structures made of periodic variations in geometric parameters and/or properties of magnetic materials, are being actively studied worldwide. In contrast to the well-established photonic crystals (PCs), MCs possess the capability of controlling the generation and transmission of information-carrying magnetostatic waves (MSWs) at microwave frequencies by a bias magnetic field. A new theoretical approach based on Walker's equation which is capable of efficiently analyzing magnetostatic volume waves (MSVWs) propagation characteristics in one-dimensional (1-D) and two-dimensional (2-D) MCs was developed through this dissertation research. The validity of this theoretical approach was subsequently verified by extensive experimental results with excellent agreements.

MC-based tunable microwave devices were also envisaged and realized. Specifically, the performance characteristics of wideband tunable microwave filters and phase shifters, and waveguides, are detailed in this dissertation. In device fabrication, both the 1-D MC consisting of periodic channels and the 2-D MC consisting of periodic holes in square lattices were prepared by wet etching technique. The magnetically-tuned bandgaps created in the 1-D and 2-D MCs were shown to function as tunable band stop filters (BSFs). Furthermore, the large phase shifts associated with the left and right flat passbands of the bandgap facilitated construction of tunable wideband microwave phase shifters. Compared to all existing magnetically-tuned phase shifters, the MC-based phase shifters are significantly smaller in dimension and possess much larger phase tuning rate and phase shifts. Finally, confinement of magnetostatic forward volume waves (MSFVWs) was demonstrated both theoretically and experimentally.

Chapter 1

Introduction

1.1 Theoretical Analysis of Magnonic Crystals and Applications

Magnonic crystals (MCs) are metamaterial structures with periodic variations in geometrical structure and/or material property of magnetic materials. It is a new and emerging research field actively studied in recent years [1–11]. Prof Chen S. Tsai is one of the pioneers in this research field[1–3]. MCs has attracted a great deal of attention worldwide lately because it possesses the capability of controlling the generation and propagation of information-carrying magnetostatic waves (MSWs) in the microwave frequency ranges analogous to control of light in photonic crystals (PC) in the optical frequency regime. In contrast to the optical bands in the conventional PCs

[12, 13], the bandgaps of the MCs can be tuned by bias magnetic fields, and thus tunable microwave devices such as filters, phase shifters, and waveguides could be envisaged and constructed. Typically, there are three major types of periodic structures in constructing the MCs: periodic structure of different magnetic materials [14–19], periodic dots or antidots [4, 20–25], and periodic magnetic film geometries [2, 3, 9, 26–30]. Other types of MC, e.g. using periodic variation of bias magnetic fields was also reported [31]. Up to now, research efforts on MCs are still concentrated on design, analysis, and verification of the bandgap and propagation characteristics. Various analytical approaches have been employed for studying the propagation characteristics of the MSWs in one-dimensional (1-D) [14, 15, 20, 22, 24, 27, 28], two-dimensional (2-D) [3, 17, 21, 25] and three-dimensional (3-D) [19] MCs. For example, the Kronig-Penny model was applied to Landau-Liftshitz equation to analyze the periodic structures of MCs that consist of ferromagnetic materials with varying saturation magnetizations [1, 2, 16]. Plane-wave expansion method was applied to Landau-Liftshitz equation to analyze 2-D and 3-D MCs that are composed of various types of ferromagnetic materials [18, 19], and the same method was also applied to Walker's equation to analyze the periodic structures of magnetic and non-magnetic layers [23]. In addition, Walker's equation [9–11] as well as the transmission-line model [26, 29, 32, 33] were also used to analyze 1-D/2-D MCs with periodic variation in thickness of the magnetic layer. Among these analytical approaches, only the new

approach based on Walker's equation developed by Prof. Tsai's group and presented in this dissertation is capable of analyzing magnetostatic volume waves (MSVWs) in 2-D MCs.

Microwave devices are essential in a wide variety of applications including military, civil, long-distance communication, and signal processing systems. A variety of MC-based microwave device applications have also been envisaged but only a few devices e.g. filter and waveguides were reported. MC-base devices possess the unique advantages of much smaller device dimension due to the much shorter wavelengths of the MSWs and tunability of the propagation characteristics of the MSWs via bias magnetic fields. In this dissertation, new wideband tunable MC-based devices such as microwave filters and phase shifters were also realized and demonstrated with superior performance characteristics.

1.2 Organization of Dissertation

In this dissertation, theoretical analysis and experimental verification of the propagation characteristics of MSWs in magnonic crystals (MCs), and wideband tunable microwave filters and phase shifters are presented.

The dissertation consists of 5 chapters. Following Chapter 1, the Introduction, Chapter 2 provides an overview on the fundamental theories of MSWs

and MCs. The equation of motion of magnetization and associated Polder permeability tensor are first derived. The derivation of Walker's equation and an introduction on MSWs are then presented.

In Chapter 3, the theoretical approach based on Walker's equation is derived. It is then employed to analyze 1-D and 2-D MCs. The experimental verifications with excellent agreements are also presented.

In Chapter 4, realization and performance characteristics of MC-based microwave devices including tunable filters and phase shifters, and waveguides are presented in detail.

Finally, a conclusion for the dissertation research is given in Chapter 5.

Chapter 2

Magnetostatic Waves and Magnonic Metamaterials

Magnetic excitations in solids at microwave frequencies have been a subject of continuing study, which began with the pioneering theory of spin waves reported by Holstein and Primakoff [34], the discovery of FMR by Griffiths [35], Kittel's linear response theory for FMR [36], and Walker's study on magnetostatic modes [37]. A special class of magnetic excitations include the uniform mode ferromagnetic resonance (FMR) and long wavelength propagating magnetostatic waves (MSWs) [38, 39]. The theoretical study on both FMR and MSWs starts with derivation of the equation of motion of magnetization for an electron under a dc bias magnetic field as presented in the following section [40].

2.1 Equation of Motion of Magnetization

For a single magnetic moment, its equation of motion is described by the Landau-Lifshitz equation with a damping term given by Eq.2.1. The precession described by this equation is shown in Fig.2.1.

$$\frac{\partial \vec{M}}{\partial t} = -\gamma \vec{M} \times \vec{H}_{eff} - \frac{\lambda}{M_s} \vec{M} \times \left(\vec{M} \times \vec{H}_{eff} \right) \tag{2.1}$$

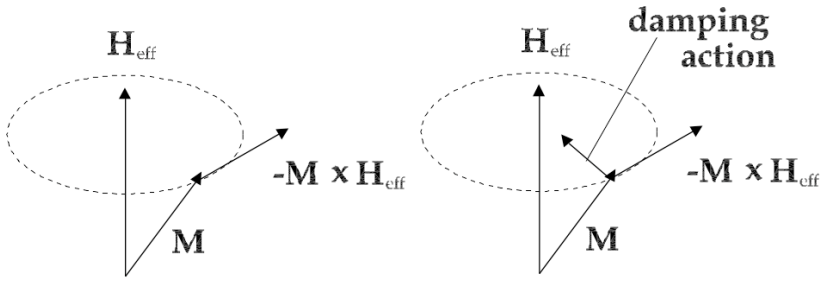

Figure 2.1: The precession of a magnetic moment described by the Landau-Lifshitz equation

In Eq.2.1, M_s is the saturation magnetization of the ferromagnetic material, H_{eff} is the effective magnetic field applied, λ is a phenomenological constant to describe the damping, and γ is the gyromagnetic ratio, which is the ratio of the magnetic moment to the angular momentum given below:

$$\gamma = \frac{g\,|e_0|}{2m_e c} \tag{2.2}$$

where g is Lande factor or the so-called g-factor, e_0 is the charge of an electron, m_e is the mass of the electron at rest, c is the speed of light. The

effective magnetic field is the functional derivative of the free energy. The effective magnetic field involved in this dissertation consists of anisotropic magnetic field of the material and the bias magnetic field. As Fig.2.1 shows, the magnetic moment would precess around the effective magnetic field.

The nature of the interaction that produces the magnetic ordering was first explained by Heisenberg[41], who showed that it is electrostatic in origin and is due to the quantum-mechanical exchange. For simplicity, a system of two neighboring magnetic ions, each with one electron, is considered. The two possible spin states are the symmetric $\chi_{s=1}$ and the antisymmetric $\chi_{s=0}$, where χ is the spin part of the wave functions of the electrons. When the wave functions of the two electrons appreciably overlapped as shown in Fig. 2.2, the corresponding interaction energy ($\mathcal{H}$) can be expressed as follows:

Figure 2.2: The hydrogen molecule consists of two protons, each with a bound electron. The protons are sufficiently close so that the electronic wave functions overlap.

$$\mathcal{H} = -\mathcal{J}_{12} s_1 \cdot s_2 \tag{2.3}$$

in which s_1 and s_2 are the spin operators for the two electrons. The quan-

tity $\mathcal{J}_{12}$, which depends on the overlap of the electronic wave functions, is called exchange interaction[42, 43]. Typically the exchange interaction is short range, and in many cases it is sufficient to consider only the nearest-neighbor sites. A complete mathematical description of exchange interaction is much more complicated than that described above but can be readily found in Ref. [43] chapter 2. A perturbation of the magnetic moment in the ferromagnetic material would propagate via coupling to the neighboring magnetic moment as shown in Fig.2.3. From the top view the perturbation looks like propagation of a sine wave. This wave is called spin waves (SWs).

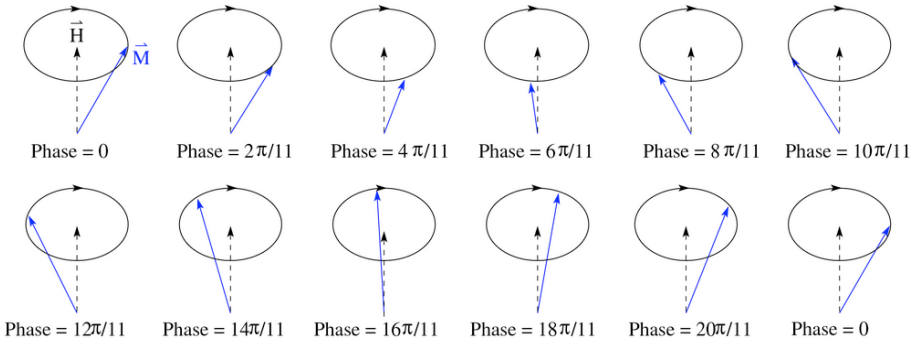

Figure 2.3: The precession of magnetic moment propagates in the ferromagnetic material to form the spin wave

There are different kinds of spin waves resulting from different wavelengths and the direction of propagation relative to the direction of the saturation magnetization. All these spin waves would be discussed in the following section.

2.2 Walker's Equation and Magnetostatic Waves (MSWs)

The theory of magnetostatic modes for spheroidal specimens was first reported by L. R. Walker and such modes are often called Walker Modes [37, 44]. Röschmann and Dötsch published a practical review on Walker modes for spheres [45]. The theory of magnetostatic modes excited in flat and unbounded ferromagnetic thin films was first reported by Damon and Eshbach which served as the foundations for numerous experimental studies of magnetic excitations in thin film and slabs of ferrite materials as well as device applications for microwave signal processing [46]. Subsequently, Storey *et al* extended this work to provide quantitative results for films of finite dimensions [47, 48].

SWs can be generally divided into three regions, namely exchange region, dipole-exchange region, and magnetostatic region, based on the wave numbers or wavelengths as shown in Table 2.1. The effect of exchange interaction reduces as the wavelengths increase. In this study, due to the long characteristic wavelengths involved the exchange interaction is neglected, and thus only the magnetostatic waves (MSWs) are considered. The two classes of MSWs are magnetostatic volume waves (MSVWs) and magnetostatic surface waves (MSSWs). Furthermore, there are two types of MSVWs, magnetostatic forward volume waves (MSFVWs) and magnetostatic backward volume waves (MSBVWs). The relative directions of bias magnetic field and propagation

vector involved in these three types of MSWs are shown in Fig.2.4.

Table 2.1: The different regions of SWs in terms of wave numbers k in ferromagnetic materials[42].

Region	Wave number range
Exchange region	$k > 10^6$ cm^{-1}
Dipole-exchange region	10^6 cm$^{-1} > k > 10^5$ cm^{-1}
Magnetostatic region	10^5 cm$^{-1} > k > 30$ cm^{-1}

2.2.1 Magnetization in Maxwell's Equations

Magnetization is defined as magnetic moment per unit volume. The four Maxwell's equations in CGS units are as follows:

$$\begin{aligned} \nabla \times \vec{E} + \frac{1}{c}\frac{\partial \vec{B}}{\partial t} = 0 \qquad & \nabla \cdot \vec{B} = 0 \\ \nabla \times \vec{H} - \frac{1}{c}\frac{\partial \vec{D}}{\partial t} = \frac{4\pi}{c}\vec{J} \qquad & \nabla \cdot \vec{D} = 4\pi\rho \end{aligned} \tag{2.4}$$

The field quantities are defined as follows:

$\vec{H}$ is the magnetic field intensity;

$\vec{E}$ is the electric field intensity;

$\vec{B}$ is the magnetic flux density;

$\vec{D}$ is the electric flux density;

$\vec{J}$ is the electric volume current density;

ρ is the electric volume charge density.

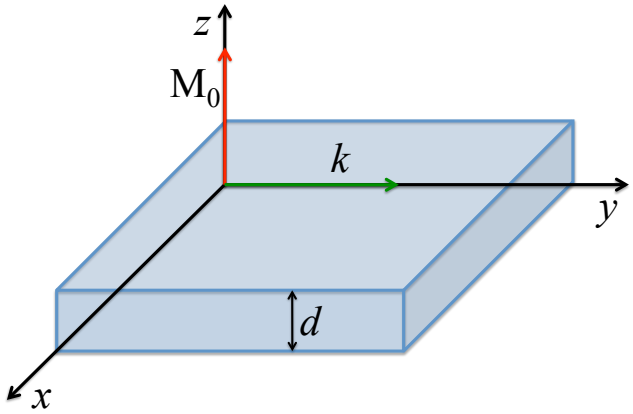

(a) In FVMSW, $\vec{k} \perp \vec{M}_0 \parallel \vec{n}_0$.

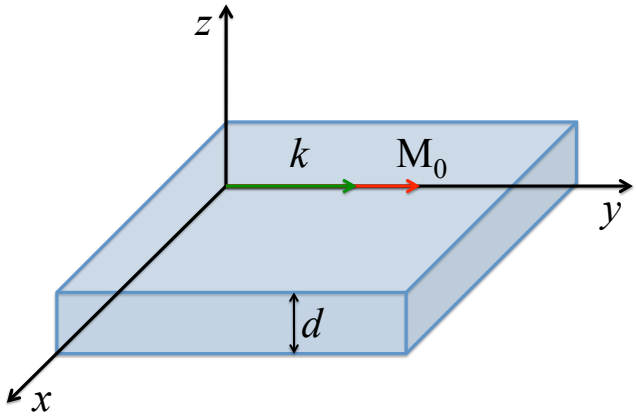

(b) In BVMSW, $\vec{k} \parallel \vec{M}_0 \perp \vec{n}_0$.

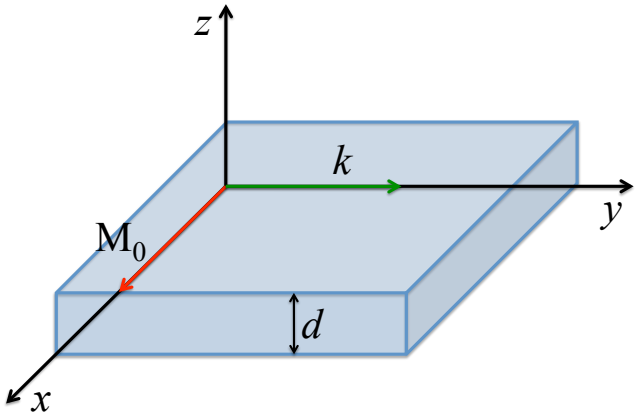

(c) In MSSW, $\vec{k} \perp \vec{M}_0 \perp \vec{n}_0$.

Figure 2.4: The relative directions of propagation constant k and steady magnetization M_0 of three types of magnetostatic waves, and n_0 is a unit vector normal to the plane.

where

$$\begin{aligned} \vec{D} &= \vec{E} + 4\pi\vec{P} \\ \vec{B} &= \vec{H} + 4\pi\vec{M} \end{aligned} \tag{2.5}$$

in which $\vec{P}$ is the dielectric polarization, and $\vec{M}$ is the magnetization. And the boundary conditions are

$$\begin{aligned} \vec{E}_1 \times \vec{n}_0 - \vec{E}_2 \times \vec{n}_0 &= 0 & \vec{H}_1 \times \vec{n}_0 - \vec{H}_2 \times \vec{n}_0 &= \frac{4\pi}{c}\vec{J}_s \\ \vec{D}_1 \cdot \vec{n}_0 - \vec{D}_2 \cdot \vec{n}_0 &= 4\pi\rho_s & \vec{B}_1 \cdot \vec{n}_0 - \vec{B}_2 \cdot \vec{n}_0 &= 0 \end{aligned} \tag{2.6}$$

where ρ_s and $\vec{J}_s$ are surface densities, respectively, of electric charge and current. The subscription 1 and 2 represent the $\vec{H}$, $\vec{E}$, $\vec{B}$, and $\vec{D}$ in two different media separated by the boundary. The magnetic field consists of steady and ac components. Here we assume that the ac components, $\vec{h}$, $\vec{e}$, $\vec{b}$, $\vec{d}$, ρ_a, and $\vec{j}$, are small compared to the steady components, $\vec{H}$, $\vec{E}$, $\vec{B}$, $\vec{D}$, ρ, and $\vec{J}$. The set of equations relating the ac components are as follows:

$$\begin{aligned} \nabla \times \vec{e} + ik_0\vec{b} = 0 \qquad & \nabla \cdot \vec{b} = 0 \\ \nabla \times \vec{h} - ik_0\vec{d} = \frac{4\pi}{c}\vec{j} \qquad & \nabla \cdot \vec{d} = 4\pi\rho_a \end{aligned} \tag{2.7}$$

Now consider the following material equations in which $\vec{d}$ depends only on $\vec{e}$, and $\vec{b}$ depends only on $\vec{h}$:

$$\vec{d} = \tilde{\epsilon}\vec{e}, \qquad \vec{b} = \tilde{\mu}\vec{h} \tag{2.8}$$

where $\tilde{\epsilon}$ and $\tilde{\mu}$ are the permittivity tensor and the Polder permeability tensor, respectively. In this study, the permittivity tensor is treated as a scalar for the ferromagnetic material yttrium iron garnet (YIG) involved, while the permeability tensor is to be determined as follows. In the Landau-Lifshitz equation without a damping term, Eq.2.9, $\vec{M}$ and $\vec{H}$ are terms containing the steady components, $\vec{M}_0$ and $\vec{H}_0$, and the ac components, $\vec{m}$ and $\vec{h}$, as Eq.2.10 shows.

$$\frac{\partial \vec{M}}{\partial t} = -\gamma \vec{M} \times \vec{H} \tag{2.9}$$

$$\begin{aligned} \vec{M} &= \vec{M}_0 + \vec{m} \qquad \vec{m} \ll \vec{M}_0 \\ \vec{H} &= \vec{H}_0 + \vec{h} \qquad \vec{h} \ll \vec{H}_0 \end{aligned} \tag{2.10}$$

When magnetization is saturated, $\vec{M}_0$ is parallel to $\vec{H}_0$, and Eq.2.9 can be written as follows:

$$\begin{aligned} \frac{\partial \vec{m}}{\partial t} &= -\gamma \left(\vec{M}_0 + \vec{m} \right) \times \left(\vec{H}_0 + \vec{h} \right) \\ &= -\gamma \left(\vec{M}_0 \times \vec{H}_0 + \vec{M}_0 \times \vec{h} + \vec{m} \times \vec{H}_0 + \vec{m} \times \vec{h} \right) \end{aligned} \tag{2.11}$$

Since $\vec{M}_0$ and $\vec{H}_0$ are in the same direction, $\vec{M}_0 \times \vec{H}_0$ is equal to zero. And the term $\vec{m} \times \vec{h}$ is negligible because $\vec{m} \ll \vec{M}_0$ and $\vec{h} \ll \vec{H}_0$. Eq.2.11 can be further simplified as follows:

$$\frac{\partial \vec{m}}{\partial t} + \gamma \vec{m} \times \vec{H}_0 = -\gamma \vec{M}_0 \times \vec{h} \tag{2.12}$$

This equation can also be decomposed into the following three equations:

$$
\begin{aligned}
i\omega m_x + \gamma H_0 m_y &= \gamma M_0 h_y \\
-\gamma H_0 m_x + i\omega m_y &= \gamma M_0 h_x \\
i\omega m_z &= 0
\end{aligned}
\tag{2.13}
$$

The solution for Eq.2.13 is as follows:

$$
m_x = \chi h_x + i\chi_a h_y \qquad m_y = -i\chi_a h_x + \chi h_y \qquad m_z = 0 \tag{2.14}
$$

where

$$
\chi \equiv \frac{\gamma M_0 \omega_H}{\omega_H^2 - \omega^2} \qquad \chi_a \equiv \frac{\gamma M_0 \omega}{\omega_H^2 - \omega^2} \tag{2.15}
$$

The notation ω_H will be used through out in this dissertation, which is

$$
\omega_H = \gamma H_0 \tag{2.16}
$$

Finally, Eq.2.14 can be written in a tensor form

$$
\vec{m} = \tilde{\chi}\vec{h} \tag{2.17}
$$

where the ac (high-frequency) magnetic susceptibility $\tilde{\chi}$ is a non-symmetric second-rank tensor:

$$\tilde{\chi} = \begin{bmatrix} \chi & i\chi_a & 0 \\ -i\chi_a & \chi & 0 \\ 0 & 0 & 0 \end{bmatrix} \tag{2.18}$$

From the relationships $\vec{b} = \vec{h} + 4\pi\vec{m}$ and $\vec{b} = \tilde{\mu}\vec{h}$,

$$\tilde{\mu} = \tilde{I} + 4\pi\tilde{\chi} \tag{2.19}$$

In which $\tilde{I}$ is a unit tensor. By combining Eq.2.18 and Eq.2.19, the following Polder permeability tensor $\tilde{\mu}$ is obtained:

$$\tilde{\mu} = \begin{bmatrix} \mu & i\mu_a & 0 \\ -i\mu_a & \mu & 0 \\ 0 & 0 & 1 \end{bmatrix} \tag{2.20}$$

where

$$\mu = 1 + 4\pi\chi = \frac{\omega_H\left(\omega_H + \omega_M\right) - \omega^2}{\omega_H^2 - \omega^2} \qquad \mu_a = 4\pi\chi_a = \frac{\omega\omega_M}{\omega_H^2 - \omega^2} \tag{2.21}$$

where

$$\omega_M \equiv \gamma 4\pi M_0 \tag{2.22}$$

There is a peculiar point that the diagonal component μ is negative when the applied magnetic field from H_2 to $\frac{\omega}{\gamma}$. The antiresonance field H_2, at which $\mu = 0$, is

$$H_2 = \sqrt{\left(\frac{\omega}{\gamma}\right)^2 + (2\pi M_0)^2} - 2\pi M_0 \tag{2.23}$$

The condition of antiresonance can be written also as $\omega = \omega_\perp$ where

$$\omega_\perp = \sqrt{\omega_H \left(\omega_H + \omega_M\right)} \tag{2.24}$$

2.2.2 Walker's Equation

The non-exchange magnetostatic waves (MSWs) in a bounded ferromagnetic material is discussed in this section. For the non-exchange MSWs, the propagation constant k is much larger than the propagation constant $k_0 = \omega/c$ in free space, so we can use magnetostatic approximation to analyze these waves and neglect the $ik_0\vec{d}$ term in Eq.2.7. In the problem we deal with, $j_{ext} = 0$,

so

$$\nabla \times \vec{h} = 0 \qquad \nabla \cdot \left(\tilde{\mu}\vec{h}\right) = 0 \tag{2.25}$$

Again, as mentioned previously, the exchange interaction can be neglected for the non-exchange magnetostatic waves because of the large wavelength involved. There are two types of MSWs: volume type waves and surface type waves. The volume waves may take the form of forward waves or backward waves. The magnetostatic potential ψ inside a ferromagnetic plate in the direction normal to the plate surface is of trigonometric functions. For the surface waves, ψ inside the ferromagnetic plate in the direction normal to the plate surface is of hyperbolic function. The relative directions of the quantities involved are shown in Fig.2.4. Treatment for the magnetostatic waves begins with introduction of the magnetostatic potential ψ so that

$$\vec{h} = \nabla\psi \tag{2.26}$$

Substituting Eq.2.26 into Eq.2.25, we obtain the equation

$$\nabla \cdot (\tilde{\mu}\nabla\psi) = 0 \tag{2.27}$$

Assuming that the z-axis is normal to the boundary surface the boundary conditions for ψ are as follows:

$$\frac{\partial \psi_1}{\partial x} = \frac{\partial \psi_2}{\partial x} \qquad \frac{\partial \psi_1}{\partial y} = \frac{\partial \psi_2}{\partial y} \qquad \left(\tilde{\mu}_1 \nabla \psi_1\right)_z = \left(\tilde{\mu}_2 \nabla \psi_2\right)_z \tag{2.28}$$

where the subscripts 1 and 2 designate the two media separating the boundary. From Eq.2.27 and the $\tilde{\mu}$ given by Eq.2.20, we have the following equation for the magnetostatic potential in the bounded ferromagnetic medium:

$$\mu \left(\frac{\partial^2 \psi}{\partial x^2} + \frac{\partial^2 \psi}{\partial y^2} \right) + \frac{\partial^2 \psi}{\partial z^2} = 0 \tag{2.29}$$

2.3 Magnetostatic Waves

2.3.1 Magnetostatic Forward Volume Waves (MSFVWs)

For the forward volume wave case, the solution of Eq.2.29 takes the following form:

$$\psi = \left(A \cos(k_z z) + B \sin(k_z z)\right) \exp(-iky) \tag{2.30}$$

For simplicity, we assume that perfect conductors are placed on the bound-

aries $z = 0$ and $z = d$, namely,

$$(\tilde{\mu}\nabla\psi) \cdot \vec{n}_0 = 0 \qquad \frac{\partial\psi}{\partial n} = 0 \tag{2.31}$$

$$\frac{\partial\psi}{\partial n} = \frac{\partial\psi}{\partial z} = (-Ak_z \cos(k_z z) + Bk_z \sin(k_z z)) \exp(-iky) = 0 \tag{2.32}$$

By matching the boundary conditions on $z = 0$ and $z = d$, we obtain $B = 0$ and

$$k_z d = n\pi \Rightarrow k_z = \frac{n\pi}{d} \tag{2.33}$$

where n is an integer that designates the modes for the forward volume waves. By substituting Eq.2.30 into Eq.2.29 the following relation is obtained:

$$k_z^2 = -\mu k^2 \tag{2.34}$$

It is seen from Eq.2.34 that the propagating waves exist only for $\mu < 0$, and $\mu < 0$ falls in the frequency range of $\omega_H \leq \omega \leq \omega_\perp$ in which $\omega_\perp = \sqrt{\omega_H (\omega_H + \omega_M)}$ is given by Eq. 2.24. Finally, substituting μ given in Eq.2.21 into Eq.2.34, the following dispersion relation is obtained:

$$\left(\frac{Z_n}{d}\right)^2 = -\frac{\omega_H\left(\omega_H+\omega_M\right)-\omega^2}{\omega_H^2-\omega^2}k^2$$
$$\Rightarrow \omega^2 = \omega_H\left[\omega_H + \frac{\omega_M}{1+\left(Z_n/kd\right)^2}\right] \tag{2.35}$$

where $Z_n = n\pi$. The plots for the dispersion relation for a number of modes are shown in Fig.2.5.

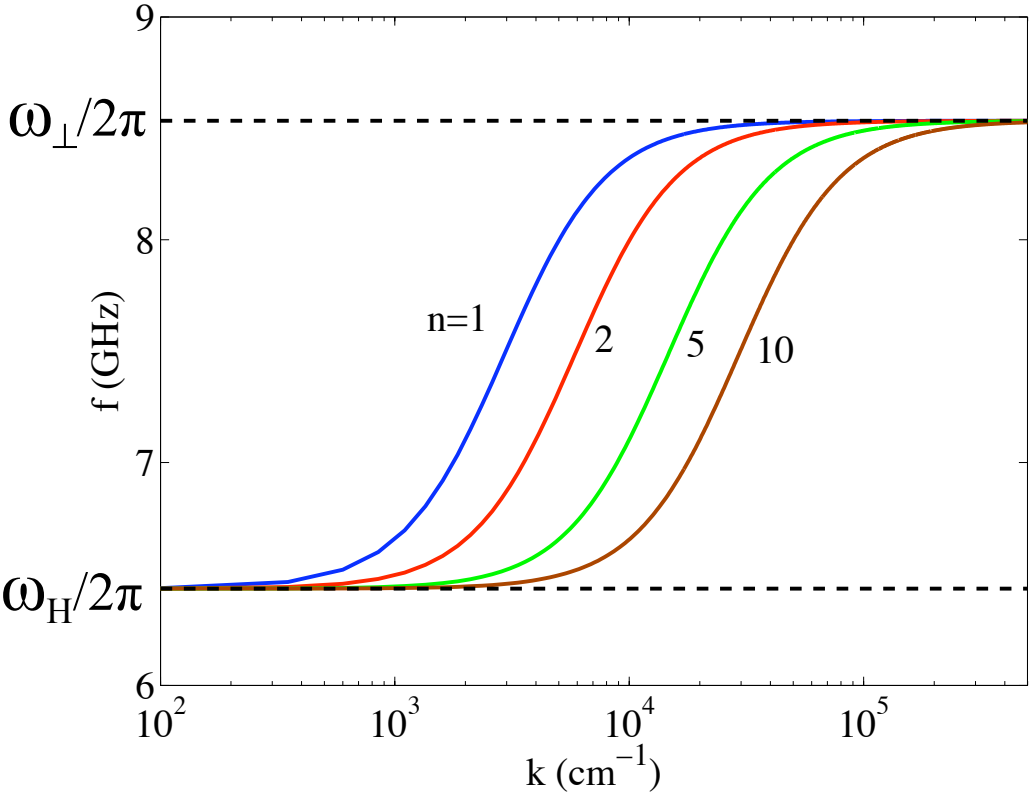

Figure 2.5: The dispersion relations of the forward volume waves, with $M_0 = 139$G, $H_0 = 2300$Oe, and $d = 10\mu$m. The lower frequency limit is $\omega_H/2\pi$, and the higher frequency limit is $\omega_\perp/2\pi$.

For the YIG film with $d = 10\mu$m and $n = 1$, $(v_{gr})_{max} \approx 2.5\times10^6$ cm/s, which is 4-order lower than the velocity of electromagnetic waves in a dielectric.

2.3.2 Magnetostatic Backward Volume Waves (MSBVWs)

In the case of magnetostatic backward volume waves, in contrast to the special case shown in Fig.2.4(b), the general case shown in Fig.2.6, in which the k and M_0 have an angle θ_k between them is analyzed first. Note that for this purpose the coordinate system is also altered to make M_0 lies on the z-axis.

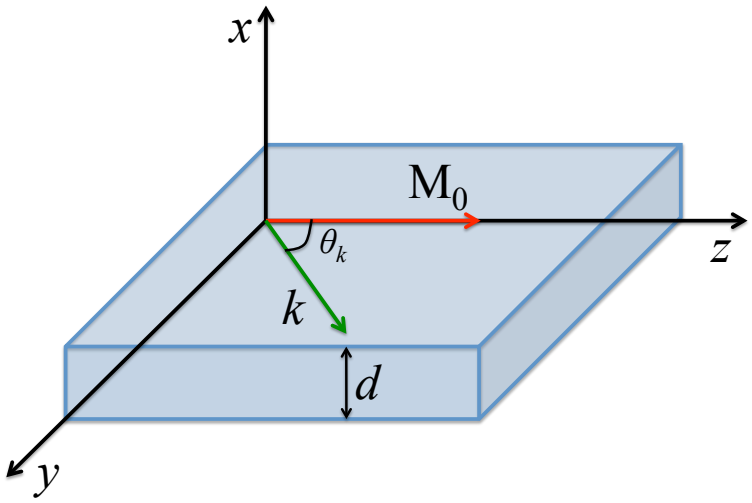

Figure 2.6: The relative direction of k and M_0.

The corresponding magnetostatic potential ψ is

$$\psi = (A\cos(k_x x) + B\sin(k_x x))\exp(-ik_y y - ik_z z) \tag{2.36}$$

By substituting Eq.2.36 into Eq.2.29 we obtain

$$\mu\left(k_x^2 + k_y^2\right) = k_z^2 \tag{2.37}$$

Similarly, assuming perfect conductors on the boundaries $x = 0$ and $x = d$ and applying the boundary condition $(\tilde{\mu}\nabla\psi)\cdot\vec{n}_0 = 0$ with $\tilde{\mu}$ given by Eq.2.20, the following equation is obtained:

$$\mu\frac{\partial\psi}{\partial x} + i\mu_a\frac{\partial\psi}{\partial y} = 0 \tag{2.38}$$

Matching of the boundary conditions on the planes $x = 0$ and $x = d$ lead to Eq.2.39 and Eq.2.40, respectively:

$$Ak_y\mu_a + Bk_x\mu = 0 \tag{2.39}$$

$$A\left[\mu_a k_y\cos(k_x d) - \mu k_x\sin(k_x d)\right] + B\left[\mu k_x\cos(k_x d) + \mu_a k_y\sin(k_x d)\right] = 0 \tag{2.40}$$

For a solution to exist the determinant constructed from the coefficients of A and B in Eq.2.39 and Eq.2.40 must vanish, i.e.

$$\det\left(\begin{bmatrix} k_y\mu_a & k_x\mu \\ \mu_a k_y\cos(k_x d) - \mu k_x\sin(k_x d) & \mu k_x\cos(k_x d) + \mu_a k_y\sin(k_x d) \end{bmatrix}\right) = 0 \tag{2.41}$$

After expansion of Eq.2.41, the following equation is obtained:

$$\left(\mu_a^2 k_y^2 + \mu^2 k_x^2\right) \sin(k_x d) = 0 \tag{2.42}$$

For the volume waves, k_x is assumed to be real. Thus, the solution for Eq.2.42 is $k_x d = n\pi \equiv X_n$. By putting this solution back to Eq.2.37, the following dispersion relation is obtained:

$$\begin{aligned} & -\frac{\omega_H\left(\omega_H+\omega_M\right)-\omega^2}{\omega_H^2-\omega^2}\left[\left(X_n/d\right)^2+k_y^2\right]=k_z^2 \\ & \Rightarrow \omega^2=\omega_H\left\{\omega_H+\frac{\omega_M}{1+\frac{k_z^2 d^2}{X_n^2+k_y^2 d^2}}\right\} \\ & \equiv \omega_H\left\{\omega_H+\frac{\omega_M}{1+\frac{\cos^2\theta_k}{X_n^2/k^2 d^2+\sin^2\theta_k}}\right\} \end{aligned} \tag{2.43}$$

For the special case with $\theta_k = 0$, the ω-k plots for the dispersion relations are shown in Fig.2.7.

Fig.2.7 shows that the group velocity $v_{gr} \equiv \partial\omega/\partial k$ is negative and antiparallel to the phase velocity v_{ph}. This is the reason why such waves are called *backward waves*. For the case with $\theta_k \neq 0$ or $\neq \pi/2$, the slopes of the plots for the dispersion relation are still negative, but not antiparallel to the phase velocity. Note that the direction of v_{ph} is usually determined by the

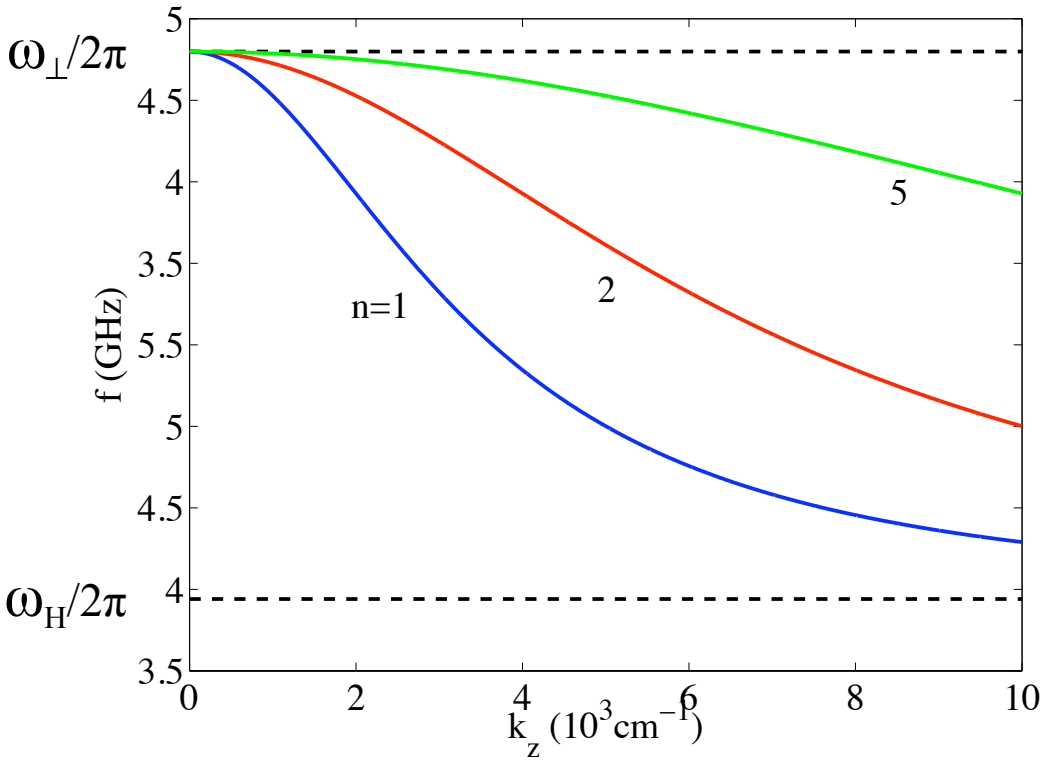

Figure 2.7: The dispersion relation of magnetostatic backward volume waves, where $M_0 =$ 90G, $H_0 =$ 1350Oe,and $d = 10\mu$m. The lower frequency limit is $\omega_H/2\pi$, and the higher frequency limit is $\omega_\perp/2\pi$.

orientation of the microstrip conductor.

2.3.3 Magnetostatic Surface Waves (MSSWs)

For treatment of magnetostatic surface waves, we consider the geometry in which the ferromagnetic plate is situated between dielectrics, rather than perfect conductors, as shown in Fig.2.4(c). The corresponding magnetostatic potential in the ferromagnetic plate is as follows:

$$\psi = [A\exp(-\kappa z) + B\exp(\kappa z - \kappa d)]\exp(-iky) \tag{2.44}$$

where A and B are constants to be determined. The magnetostatic potential outside the ferromagnetic plate is

$$\psi_0 = \begin{cases} C\exp(\kappa_0 z + iky) & z < 0 \\ D\exp(-\kappa_0 z + \kappa_0 d - iky) & z > d \end{cases} \tag{2.45}$$

where C and D are constants to be determined.

Now the boundary conditions are matched in the same manner as in the magnetostatic forward volume waves. The resulting dispersion relation is given by Eq.2.46 and the corresponding ω-k plots are shown in Fig.2.8.

$$\omega^2 = \left(\omega_H + \frac{\omega_M}{2}\right)^2 - \left(\frac{\omega_M}{2}\right)^2 \exp(-2kd) \tag{2.46}$$

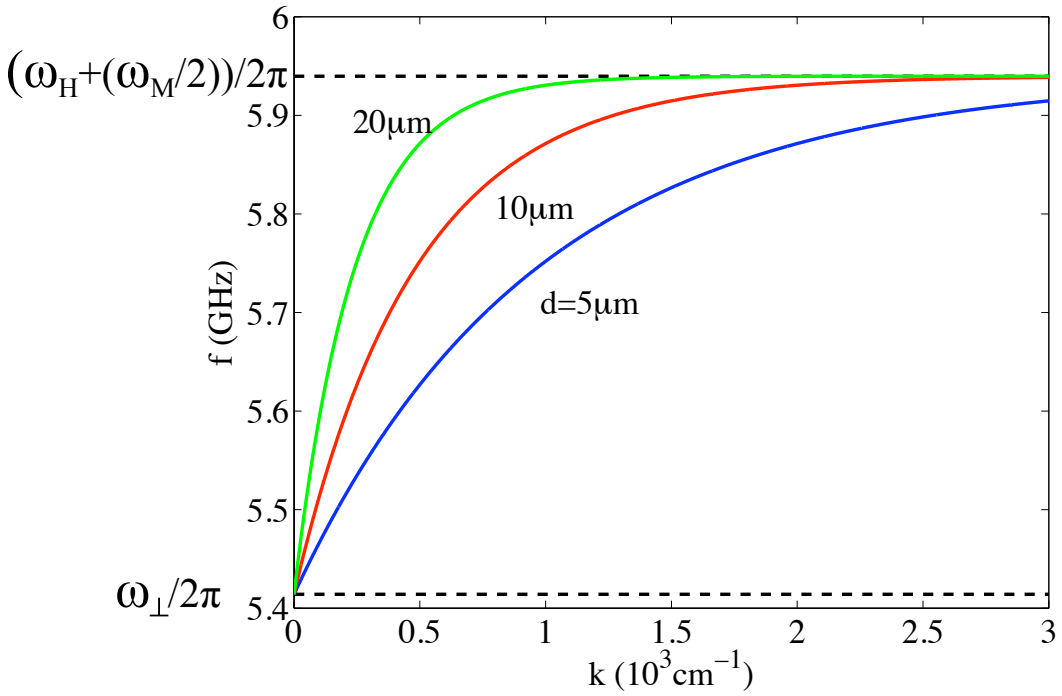

Figure 2.8: The dispersion relation of surface waves, where $M_0 = 139$G, $H_0 = 1250$Oe,and d is shown in the figure. The lower frequency limit is $\omega_\perp/2\pi$, and the higher frequency limit is $\left(\omega_H + \frac{1}{2}\omega_M\right)/2\pi$.

Finally, the group velocity $v_{gr} \equiv \partial\omega/\partial k$ is obtained from the dispersion relation as follows:

$$v_{gr} = \frac{d\omega_M^2}{4\omega} \exp(-2kd) \tag{2.47}$$

The frequency range for the MSSW to propagate is $\omega_\perp \leq \omega \leq \omega_H + \frac{1}{2}\omega_M$, which is adjoint with the frequency range for the propagation of the volume waves, $\omega_H \leq \omega \leq \omega_\perp$.

The following advantages of magnetostatic waves in ferromagnetic films should be emphasized:

1. Large range of operation frequency (about $1 - 50$ GHz).
2. Possibility of tuning by variation of the DC-bias magnetic field.
3. The large range of propagation constants ($30 - 10^5$ cm^{-1}) at a given frequency can be facilitated by tuning the DC bias magnetic field and, thus, convenient for various applications.
4. Low group velocity controllable by the DC bias magnetic field.
5. Possibility to change the dispersion relation in simple manners, e.g., by the choice of the wave type and the thickness of ferromagnetic layers.
6. Relatively low propagation losses, and
7. Efficient excitation by microstrip transducers of simple design.

2.4 Magnonic Crystals

Magnonic Crystals (MCs) are magnetic metamaterials resulting from periodic variations in geometrical structure and/or material properties. It possesses interesting features such as controllable generation and propagation of the magnetostatic waves (MSWs)/spin waves (SWs) and tunable bandgaps. The

SWs propagating in MCs are analogous to electromagnetic waves propagating in photonic crystals (PCs). PC-based devices are made in the size of the wavelengths, so devices for visible or infrared regions are small and in nanometer range, but devices for RF frequencies are relatively large, i.e. centimeter to meter range. On the other hand, the wavelengths for spin waves are much shorter than electromagnetic waves at the same frequency, so miniature (micrometer range) MC-based RF devices are achievable. In addition, the characteristics of MCs can be easily controlled by external bias magnetic field because ferromagnetic materials are highly sensitive to the bias field. Planar, miniature, and tunable devices with the aforementioned advantages can be realized by utilizing the MSWs in the magnonic crystals. The concept and the superior performance of MC-based devices have been successfully demonstrated by Prof. Chen S. Tsai's group and presented in Chapter 4. It is very challenging to model and simulate MC-based structures and devices. Because the wavelengths of MSWs are very short in comparison to that of the ordinary electromagnetic waves, it takes the commercial softwares like HFSS a long time, i.e. days, to accurately analyze the characteristics of MCs. A numbers of theoretical approaches and numerical methods have been proposed to model the characteristics of MCs. We proposed, for the first time, a new theoretical approach using Walker's equation presented in section 2.2.2 to analyze MCs with periodic variation in thickness of the ferromagnetic substrate such as YIG. This approach is capable of efficiently analyzing the

MCs and significantly reducing the simulation time to minutes. The detailed derivations and experimental verifications are presented in the Chapter 3.

Chapter 3

Theoretical Analysis and Experimental Verification of MSVWs in Magnonic Metamaterials

In Chapter 2, equation of motion of magnetization and the associated Polder permeability tensor were introduced. Walker's equation was employed to analyze the propagation characteristics of magnetostatic volume waves (MSVWs) in one-dimensional (1-D) and two-dimensional (2-D) magnonic crystals (MCs) with the eigenvalue equations derived in matrix form by Professor Chen S. Tsai's group[9–11] . By solving the eigenvalue equations, the band structures associated with MSVWS in 1-D and 2-D MCs at normal and oblique incidence have been found and verified experimentally, and are presented in this chapter.

3.1 Walker Equation-Based Theoretical Approach

Various analytical approaches have been employed for studying the propagation characteristics of the magnetostatic waves (MSWs) in 1-D, 2-D, and three-dimensional (3-D) MCs. Among these studies, Ref. [3] was the only report on 2-D MCs with periodic variation of layer thickness heretofore. In that work, the theoretical results were obtained with one component of the wave number fixed and the other component of the wave number varied, and the experiments were focused on studying the relationship between the etching depth of the YIG film and the decay of magnetostatic surface waves (MSSWs). The theoretical approach based on Walker's equation proposed by Prof. Tsai's group was the first one to calculate the propagation characteristics of MSVWs in 1-D and 2-D MCs with periodic variation in ferromagnetic film thickness. The theoretical analysis begins with Walker's equation and Polder permeability tensor given by Eq.2.27 and Eq.2.20, respectively. The frequency-dependent parameters μ and μ_a in Eq.2.20 are defined in Eq.2.21.

In the case of MSFVWs propagation in the X-Y plane in a ferromagnetic layer with thickness d in the Z-direction, the Walker's equation is expanded as follows:

$$\nabla \cdot (\tilde{\mu} \nabla \psi) = \frac{\partial}{\partial x}\left(\mu \frac{\partial \psi}{\partial x}\right) + \frac{\partial}{\partial y}\left(\mu \frac{\partial \psi}{\partial y}\right) + \frac{\partial^2 \psi}{\partial z^2} \tag{3.1}$$

By assuming the top and bottom boundaries of the magnetic layer as perfect

conductor, ψ is readily found to take the following form:

$$\psi = A\sin(k_z z)\exp\left[-i\left(k_x x + k_y y\right)\right] \tag{3.2}$$

where A is a constant, k_x and k_y are the wave number of the MSFVWs in X- and Y-direction, respectively, and k_z is the wave number in the Z-direction which is equal to $n\pi/d$, in which n is an integer and d is the thickness of the magnetic layer. Substituting μ and ψ into Eq.3.1 an eigenvalue equation for the MSFVW is obtained as Eq.3.3. Similarly, the eigenvalue equation for the MSBVW is obtained as Eq.3.4.

$$\left(D_{x2} + D_{y2} - k_z^2\right)^{-1}\left[\left(4\pi M_s H_0 + H_0^2\right)\left(D_{x2} + D_{y2}\right) - H_0^2 k_z^2\right]\psi = \frac{\omega^2}{\gamma^2}\psi \tag{3.3}$$

$$\left(D_{x2} + D_{y2} - k_z^2\right)^{-1}\left[H_0\left(H_0 + 4\pi M_s\right)\left(-k_z^2\right) + H_0^2\left(D_{x2} + D_{y2}\right)\right]\psi = \frac{\omega^2}{\gamma^2}\psi \tag{3.4}$$

where

$$D_{x2} = -k_x^2 - 2ik_x\frac{\partial}{\partial x} + \frac{\partial^2}{\partial x^2}; \quad D_{y2} = -k_y^2 - 2ik_y\frac{\partial}{\partial y} + \frac{\partial^2}{\partial y^2} \tag{3.5}$$

and M_s and H_0 are saturation magnetization and bias magnetic field, respec-

tively. Now, using a finite-difference method the eigenvalue equations are presented in the following matrix form:

$$\mathcal{M}\Psi = \left(\frac{\omega}{\gamma}\right)^2 \Psi \tag{3.6}$$

where Ψ is the magnetic vector potential, and $\mathcal{M}$ is a matrix that includes the parameters of wave numbers, ferromagnetic material properties, and ferromagnetic film geometry, namely, k_x, k_y, M_s, H_0, and k_z. Therefore, the frequency ω of the MSVWs can be found by solving the eigenvalue of Eq. (3.6). The correctness of this approach has been verified by experiments presented in the following sections.

Subsequently, the theoretical approach was further improved to calculate complex wave numbers as eigenvalues with given frequencies. Imaginary parts of the calculated complex wave numbers are absorption levels for MSWs propagating in MCs. When bias magnetic field is applied in Z-direction, Walker's equation is expanded as shown in Eq 3.1. In the case of MSFVWs propagating in the X-Y plane in a ferromagnetic layer with thickness d in the Z-direction, Eq. (3.1) is expanded and organized in the following polynomial equation:

$$(-\mu)\, k_y^2 \psi + \left(-2i\mu \frac{\partial}{\partial y}\right) k_y \psi + \left(\mu \frac{\partial^2}{\partial x^2} + \mu \frac{\partial^2}{\partial y^2} - k_z^2\right) \psi = 0 \tag{3.7}$$

In the case of MSBVWs propagating in Z-direction, which is parallel to the bias magnetic file, in a ferromagnetic layer with thickness d in the X-direction, the following polynomial equation is obtained:

$$-k_z^2\psi + \left(-2i\frac{\partial}{\partial z}\right)k_z\psi + \left(-\mu k_x^2 + \mu\frac{\partial^2}{\partial y^2} + \frac{\partial^2}{\partial z^2}\right)\psi = 0 \qquad (3.8)$$

in which k_x, k_y, and k_z are the wave numbers in the X-, Y-, and Z-direction, respectively, and k_z and k_x are $2n\pi/d$ in the case of MSFVWs and MSBVWs, respectively, as mentioned previously.

Both Eq. 3.7 and 3.8 are then generalized in the following form of non-linear eigenvalue equation:

$$A_2\lambda^2\psi + A_1\lambda\psi + A_0\psi = 0 \qquad (3.9)$$

By assuming $\xi = \lambda\psi$, Eq. 3.9 is presented a matrix as follow:

$$\begin{bmatrix} -A_0 & 0 \\ 0 & I \end{bmatrix}\begin{bmatrix} \psi \\ \xi \end{bmatrix} = \lambda\begin{bmatrix} A_1 & A_2 \\ I & 0 \end{bmatrix}\begin{bmatrix} \psi \\ \xi \end{bmatrix} \qquad (3.10)$$

For MSFVWs,

$$A_2 = -\mu \tag{3.11}$$

$$A_1 = -2i\mu\frac{\partial}{\partial y} \tag{3.12}$$

$$A_0 = \mu\frac{\partial^2}{\partial x^2} + \mu\frac{\partial^2}{\partial y^2} - k_z^2 \tag{3.13}$$

$$\lambda = k_y \tag{3.14}$$

For MSBVWs,

$$A_2 = -I \tag{3.15}$$

$$A_1 = -2i\frac{\partial}{\partial z} \tag{3.16}$$

$$A_0 = -\mu k_x^2 + \mu\frac{\partial^2}{\partial y^2} + \frac{\partial^2}{\partial z^2} \tag{3.17}$$

$$\lambda = k_z \tag{3.18}$$

in which ψ is magnetic potential, μ is previously defined in Eq. 2.21 consisting of frequency ω, saturation magnetization M_s, and bias magnetic field H_0. Finite difference method is now utilized to solve the eigenvalue problem and the complex wave numbers can be obtained with given frequencies and material properties. The significance of this improved method is that the absorption levels of the MSVWs in the frequency ranges of bandgaps can be

calculated efficiently. There is no available theoretical method that is able to calculate the absorption in 2-D MCs to the best of our knowledge. The validity of this method is verified by comparing with the experimental results presented in the following sections.

3.2 Sample Preparation and Experiment Setup

Magnonic crystals used the experimental verifications were fabricated on yttrium iron garnet (YIG) thin films with gadolinium gallium garnet (GGG) substrate[49–52]. The experimental setup was also carefully designed and constructed in order to eliminate interference and correctly identify the magnonic bandgaps.

3.2.1 Sample Preparation

The samples were prepared by photolithography and wet-etching techniques using orthophosphoric acid on a 100μm YIG/GGG thin film. The important fabrication steps are listed as follows:

1. Properly clean the YIG sample and avoid direct contact to the mask in order to ensure its surface quality.

2. Deposit 400nm SiO_2 on the surface of the YIG thin film as the mask.

Note that SiO_2 has good resistance over high temperature etching and is able to maintain its integrity.

3. Apply standard photolithographic technique upon the YIG sample.

4. Preheat orthophosphoric acid for 3 hours to 146°C with temperature variation controlled within 1°C.

5. Gently soak the sample into the acid and maintain the temperature at 146°C during etching.

6. Etching time was set at 120 minutes. The etched depth was close to 21.6 μm. The calculated etching rate was 0.1725-0.15 μm/min.

7. Complete the etching and clean the sample for measurements.

Note that the etching rate was greatly affected by the temperature, namely, around 20% increase with a 1°C temperature increment.

3.2.2 MSVWs in a Non-structured YIG Thin Film

The frequency response of the MSVWs excited in a non-structured ferromagnetic YIG thin film was measured and compared with the simulated results. A square YIG/GGG thin film with dimension of 8mm× 8mm × 100μm was used for the purpose. The bias magnetic fields were generated by a pair of Nd-Fe-B permanent magnets (0.75" in diameter and 0.5" in thickness) attached

to an iron yoke to complete the magnetic circuit as reported in Ref.[53–56]. Both types of MSVWs, namely forward volume waves and backward volume waves, were excited by setting the directions of the magnetic fields as shown in Fig. 2.4.

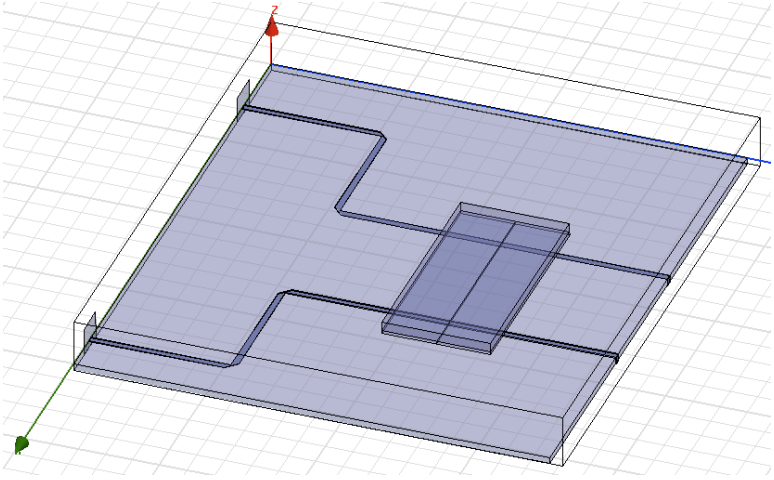

(a)

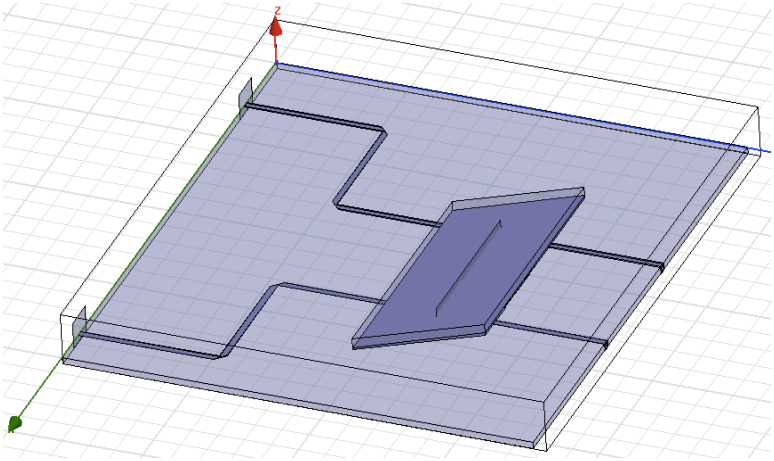

(b)

Figure 3.1: MSVWs excited in a non-structured YIG/GGG thin film sample of a (a) rectangular, and (b) parallelogram shape.

The measured and simulated frequency responses of the MSWs are compared in Fig. 3.2 with a close agreement clearly seen. The simulation was carried out using *Ansoft HFSS* software and the model shown in Fig. 3.1(a). Note

that both simulated and measured results show many fluctuating absorption peaks, which were caused by the destructive/constructive interferences of the reflected MSWs from the edges of the YIG thin film samples. A YIG thin film sample of parallelogram shape as shown in Fig. 3.1(b) was prepared to replace the original sample of rectangular shape [57]. As shown in Fig. 3.3(a) and Fig. 3.3(b), both simulation and experimental results showed that the YIG sample of parallelogram shape was capable of eliminating the undesirable fluctuations. Thus, YIG samples of parallelogram shape were utilized in subsequent 1-D and 2-D MCs experiments.

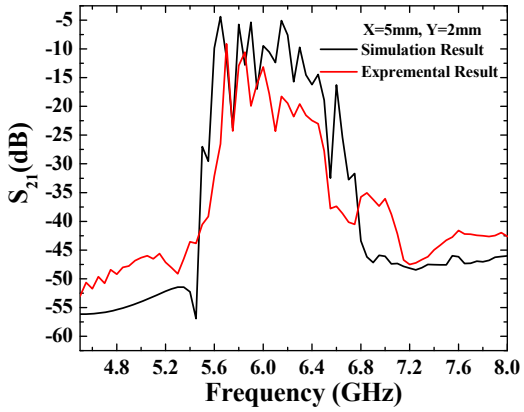

(a) HFSS simulation and experimental result of MSFVW.

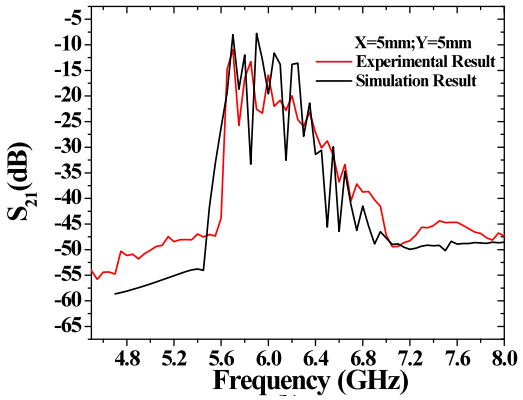

(b) HFSS simulation and experimental result of MSFVW.

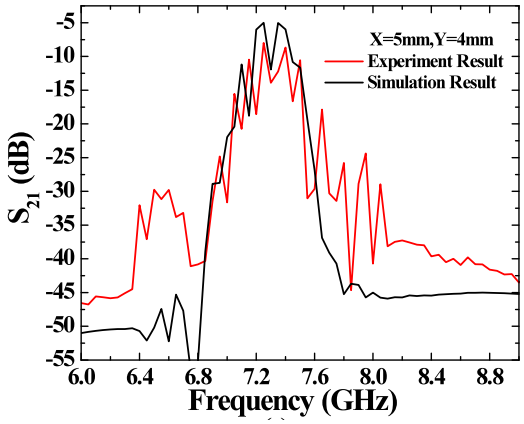

(c) HFSS simulation and experimental result of MSBVW.

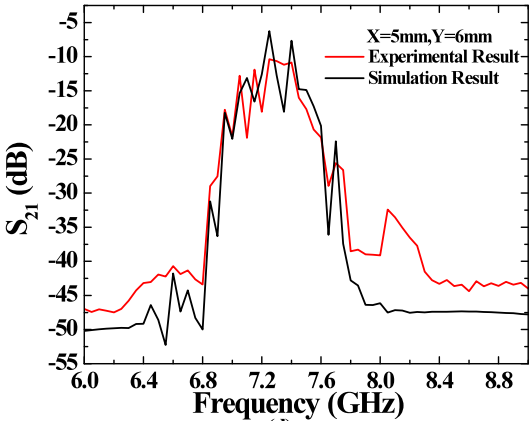

(d) HFSS simulation and experimental result of MSBVW.

Figure 3.2: Comparison of frequency response of MSVWs propagating in YIG thin film samples between HFSS simulation and experiment results. They have very good agreements.

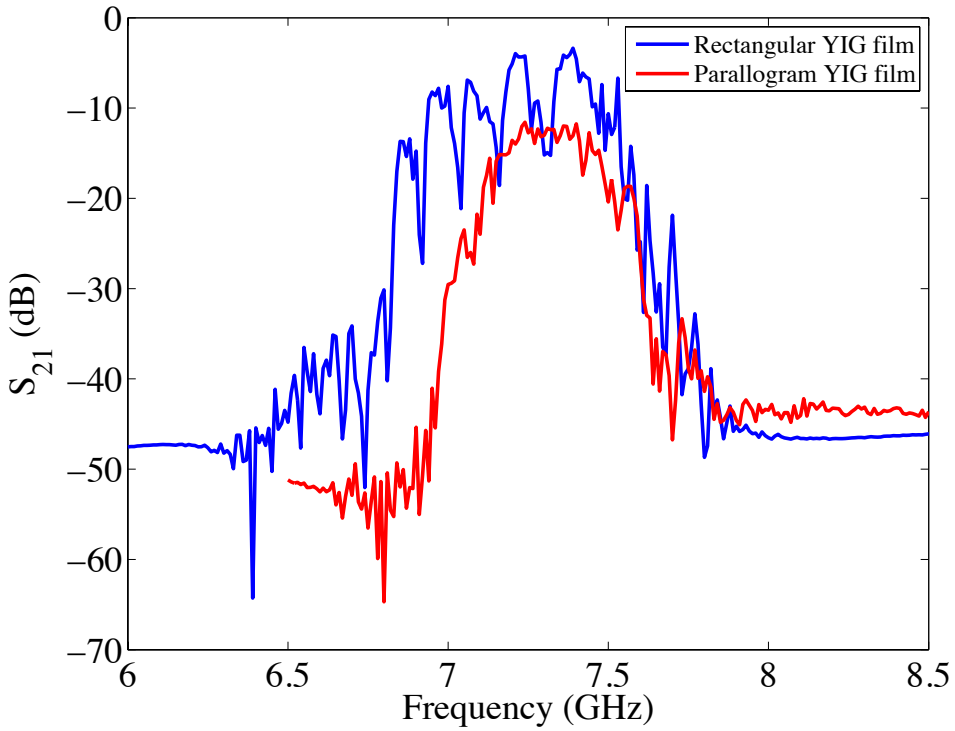

(a)

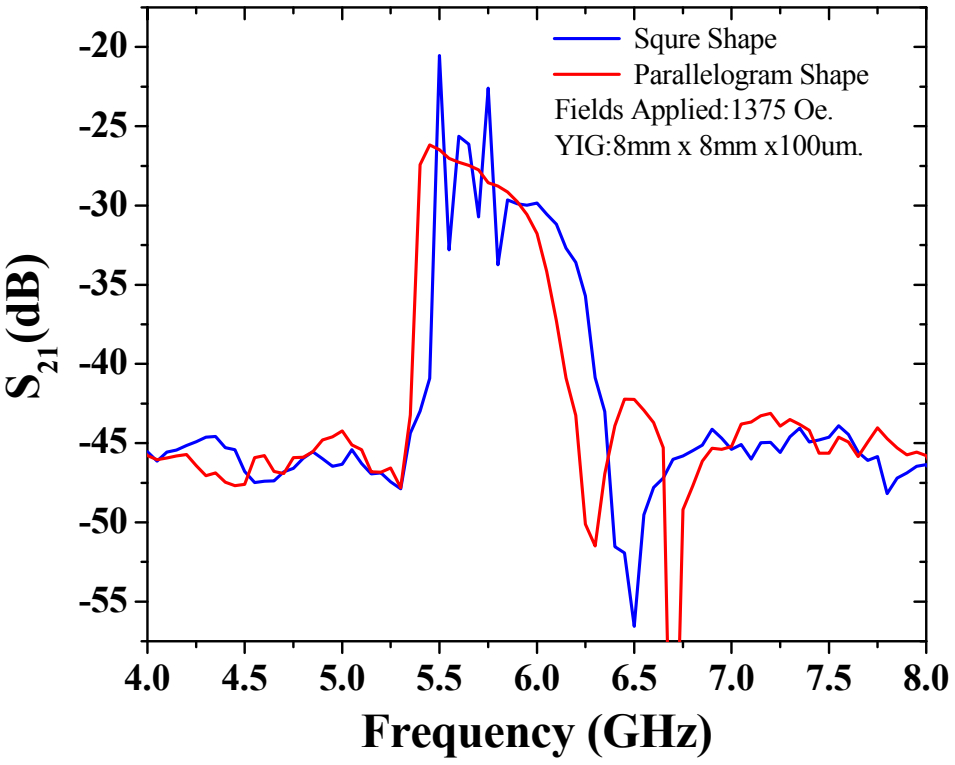

(b)

Figure 3.3: The comparison of the MSBVWs excited in a non-structured rectangular and a parallelogram YIG thin film with (a). simulated, (b) experimental results.

3.3 Propagation Characteristics of MSVWs in 1-D Magnonic Crystal with Normal Incidence

The above-mentioned analytical approach based on Walker's equation[9] was used to calculate the band structures of the MSVWs in 1-D MC at normal incidence. The calculated results were then verified experimentally. The validity of the analytical approach in determining and identifying the bandgaps of MSVWs in structures with periodic variation in YIG thin film thickness was demonstrated.

3.3.1 Band Structures Calculation and Verification

Fig. 3.5 shows the calculated band structure of the MSFVW by using the theoretical approach reported in Ref. [9] of a 1-D MC with geometrical parameters: $d_1 = 10$ μm, $d_2 = 5$ μm, $a_1 = 5$ μm, and $a_2 = 5$ μm, where d_1,

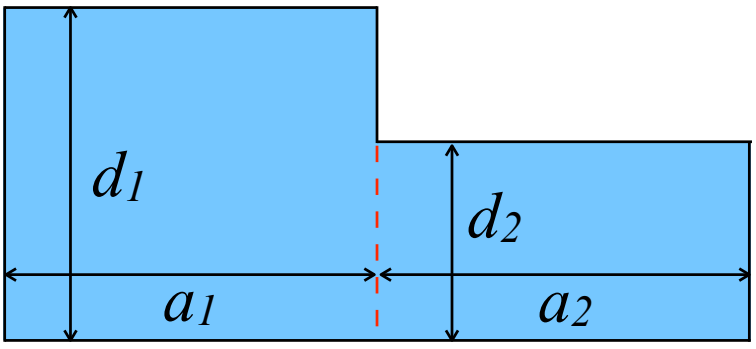

Figure 3.4: Unit cell in a 1-D MC. d_1 and d_2 are the thicknesses of non-etched and etched magnetic layer, respectively. a_1 and a_2 are the widths of non-etched and etched layers, and the lattice constant $a = a_1 + a_2$.

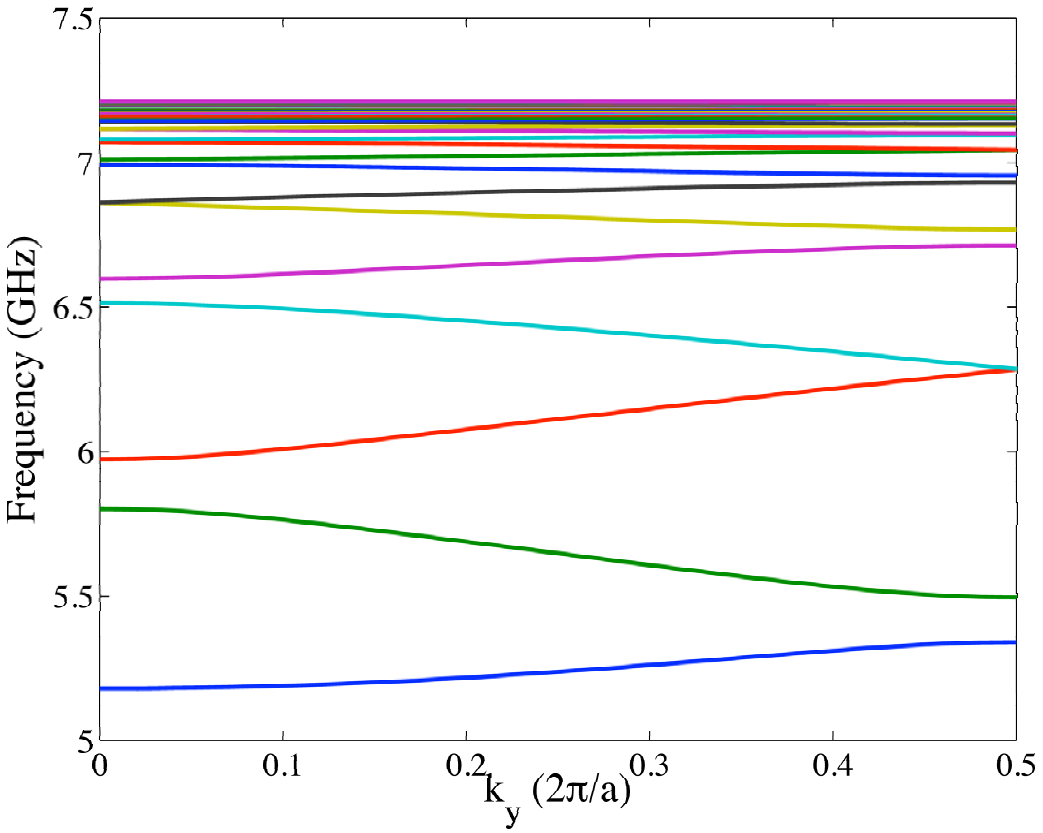

Figure 3.5: Band structure of a 1-D magnonic crystal for MSFVW with parameters of $M_s = 140\ G$, $H_0 = 1850$ Oe, $n = 2$, $d_1 = 10\ \mu$m, $d_2 = 5\ \mu$m, $a_1 = 5\ \mu$m, and $a_2 = 5\ \mu$m.

d_2, a_1, and a_2 are defined in Fig. 3.4. The band structure clearly shows the bandgaps expected in a MC.

As mentioned previously, the 1-D MC was designed and fabricated using standard photolithographic technique. To suppress unwanted fluctuations due to the reflections from sample edges, a parallelogram shape was etched on a square YIG thin film sample and the periodic channel structure was thereafter fabricated. The schematic of the designed 1-D MC is shown in Fig. 3.6(a). The dimension of a unit cell is illustrated in Fig. 3.4. The period length of the unit cell a is 200 μm, with the etched channel width a_2 of 50

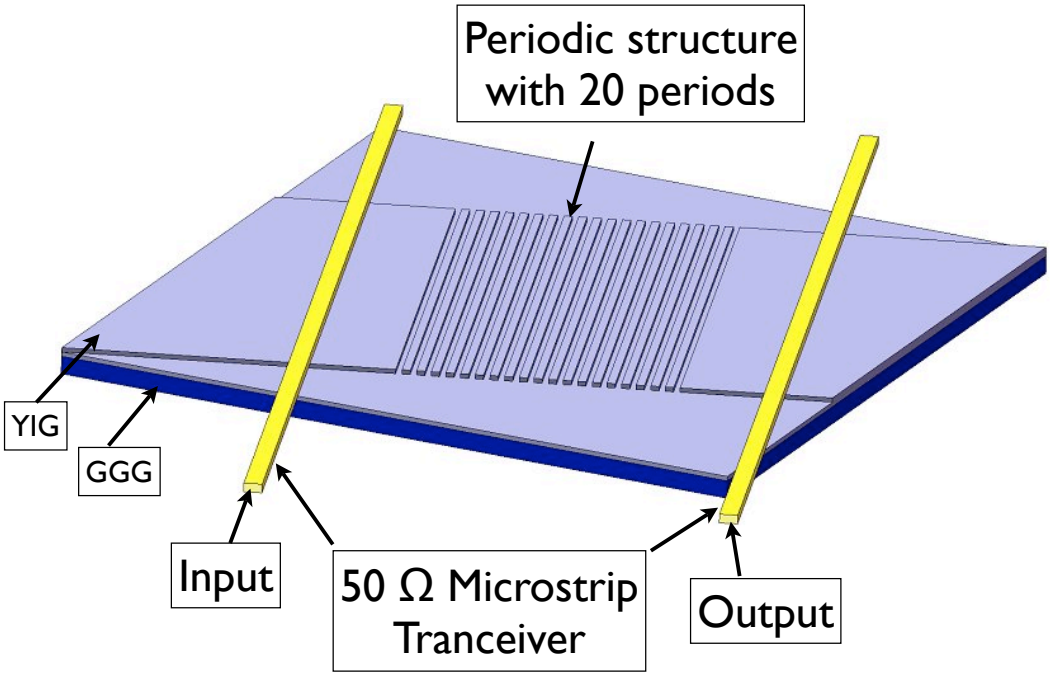

(a)

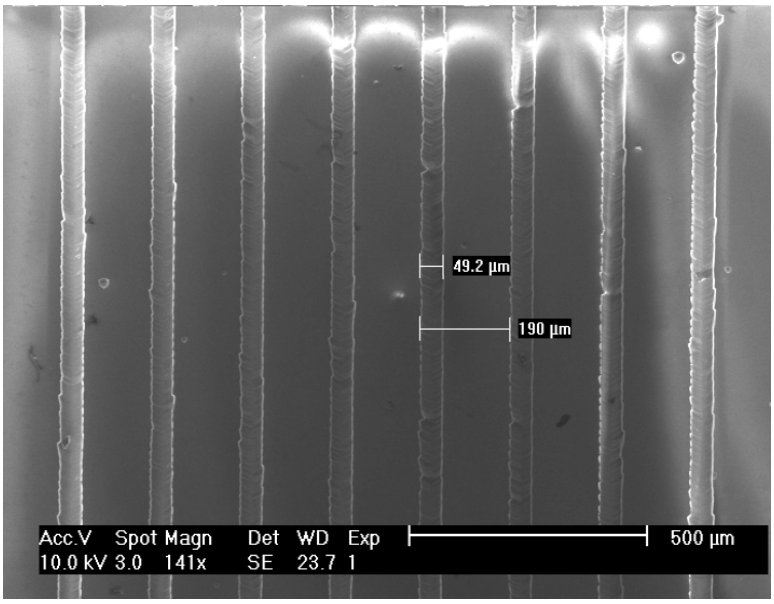

(b)

Figure 3.6: (a). The 3-D model of the 1-D MC sample; (b). the SEM image of the 1-D MC structure.

μm , and height of the etched channel d_2 of 65 μm after etching off 35 μm. The SEM image is shown in Fig. 3.6(b).

The MSWs were excited and received by mounting the 1-D MC upon a delay line structure. The arrangement for excitation and reception of the MSFVWs and MSBVWs is shown in Fig. 3.7, in which K represents the wave vector and H_0 the direction of the external bias fields generated from the permanent magnet pairs.

The analytical results were first compared with the early results for band gaps reported by others [29]. In [29], the experimental results suggest that the bandgaps fall approximately at 7.160, 7.120, 7.070, and 7.030 GHz. Fig. 3.8 shows the bandgaps (circled frequencies) predicted using our method, namely, 7.157, 7.133, 7.091, and 7.024 GHz. Clearly, the results calculated by our method are in good agreement with that reported in [29].

A series of experiments at different bias magnetic fields were also carried out on MSBVWs and MSFVWs. They consistently showed very good agreement between the experimental and the calculated results. The effect of magnonic bandgaps on the MSBVW is shown in Fig. 3.9. The 20 unit cells MC used was fabricated using photolithography and wet etching. A pair of 50 Ω transmission lines with 5 mm separation was used as a transceiver. The measured spectrum of Fig. 3.9(a) obtained at the bias field of 1,650 Oe clearly shows the three bandgaps, A, B, and C, created by the MC.

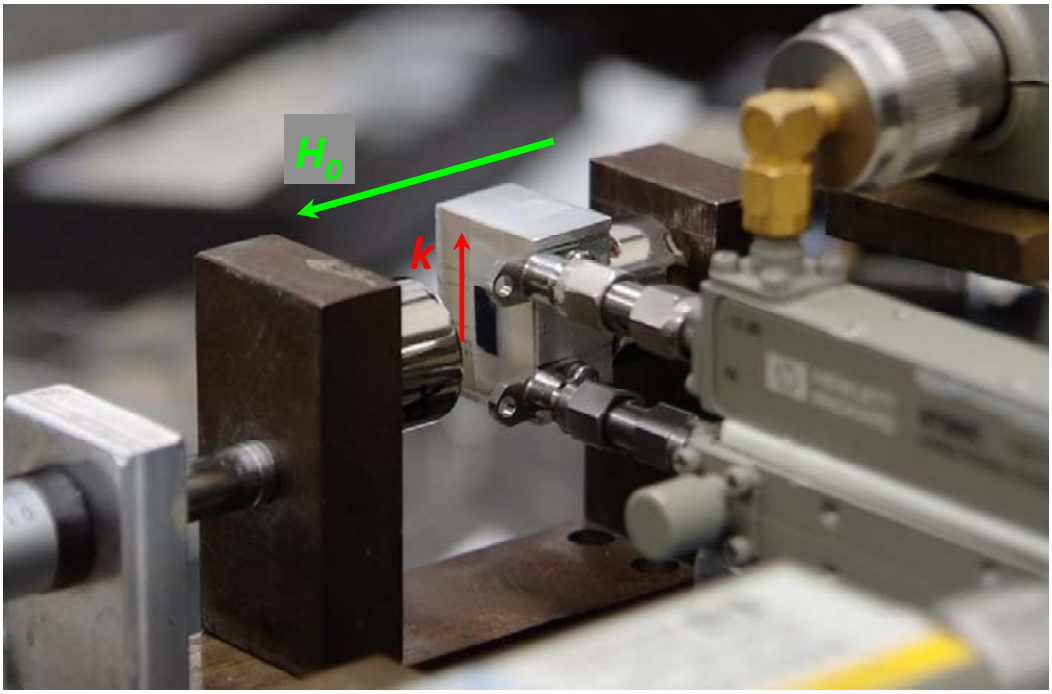

(a)

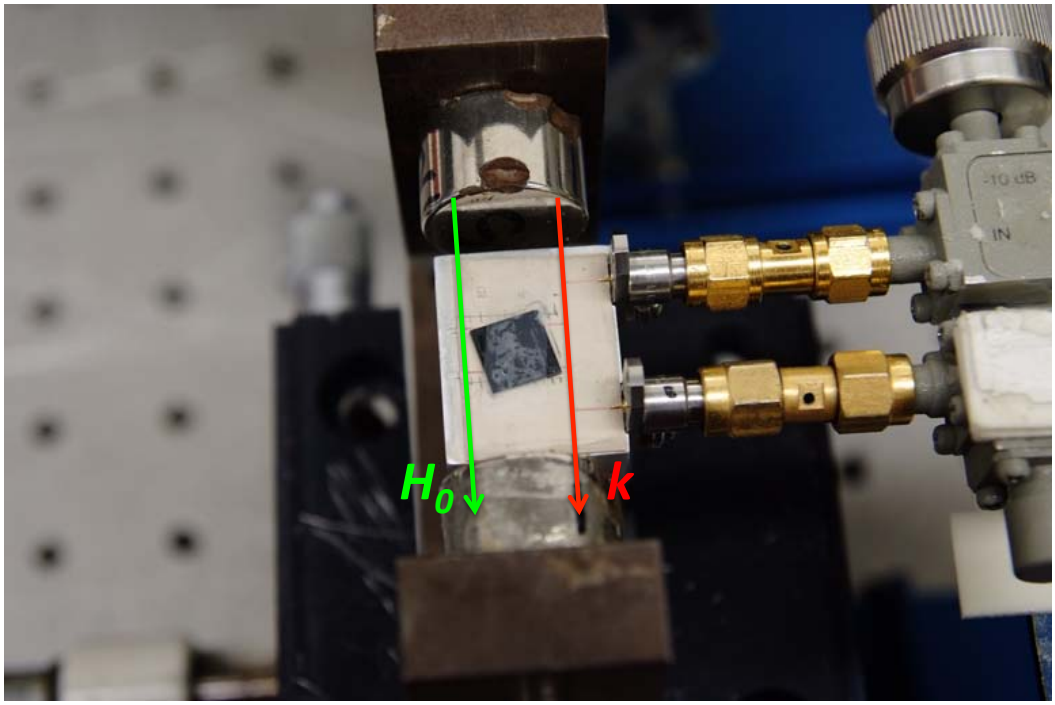

(b)

Figure 3.7: Experimental setup for (a) MSFVWs, and (b) MSBVWs excitation and bandgap tunability test.

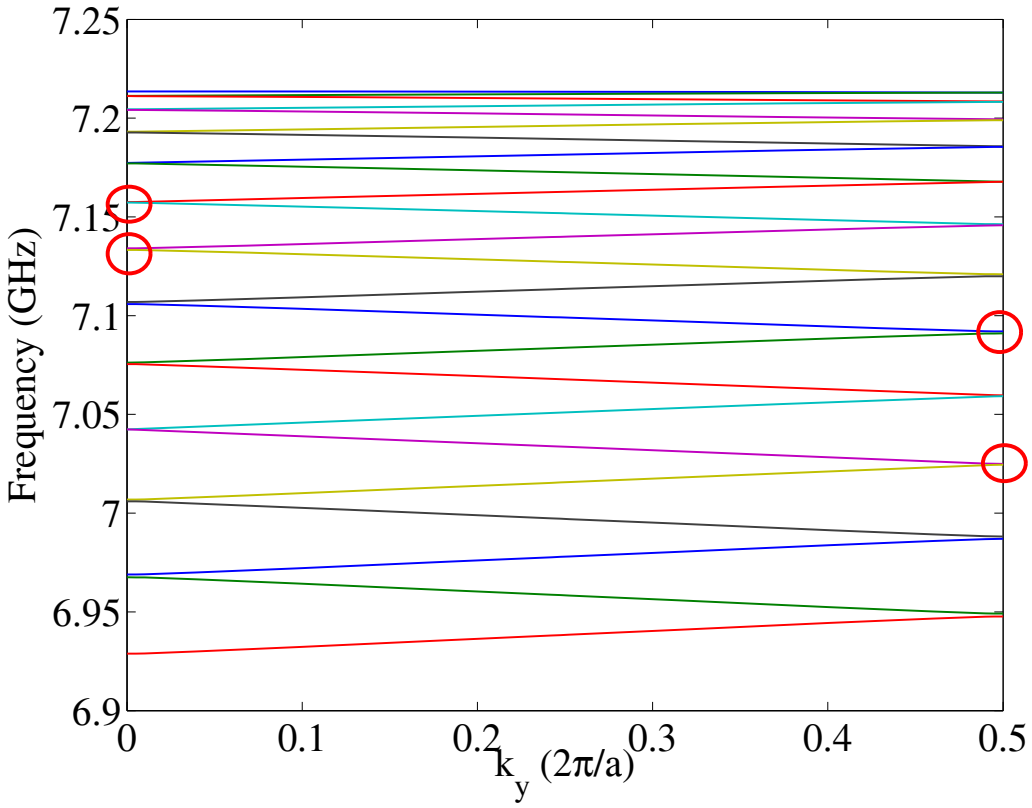

Figure 3.8: The band structure calculated by our approach with the geometry and material parameters presented in [29].

The calculated band structure of the MC with nearly identical parameters presented in Fig. 3.9(b) clearly shows the existence of bandgaps. The bandgaps A', B', and C' are the first three calculated bandgaps corresponding to the measured bandgaps A, B, and C, respectively, in Fig. 3.9(a). Table 3.1 lists the frequencies of the first three magnonic bandgaps. Clearly, an excellent agreement between the experimental and calculated results was obtained.

Experiments were also conducted to excite MSFVWs in 1-D MC. The measured spectrum of MSFVWs at a bias field of 1,350 Oe is shown in Fig. 3.10(a). A comparison between Fig. 3.10(a) and the calculated band structure shown

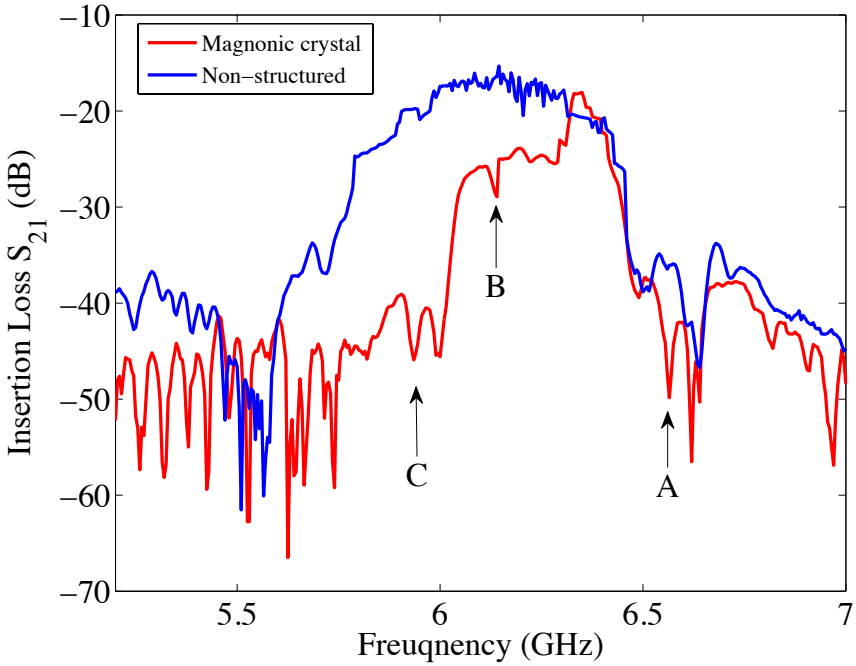

(a) Experimental result of 1-D MC with bias magnetic field of 1650 Oe.

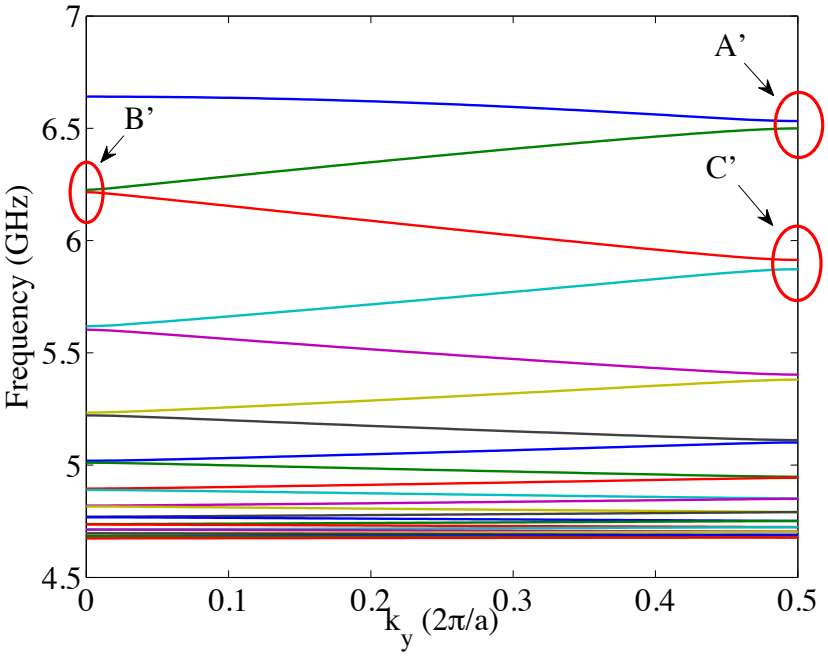

(b) Theoretical result of 1-D MC with bias magnetic field of 1650 Oe.

Figure 3.9: (a) Measured spectrum of MSBVW in a MC with the following parameters: $M_s = 140\ G$, $H_0 \approx 1650$ Oe, $d_1 = 100\ \mu$m, $d_2 \approx 80\ \mu$m, $a_1 \approx 85\ \mu$m, and $a_2 \approx 75\ \mu$m. (b) Calculated band structure of MSBVW in the 1-D MC with the following parameters: $M_s = 140\ G$, $H_0 = 1650$ Oe, $n = 2$, $d_1 = 100\ \mu$m, $d_2 = 80\ \mu$m, $a_1 = 85\ \mu$m, and $a_2 = 75\ \mu$m.

Table 3.1: Comparison of the first two bandgap frequencies between experimental and theoretical results with bias magnetic field H_0 of 1,650 Oe.

	Mid-gap Frequency (GHz)		
Experimetal	A: 6.565	B: 6.14	C: 5.935
Calculated	A': 6.516	B': 6.216	C': 5.893
Difference (%)	0.75%	1.23%	0.71%

Table 3.2: Comparison of the first two bandgap frequencies between experimental and theoretical results with bias magnetic field H_0 of 1,350 Oe.

	Mid-gap Frequency (GHz)	
Experimetal	A: 3.94	B: 4.29
Calculated	A': 3.9545	B': 4.3235
Difference (%)	0.37%	0.78%

in Fig. 3.10(b) as listed in Table 3.2 also shows a close agreement between the two.

The tunability of the MSBVWs and that of the MSFVWs were studied subsequently. As shown in Fig. 3.11(a), by increasing the bias magnetic field from 1,150 Oe to 2,030 Oe, three bandgaps of the MSFVWs marked A, B and C, respectively, were identified. The tunability of the bandgaps toward a higher frequency with the increase of the bias magnetic field was also clearly demonstrated. Similarly, the tunability of the bandgaps marked D-G of the MSBVWs in a MC under different bias magnetic fields is shown in Fig. 3.11(b). The comparison between the experimental and theoretical results is presented in Table 3.3 and a good agreement between the two results was achieved, suggesting the validity of the approach biased on Walker's equation in bandgaps calculation at normal incidence.

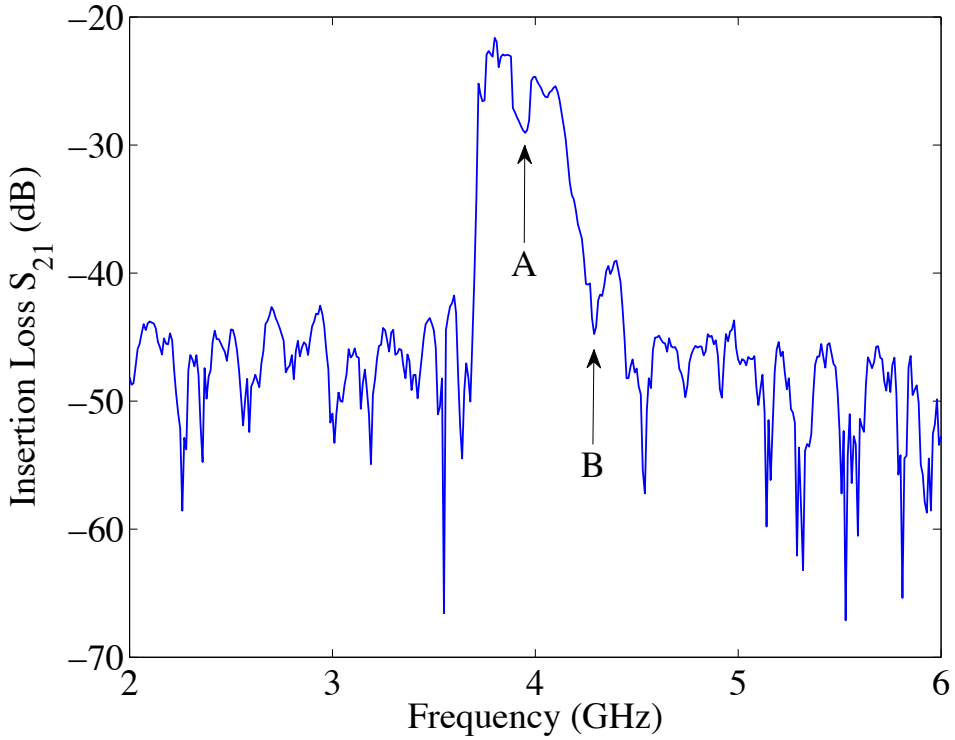

(a) Experimental result of 1-D MC with bias magnetic field of 1350 Oe.

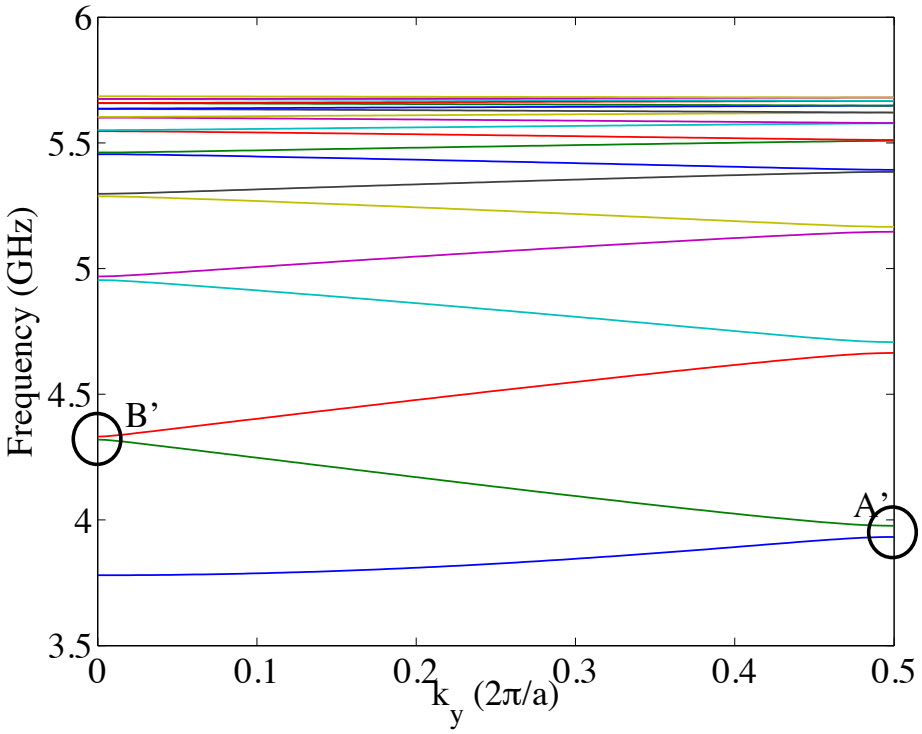

(b) Theoretical result of 1-D MC with bias magnetic field of 1350 Oe.

Figure 3.10: The experimental and theoretical results of MSFVW propagating in 1-D MC with bias magnetic field, H_0, of 1350 Oe.

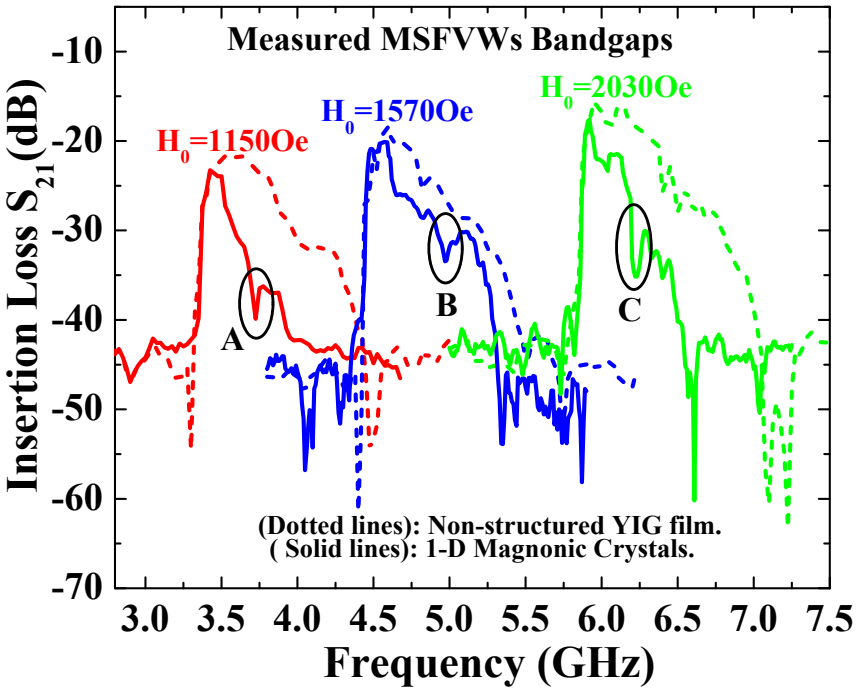

(a)

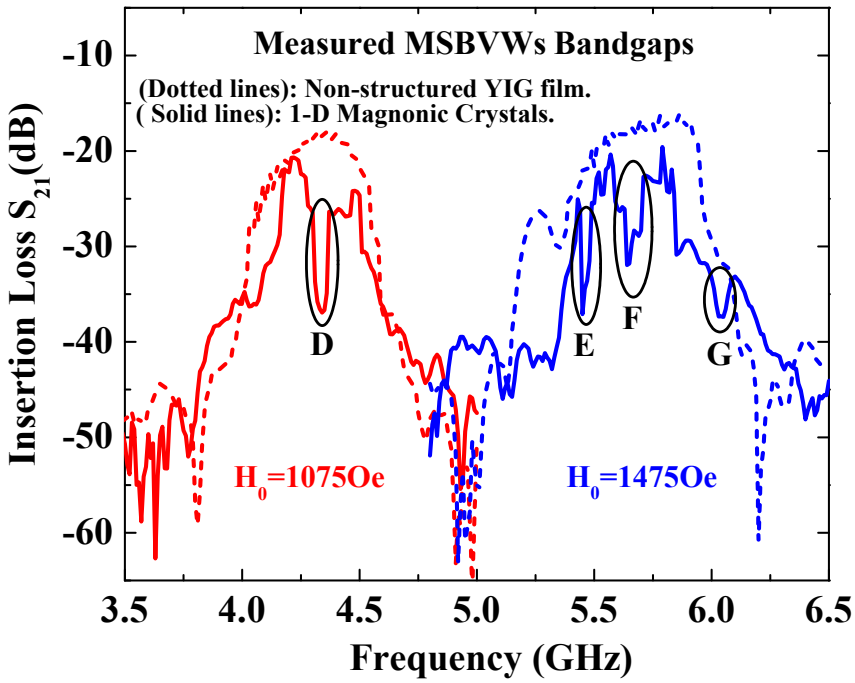

(b)

Figure 3.11: Measured bandgaps under different magnetic fields of (a). MSFVW, bandgaps marked as A-C and (b). MSBVWs, bandgaps marked as D-G.

Table 3.3: Comparison between measured MSFVWs and MSBVWs in a 1-D MC with analytically calculated Results. UNIT:[GHz]

	MSFVWs Mid-gap Freq.			MSBVWs Mid-gap Freq.			
Experimetal	A: 3.73	B: 4.98	C: 6.23	D:4.33	E:5.45	F:5.64	G:6.05
Calculated	A': 3.76	B': 4.89	C': 6.23	D':4.21	E':5.11	F':5.71	G':5.99
Difference (%)	0.93%	1.82%	1.08%	2.8%	1.08%	1.19%	0.93%

In conclusion, the validity of the eigenvalue equations derived from Walker's equation for analysis of the propagation characteristics of MSVWS in 1-D MC with periodic variation in magnetic layer thickness has been established. An excellent agreement between the calculated bandgaps for the MSVWs using the proposed approach and the experimental results has been achieved. Tuning of the bandgaps in MSFVWs and MSBVWs via a bias magnetic field has also been demonstrated.

3.4 Propagation Characteristics of MSVWs in 1-D MC with Oblique Incidence

In the last Section, the results of theoretical and experimental studies on the bandgaps of MSVWs in 1-D MC with periodic variation in YIG/GGG layer thickness at normal incidence [9] are presented. The results of subsequent theoretical and experimental studies for the case of oblique incidence [10] are presented in this Section.

3.4.1 Bandgaps Calculation and Verification

The relative propagation direction of the incident MSVWs with respect to the y-oriented 1-D MC is shown in Fig. 3.12 in which k and θ are the wave number and the incident angle of the MSVWs, respectively. The bias magnetic field H_0 is applied along the y or the z direction to excite the MSFVWs or MSBVWs, respectively.

The bandgaps of the MSVWS in a 1-D MC at oblique incidence were calculated by using the approach reported in [10]. In order to elucidate the propagation characteristics at different incident angles, 2-D band structures were constructed to present the calculated results. Fig. 3.13 and Fig. 3.14 are such 2-D band structures for the MSFVWs and the MSBVWs, respectively, with the incident angle ranging from -45° to 45° in the 1-D MC with unit cell

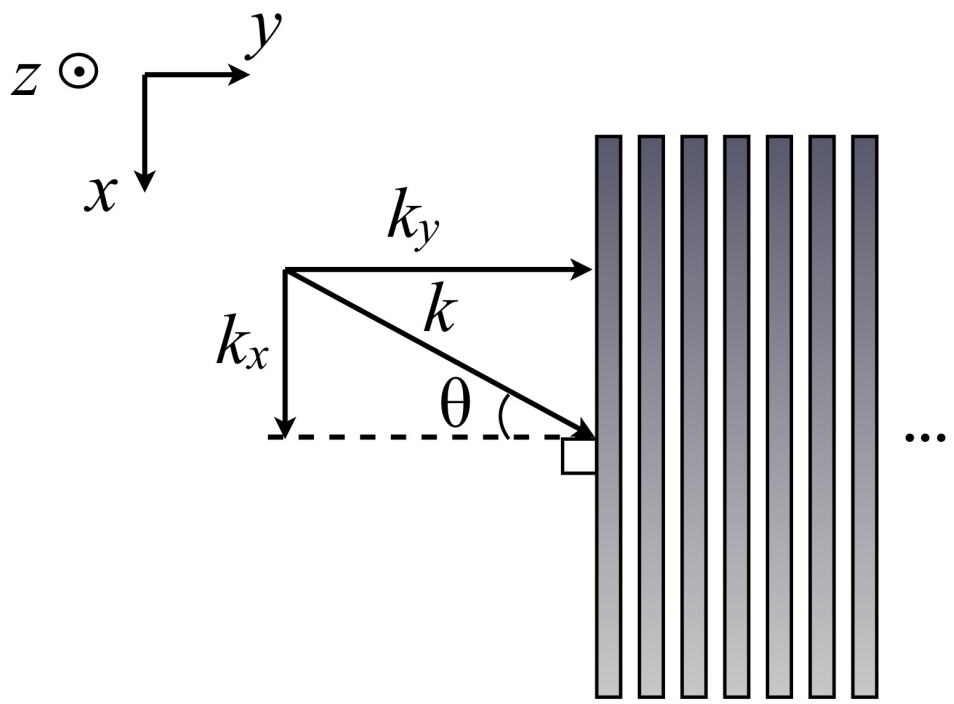

Figure 3.12: Oblique incidence of MSVWs upon a 1-D MC, when k is the wave number of the MSVWs and θ is the incident angle.

dimensions of $a_1 = 50$ μm,$a_2 = 50$ μm, $a = 100$ μm , $d_1 = 100$ μm, and $d_2 = 80$ μm as shown in Fig. 3.4.

The theoretical approach enabled efficient calculation of the band structures at different θ together with the corresponding bandgap information clearly demonstrated on the 2-D band structures. For example, from Fig. 3.13 for the MSFVWs, the first band (in blue to green) can be readily found to be from 5.531 GHz to 6.453 GHz at $\theta = 0^\circ$ and from 5.531 GHz to 6.804 GHz at $\theta = 45^\circ$, respectively. Similarly, the second band (in green to orange) are readily found to be from 6.597 GHz to 7.152 GHz at $\theta = 0^\circ$ and from 6.935 GHz to 7.152 GHz at $\theta = 45^\circ$, respectively. Furthermore, Fig. 3.15(a) and

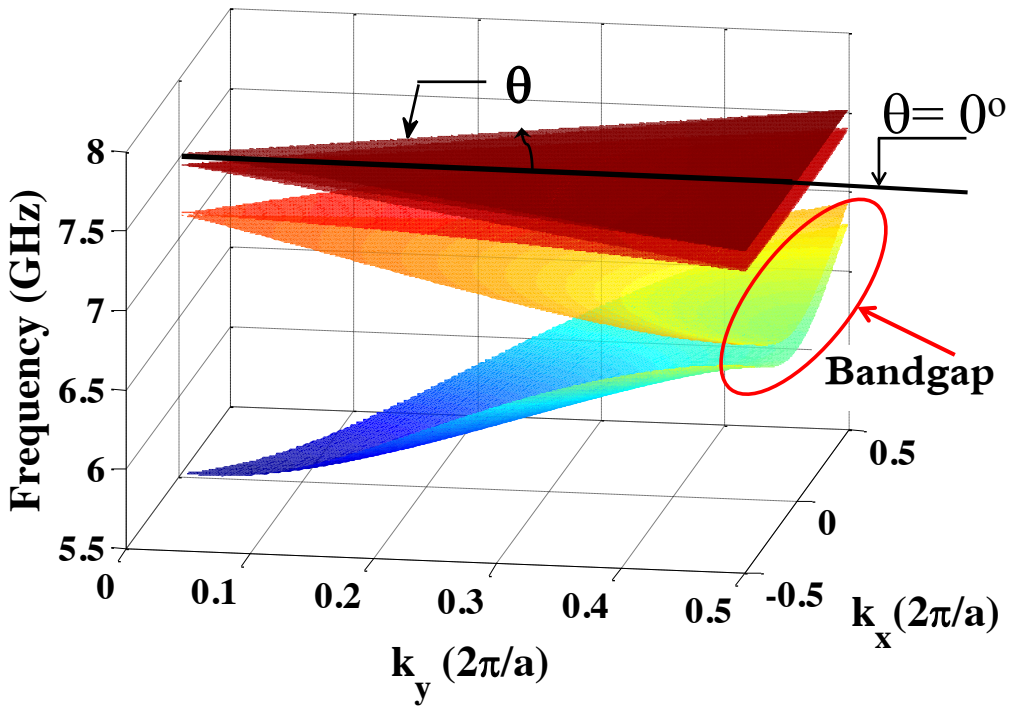

Figure 3.13: 2-D band structure of the MSFVWs in a 1-D MC. The range of incident angle θ is from -45° to 45°. The dimensions of the unit cell are a_1 = 50 μm, a_2 = 50 μm, a = 100 μm , d_1 = 100 μm, and d_2 = 80 μm as shown in Fig. 3.4. The saturation magnetization $4\pi M_s$is 1760 G. The bias magnetic field is 1975 Oe.

3.15(b) clearly show the variation of bandgaps at versus the incident angle for the MSFVWs and the MSBVWs, respectively. The mid-gap frequency of the bandgap increases as the incident angle increases. Experiments were thereafter conducted to verify the correctness of the calculated results [10].

3.4.2 MSFVWs, Incident Angle θ = 0°, 14°, and 25°; Bias magnetic field H_0=1650Oe

Experiments were first carried out to verify the calculated bandgaps of the MSVWs propagating in the 1-D MC as shown in Fig. 3.16(a) with oblique

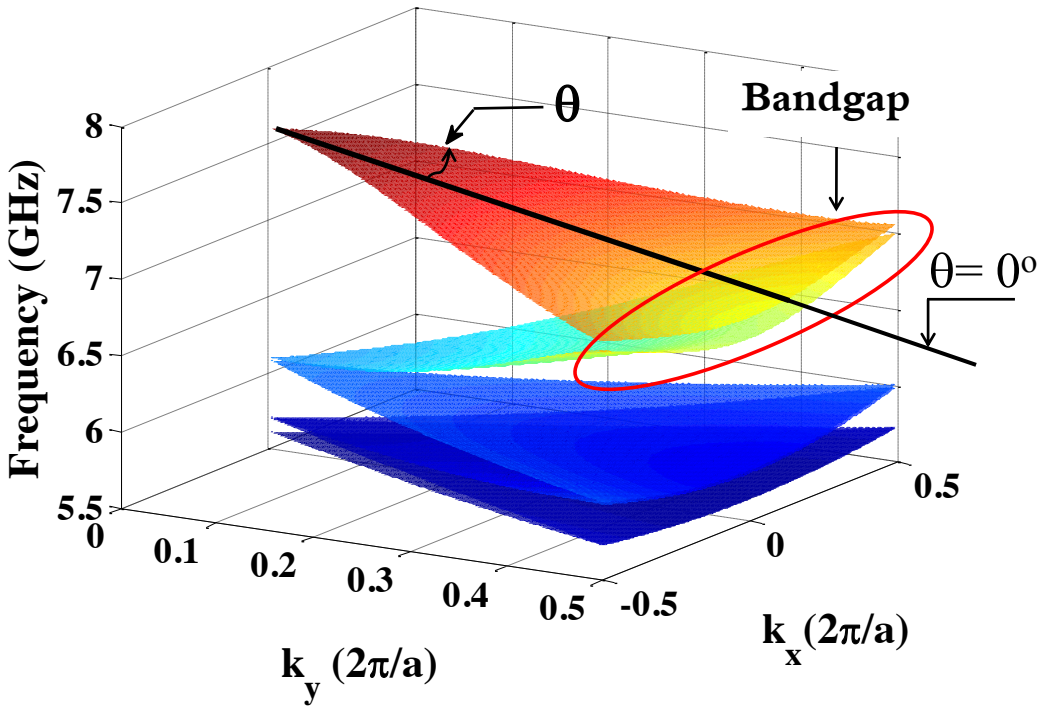

Figure 3.14: 2-D band structure of the MSBVWs in a 1-D MC. The range of incident angle θ is from -45° to 45°. The dimensions of the unit cell, the saturation magnetization, and the bias magnetic field are given in the caption of Fig. 3.13.

incidence using the same measurement setup as the one used previously [9]. The periodic channels of the 1-D MC sample was formed by wet etching upon the YIG/GGG thin-film with a thickness of 100 μm. The unit cell of the periodic structure has the dimensions of $a_1 = 90\mu$m, $a_2 = 70\mu$m, $d_1 = 100$ μm, and $d_2 = 80\mu$m . Variation of the incident angle was accomplished by rotating the 1-D MC sample while maintaining the position of the microstrip transducers and the direction of the bias magnetic field (see Fig. 3.16(b)). As shown in Figs. 3.17 (a), (c), and (e), the circled dips marked with letters A to D are the measured bandgaps of the MSFVWs with the incident angles of 0°, 14°, and 25°, respectively, at the bias magnetic field of 1,650 Oe. The

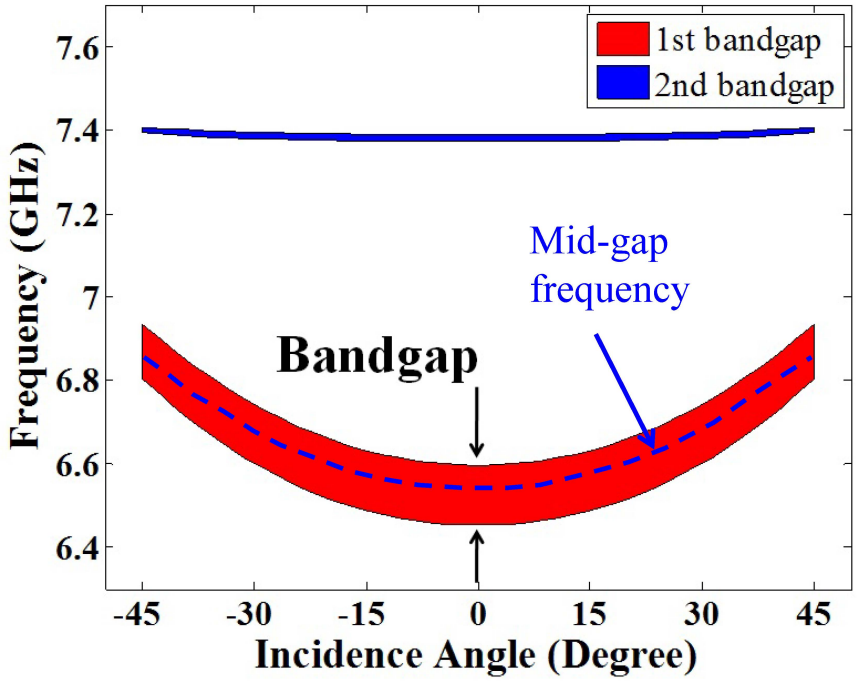

(a)

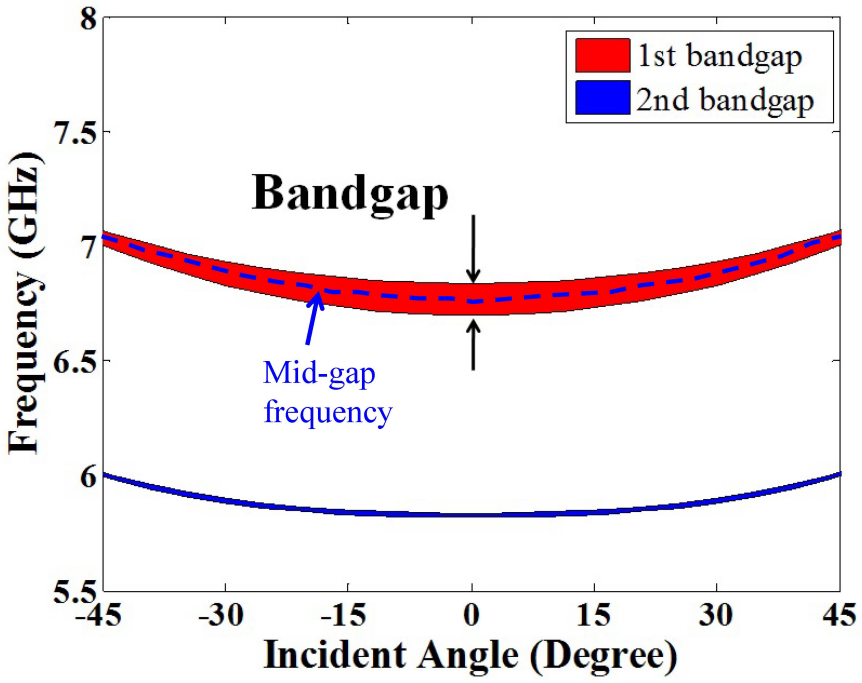

(b)

Figure 3.15: Variation of bandgaps with the incident angle:(a) MSFVWs,(b) MSBVWs. The mid-gap frequency of the bandgap increases as the incident angle increases, while the width of the bandgap decreases as the incident angle increases.

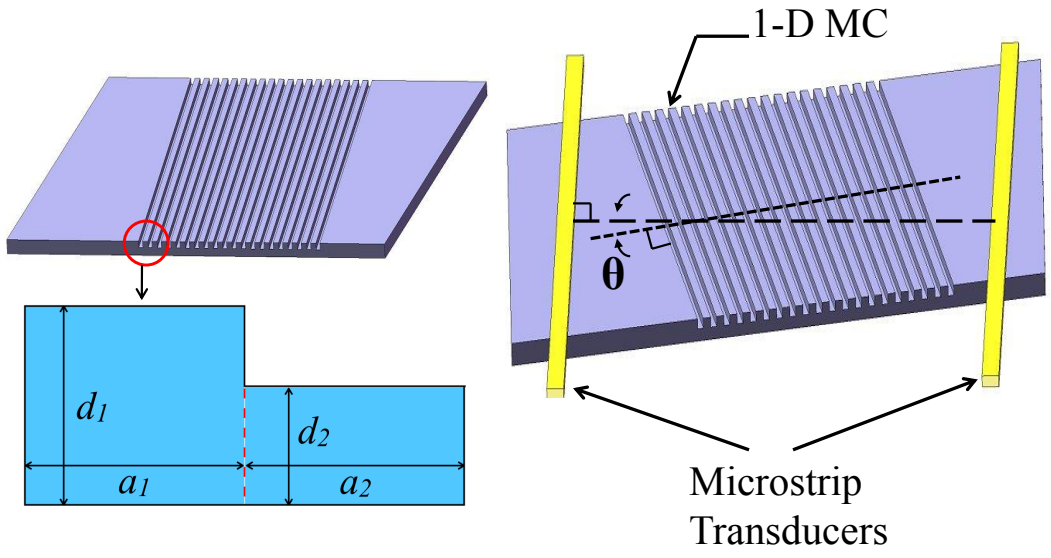

Figure 3.16: (a) The unit cell of a 1-D MC with periodic variation in layer thickness. a_1 and a_2, and d_1 and d_2 are, respectively, the width and the thickness of unetched and etched parts of the YIG film. (b) Geometry of a 1-D MC and microstrip transducers.

corresponding calculated band structures are shown in Figs. 3.17 (b), (d), and (f), respectively, with the bandgaps marked A' to D'. A comparison between the experimental and the theoretical results is presented in Table 3.4. Note that a very slight difference (<1%) between the two results was observed.

3.4.3 MSBVWs, Incident Angle θ = 0°, 14°, and 25°; Bias magnetic field H_0= 1,385 Oe

Similarly, experiments were carried out to measure the bandgaps of the MSBVWs at the incident angles of 0°, 14°, and 25°, and the bias magnetic field of 1,385 Oe. Variation of the incident angle was also accomplished in the same manner as in the experiments with the MSFVWs. Fig. 3.18(a) shows

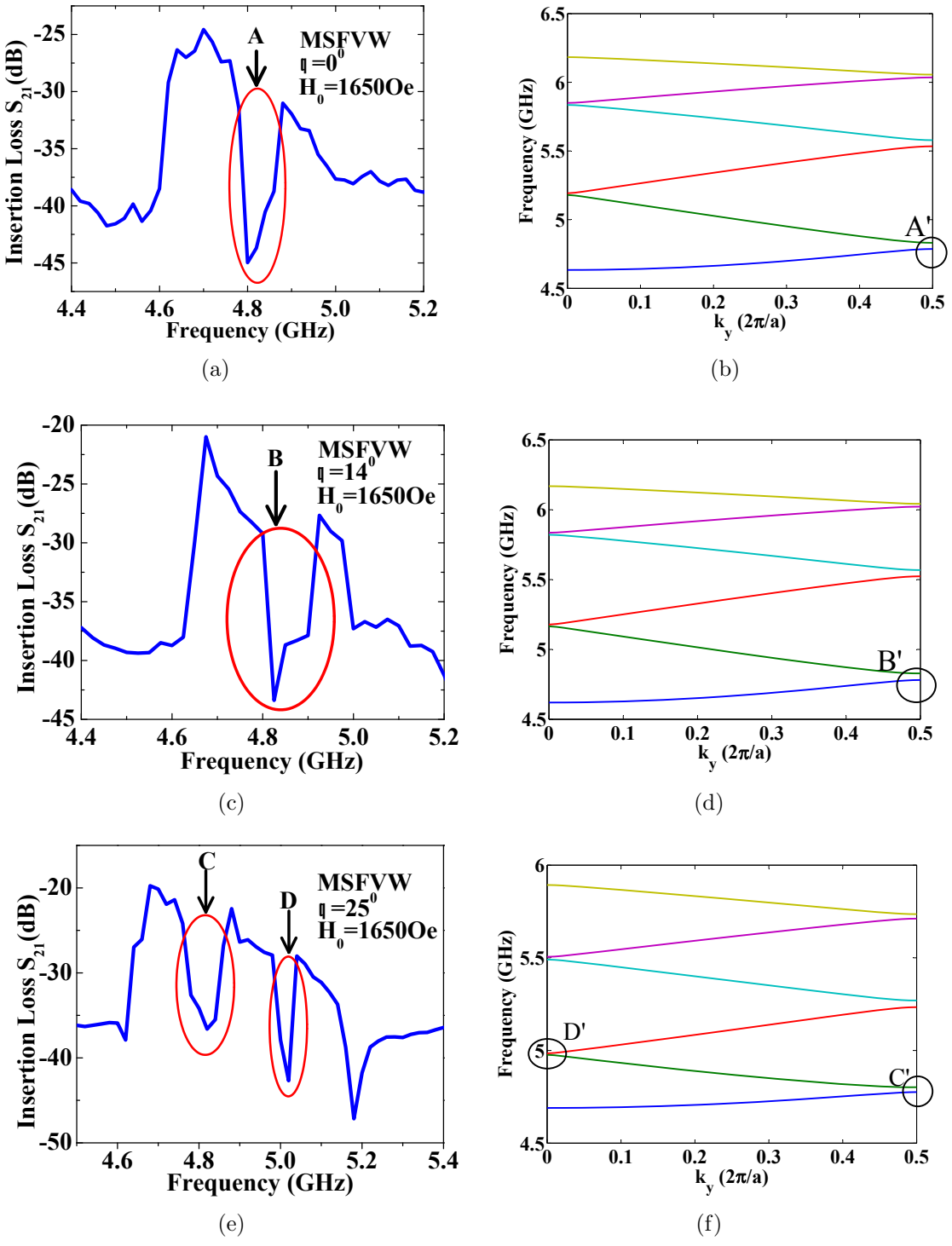

Figure 3.17: Experimental and calculated results of the MSFVWs propagating in a 1-D MC with incident angle (a), (b):$\theta = 0°$; (c), (d):$\theta = 14°$; (e), (f):$\theta = 25°$ under a bias magnetic field of 1,650 Oe. (a) Experimental Resutls,$\theta = 0°$; (b) Calculated Results $\theta = 0°$; (c) Experimental Resutls,$\theta = 14°$; (d) Calculated Results $\theta = 14°$; (e) Experimental Resutls,$\theta = 25°$; (f)Calculated Results $\theta = 25°$.

Table 3.4: Calculated and Measured MSFVWS Bandgaps Comparison

	Mid-gap Frequency(GHz)			
Incident Angle	$\theta = 0°$	$\theta = 14$ °	$\theta = 25$ °	
Experimetal	A: 4.82	B: 4.83	C: 4.81	D:5.01
Calculated	A': 4.80	B': 4.82	C': 4.78	D':4.98
Difference (%)	0.40%	0.20%	0.62%	0.60%

the measured bandgaps of the MSBVWs with the incident angle of 0° and the bias magnetic field of 1,385 Oe. The calculated band structures and bandgaps are shown in Fig. 3.18 (b). The measured and calculated bandgaps of the MSBVWs with the incident angle of 14°, and 25° are shown in Fig. 3.18 (c) and (e), and (d) and (f), respectively. Again, as shown in Table 3.5, an excellent agreement between the experimental and the theoretical results was achieved.

Table 3.5: Calculated and Measured MSBVWS Bandgaps Comparison

(a) $\theta = 0°$

Angle	Mid-gap Frequency(GHz)				
Experimetal	A: 4.620	B: 4.99	C: 5.172	D:5.461	E:5.761
Calculated	A': 4.721	B': 4.891	C': 5.162	D':5.482	E':5.760
Difference (%)	2.16%	2.00%	0.19%	0.36%	0%

(b) $\theta = 14°$

Angle	$\theta = 14°$, Mid-gap Frequency(GHz)				
Experimetal	F: 5.044	G:5.243	H: 5.436	I:5.723	J:5.787
Calculated	F': 5.043	G': 5.242	H': 5.446	I':5.656	J':5.804
Difference (%)	0.02%	0.02%	0.18%	1.17%	0.29%

(c) $\theta = 25°$

Angle	$\theta = 14°$, Mid-gap Frequency(GHz)					
Experimetal	K: 5.04	L:5.24	M: 5.36	N:5.36	O:5.68	P:5.84
Calculated	K': 5.13	L': 5.29	M': 5.43	N':5.59	O':5.72	P'=5.81
Difference (%)	1.78%	1.00%	1.30%	0.54%	0.70%	0.51%

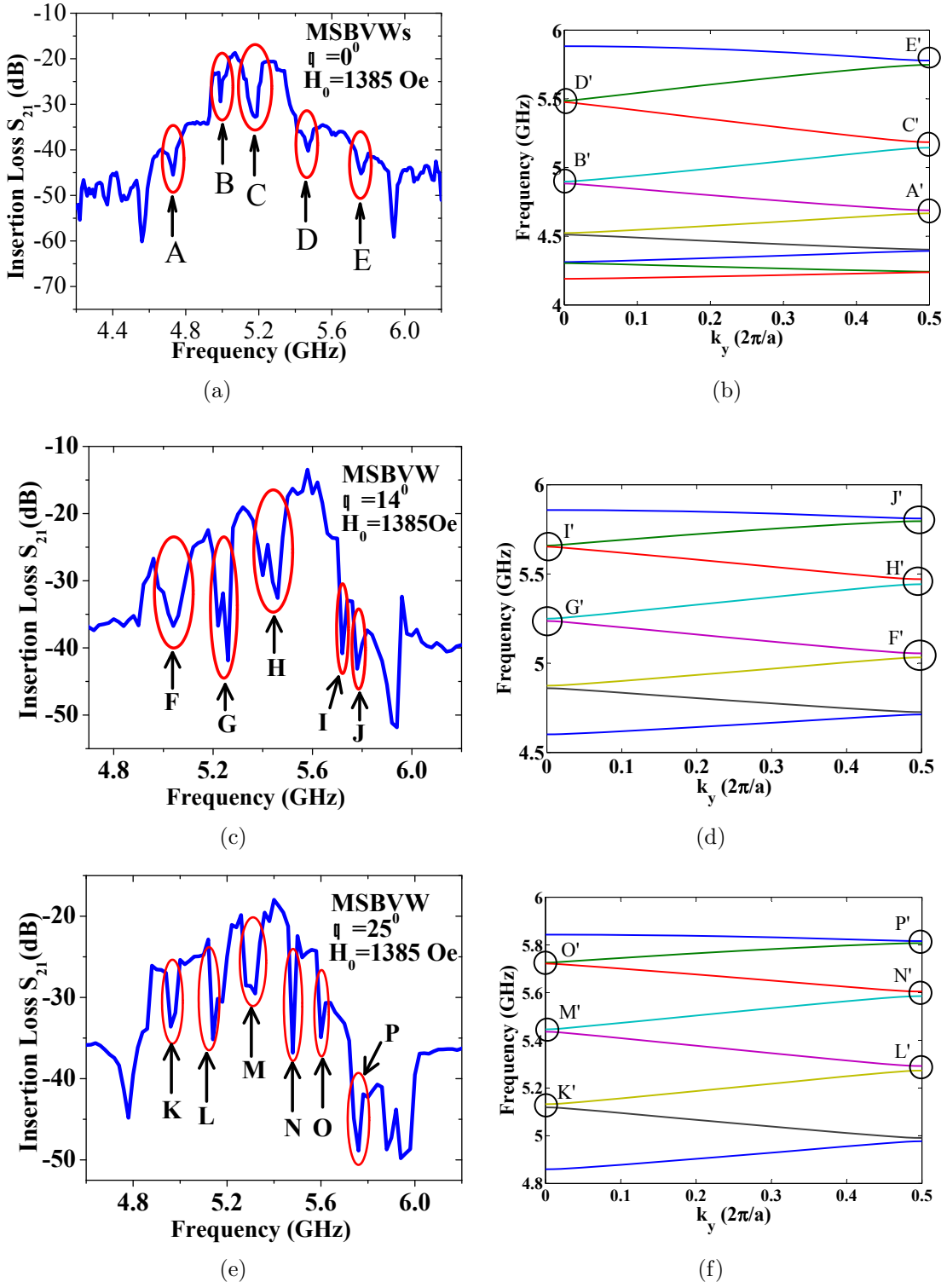

Figure 3.18: Experimental and calculated results of the MSBVWs propagating in a 1-D MC with incident angle (a), (b):$\theta = 0°$; (c), (d):$\theta = 14°$; (e), (f):$\theta = 25°$ under a bias magnetic field of 1,385 Oe. (a) Experimental Resutls,$\theta = 0°$; (b) Calculated Results $\theta = 0°$; (c) Experimental Resutls,$\theta = 14°$; (d) Calculated Results $\theta = 14°$; (e) Experimental Resutls,$\theta = 25°$; (f)Calculated Results $\theta = 25°$.

In summary, as shown in Tables 3.4 and 3.5, the measured bandgaps of the MSFVWs and the MSBVWs at the three incident angles of 0°, 14°, and 25° are all in excellent agreement with the calculated results using the approach reported in Ref. [10]. One additional bandgap was created as the incident angle was increased from 14°, and 25°. Thus, the capability of the new analytical approach for calculation of the bandgaps of both types of the MSVWs at oblique incidence in the 1-D MCs has been clearly demonstrated.

3.5 Propagation Characteristics of MSVWs in 2-D Magnonic Crystal

In Sections 3.3 and 3.4, the propagation characteristics of the MSVWs in the 1-D MC at normal and oblique incidence [9, 10] are presented. The research was further extended to the propagation characteristics of the MSVWs in 2-D MCs, at normal and oblique incidence and the findings are presented in this Section.

3.5.1 Bandgaps Calculation and Verification

The theoretical approach based on Walker's equation [11] was again employed to analyze the 2-D MC band structure. Fig. 3.19 (a) and (b) show the geometrical profile of the 2-D MCs in square lattice used in the numerical

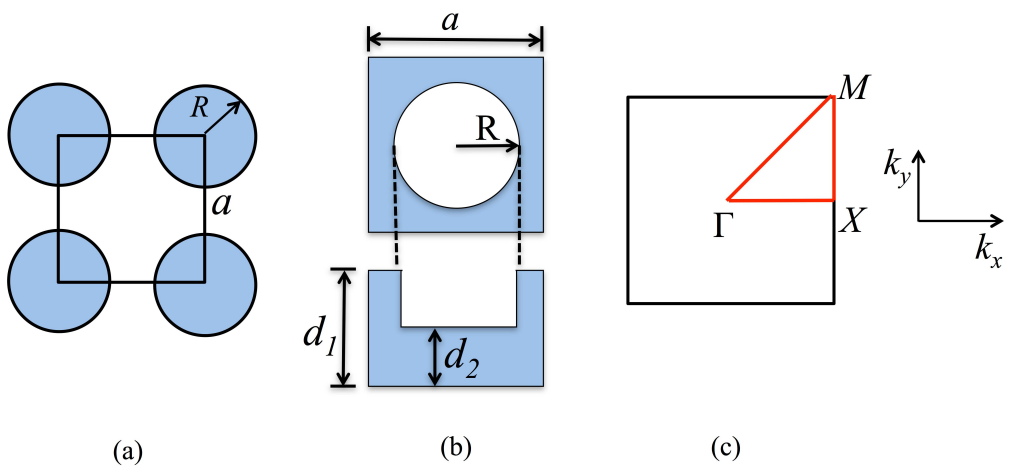

Figure 3.19: (a) Geometry and reduced first Brillouin zone in 2-D MCs of square lattice

calculation, in which a is the lattice constant, R is the radius of the etched hole, d_1 and d_2 are the thicknesses of unetched and etched YIG layer, respectively. The resulting band structure is presented along the first reduced Brillouin zone, Γ-X-M, as shown in Fig. 3.19(c), in which Γ: $k_x = 0$, $k_y = 0$, X: $k_x = \pi/a$, $k_y = 0$, and M: $k_x = \pi/a$, $k_y = \pi/a$.

Figs. 3.20(a)-(d) are the calculated band structures for MSVWs which show the first three passbands (PBs) and the first bandgap obtained with H_0 = 1,650 Oe, M_S = 1,750 Gauss for a YIG layer, with the geometric parameters: a = 200 μm, $R = 0.32a$, and d_1 = 100μm, and d_2 = 55 and 35 μm. Specifically, the colored lines represent the passbands in which the MSVWs can propagate through the periodic structure at different frequencies. The horizontal darkened bands designate the bandgaps in which the MSVWs cannot propagate in the MCs due to the destructive interference. Besides, the dispersion relations of the passbands are also readily obtained. As clearly

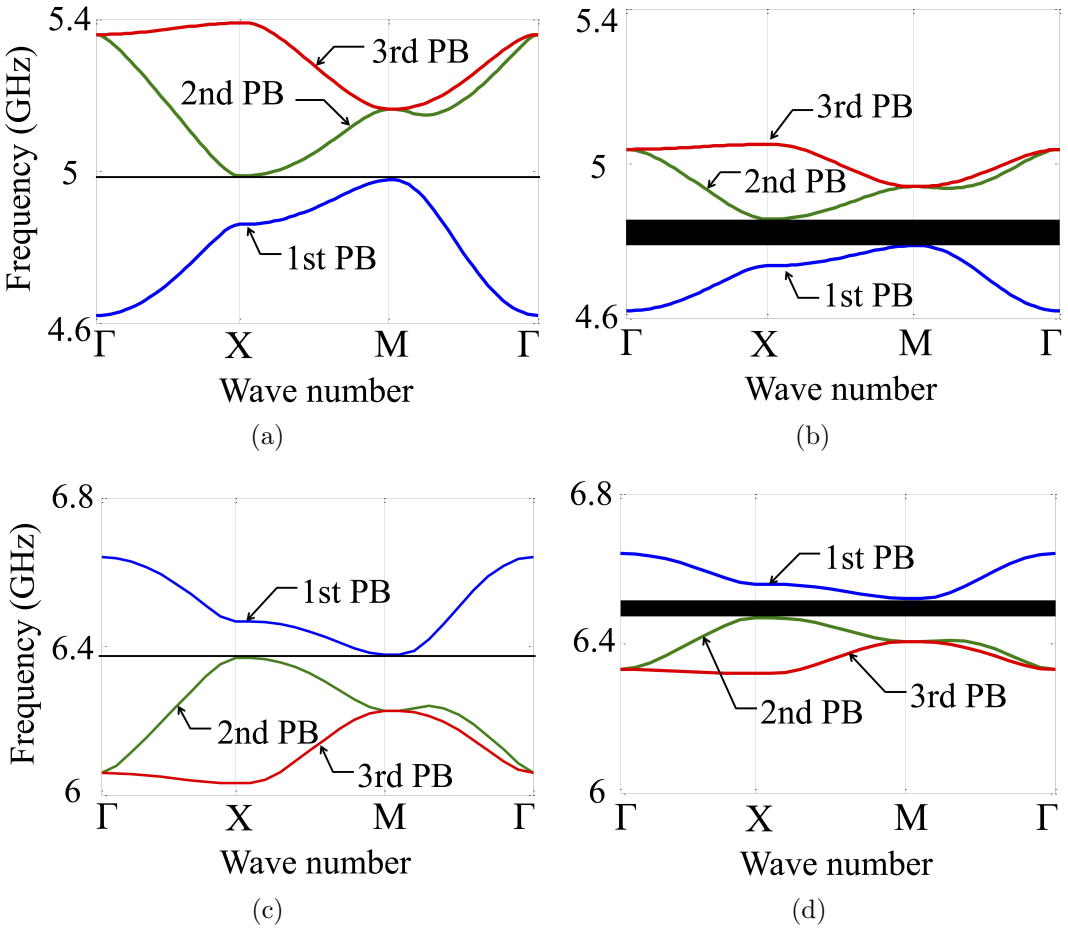

Figure 3.20: Calculated band structures of MSVWs in a 2-D MC at $H_0 = 1650$ Oe, $M_S = 1750$ Gauss, and the geometric parameters:$a = 200$ μm, $R = 0.32a$, and $d_1 = 100\mu$m, and the corresponding wave numbers:Γ: $k_x = 0$, $k_y = 0$; X: $k_x = 0.5(2\pi/a) = 157.08$ cm^{-1},$k_y = 0$; M: $k_x = k_y = 0.5(2\pi/a) = 157.08$ cm^{-1}: (a) MSFVWs, $d_2 = 55\mu$m, (b) MSFVWs, $d_2 = 35\mu$m, (c) MSBVWs, $d_2 = 55\mu$m, (d) MSBVWs, $d_2 = 35\mu$m.

seen from Figs. 3.20, the mid-gap frequency and the bandgap width change drastically as d_2 was varied from 55 to 35 μm. Therefore, the thickness variation achieved by varying d_2 is an important parameter to obtain the band structures desired.

Fig. 3.21(a) and (b) show the calculated bandgaps versus the incidence angle for the MSVWs. The blue line and the green line are for the first and the second bands, respectively. The area in between corresponds to the bandgap at respective incidence angle. It shows that at all incidence angles (-45° to 45°) a bandgap exists from 8.844 to 8.853 GHz for the MSFVWs and 5.891 to 5.935 GHz for the MSBVWs. This is in stark contrast to the case with the 1-D MCs. For example, at 6.5 GHz, the bandgap only ranges from -15° to 15° of incidence angle as shown in Fig. 3.21(c) for the MSFVWs in the 1-D MCs.

The approach based on Walker's equation has thus again demonstrated its capability for fast calculation and design of the desired band structure through a joint setting of the bias magnetic field H_0 and the periodic geometric parameters, e.g. d_2. Its correctness was thereafter verified experimentally.

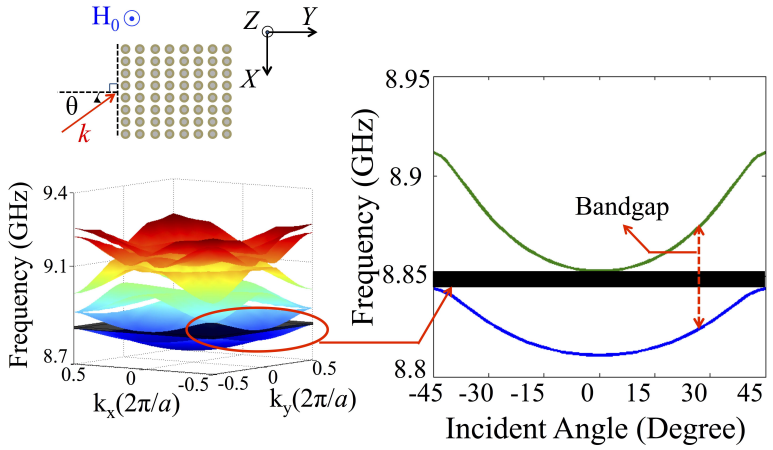

(a)

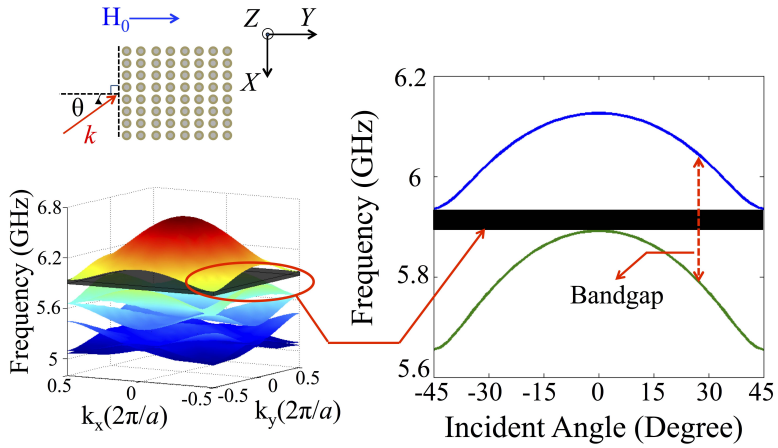

(b)

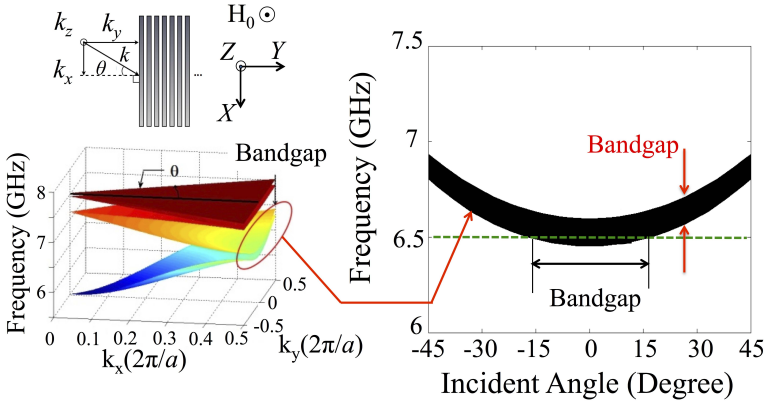

(c)

Figure 3.21: Calculated bandgaps versus the incidence angle of the MSVWs: (a) For the MSFVWs in a 2-D MC. Dark area shows that the bandgap exists at all incidence angles; (b) For the MSBVWs in a 2-D MC. Dark area shows that the bandgap exists at all incidence angles; and (c) For the MSFVWs in a 1-D MC. The dark area shows a limited range of incidence angle.

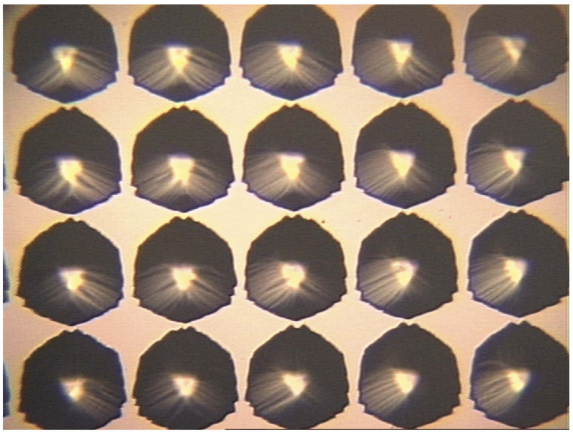

(a)

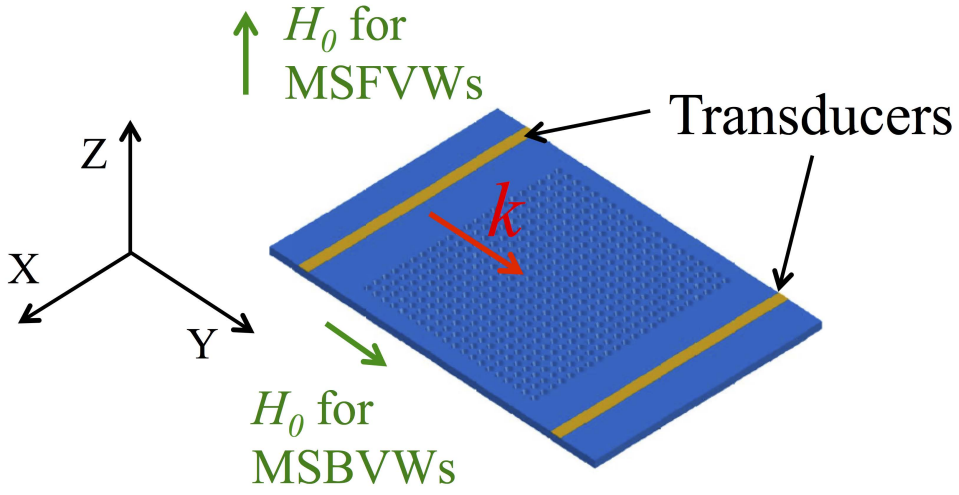

(b)

Figure 3.22: The optical image of the 2-D MC sample with square lattice (a) and the setup for experiments (b).

3.5.2 MSFVWs in a 2-D MC

Experiments were conducted to verify the calculated bandgaps of the MSVWs propagating in the 2-D MCs. Again, the samples were prepared by photolithography and wet-etching techniques on a 100μm YIG/GGG thin film sample as shown in Fig. 3.22(a). The 2-D periodic etched holes of square lattice has the dimensions of $a = 200$ μm, $R = 0.32a$, $d_1 = 100$ μm, and $d_2 = 52$

Table 3.6: Comparison of mid-gap frequency and bandgap width at Γ-X and M-Γ between experimental results and calculated results for MSFVWs.

	Mid-gap Freq./Bandgap width(GHz)		
H_0(Oe)	3000	3125	3250
Experimetal	A: 8.50/0.022	B: 8.88/0.020	C: 9.28/0.025
Calculated	A':8.49/0.009	B':8.85/0.011	C': 9.28/0.009

μm with reference to Fig. 3.19(a) and Fig. 3.19(b). Note that the hexagonal shape of the etched holes was due to preferential etching. The MSVWs were excited and received by a pair of 50 copper microstrip transmission lines as shown in Fig. 3.22(b).

Firstly, the MSFVWs were excited by applying a bias magnetic field H_0 in the direction perpendicular to both the wave propagation direction and the sample plane, namely, the Z-axis. Measurements of the insertion losses were carried out to determine the bandgaps of the MSFVWs at H_0 of 3,000, 3,125, and 3,250 Oe. As shown in Fig. 3.23, the corresponding bandgaps A, B, and C of 8.50, 8.88, and 9.28 GHz, respectively, are clearly seen. These measured values are in a very good agreement with the calculated results designated in the colored areas A', B', and C' in Fig. 3.24 with the mid-gap frequencies of 8.49, 8.85, and 9.28 GHz, respectively. A comparison between the experimental results and the calculated bandgaps at the three values of H_0 are shown in Table 3.6, and it shows a very good agreement.

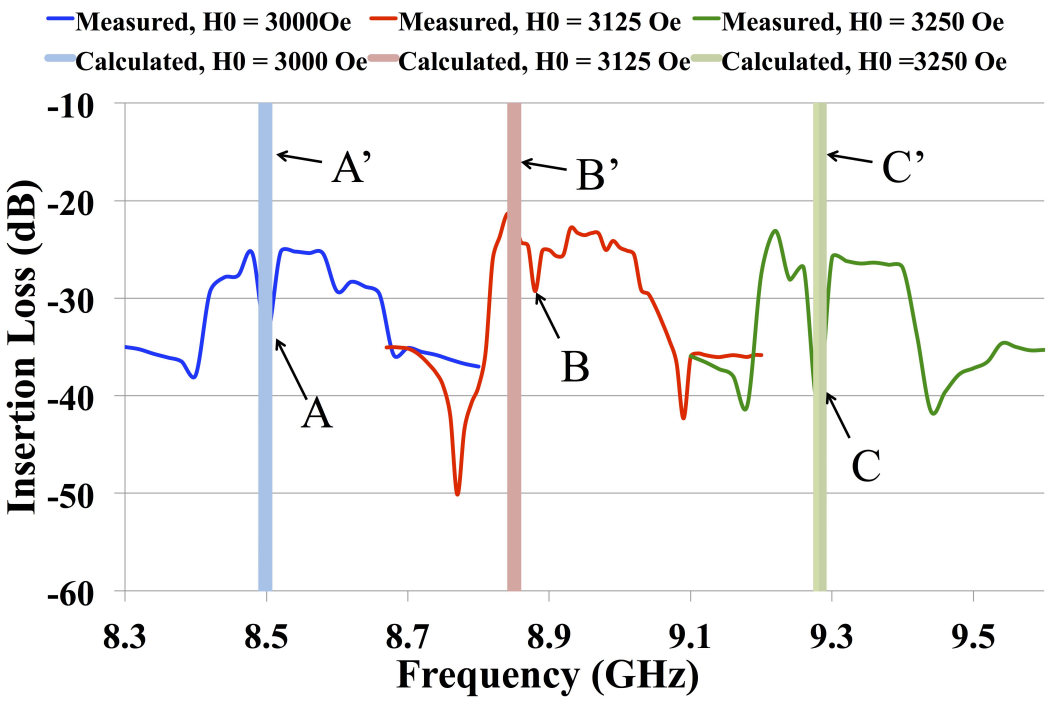

Figure 3.23: Comparison between experimental results and calculated results of MSFVWs at three H_0: 3,000, 3,125, and 3,250 Oe. The passband and bandgaps could be adjusted by tuning the H_0.

3.5.3 MSBVWs in a 2-D MC

Subsequently, the MSBVWs were excited by applying H_0 in parallel direction to the propagation direction as shown in Fig. 3.22(b). Fig. 3.25 shows the measured bandgaps A, B, and C at H_0 = 1,160, 1,375, and 1,600 Oe, respectively. As shown in Fig. 3.26, the calculated bandgaps marked A', B' and C' with the corresponding mid-gap frequencies of 5.61, 6.25, and 6.91 GHz, respectively, are in a very good agreement with the measured values. Table 3.7 lists both the measured and calculated bandgaps and bandgap widths at the three values of H_0. Clearly, the tunibility of the pass and stop bands by the bias magnetic field has been demonstrated.

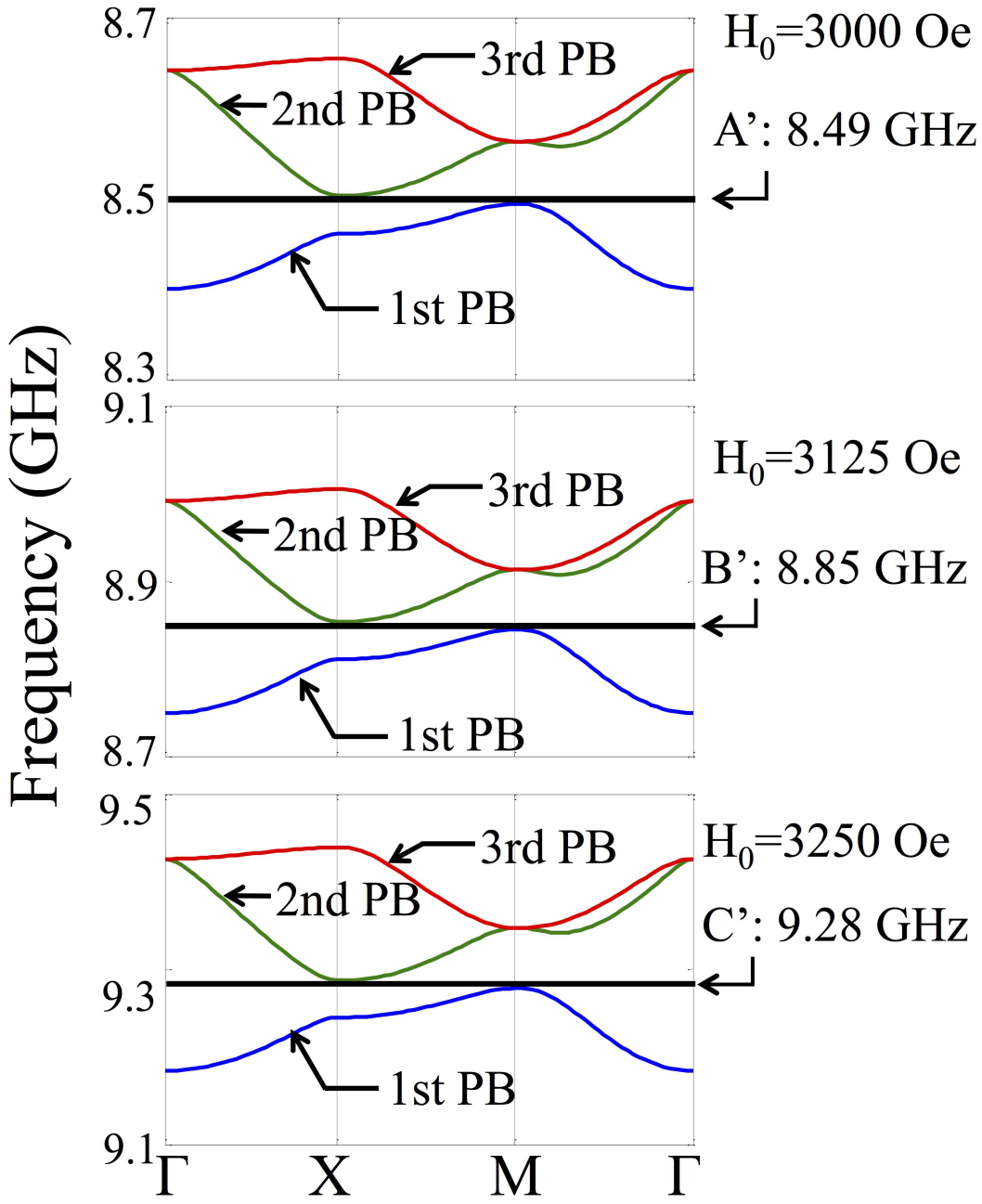

Figure 3.24: Calculated band structures of the MSFVWs at three H_0: 3,000, 3,125, and 3,250 Oe.

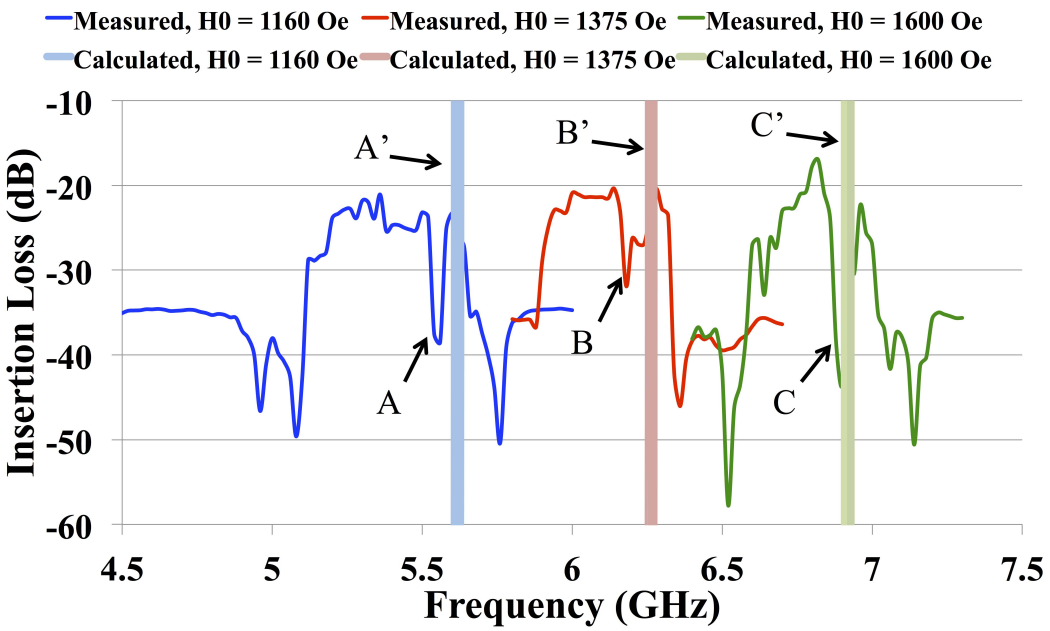

Figure 3.25: Comparison between measured and calculated results of the MSBVWs at three values of H_0: 1,160, 1,375, and 1,600 Oe. The passband and bandgaps were tuned by varying the H_0.

Experiments were also carried out to measure the angular dependence of the bandgap associated with the 2-D MCs. The variation of incidence angles of the MSBVWs was facilitated by rotating the 2-D MC sample around the Z-axis as depicted in Fig. 3.27.

As shown in Fig. 3.28, the bandgaps A, B, C, and D are clearly seen in the measured insertion losses of the MSBVWs propagating in the 2-D MC sample at the incidence angle of 0°, 10°, 20°, and 30°, respectively, at H_0 = 1,600 Oe. Table 3.8 shows the mid-gap frequency of each bandgap and a high degree of consistency across different incidence angles was observed. In other words, the bandgap of MSBVWs in the 2-D MCs at a given frequency exists in a much larger range of incidence angle than in the 1-D MCs [9, 10],.

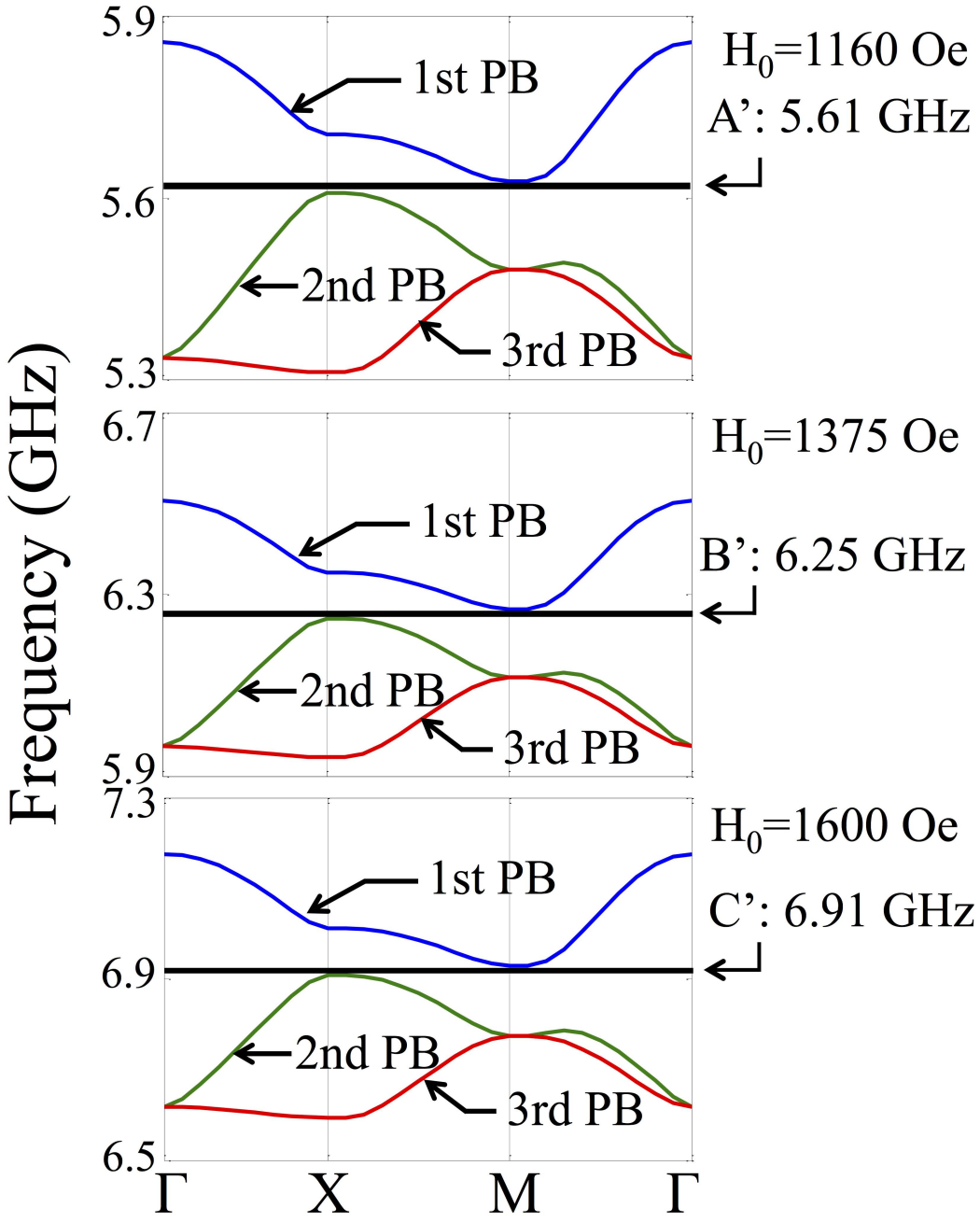

Figure 3.26: Calculated band structures for MSBVWs at three values of H_0: 1,160, 1,375, and 1,600 Oe.

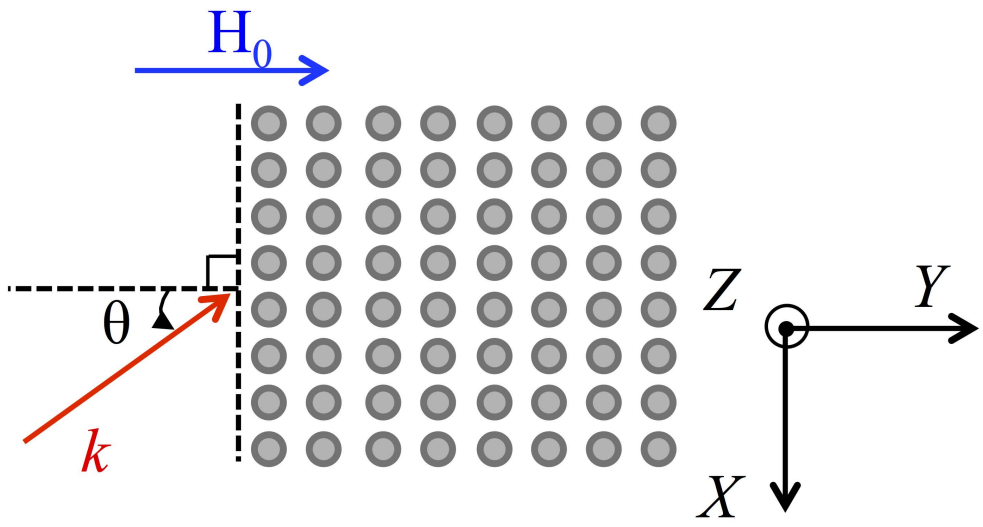

Figure 3.27: Relative direction of incident MSBVWs and the 2-D MC. The incidence angle of the MSBVWs (θ) was varied by rotating the sample around the Z-axis.

Table 3.7: Comparison of Mid-gap frequency and bandgap width at Γ-X and M-Γ between experimental results and calculated results for MSFVWs.

	Mid-gap Freq./Bandgap width(GHz)		
H_0(Oe)	1,160	1,375	1,600
Experimetal	A: 5.55/0.035	B: 6.19/0.020	C: 6.89/0.040
Calculated	A':5.61/0.025	B':6.25/0.021	C': 6.91/0.031

Table 3.8: Mid-gap Frequencies of the Bandgaps of MSBVWs versus the Incidence Angle

	Mid-gap Frequency (GHz)			
Incident Angle	θ=0°	θ=10°	θ=20°	θ=30°
Experimental	A: 6.90	B: 6.90	C: 6.92	D:6.88

In conclusion, the analytical approach based on Walker's equation was employed to study the propagation characteristics versus the bias magnetic field for both types of the MSVWs in 2-D MCs made of periodic thickness variation of square lattice in an YIG layer. Experiments were conducted to verify the calculated results, and very good agreements between the measured and calculated results were obtained.

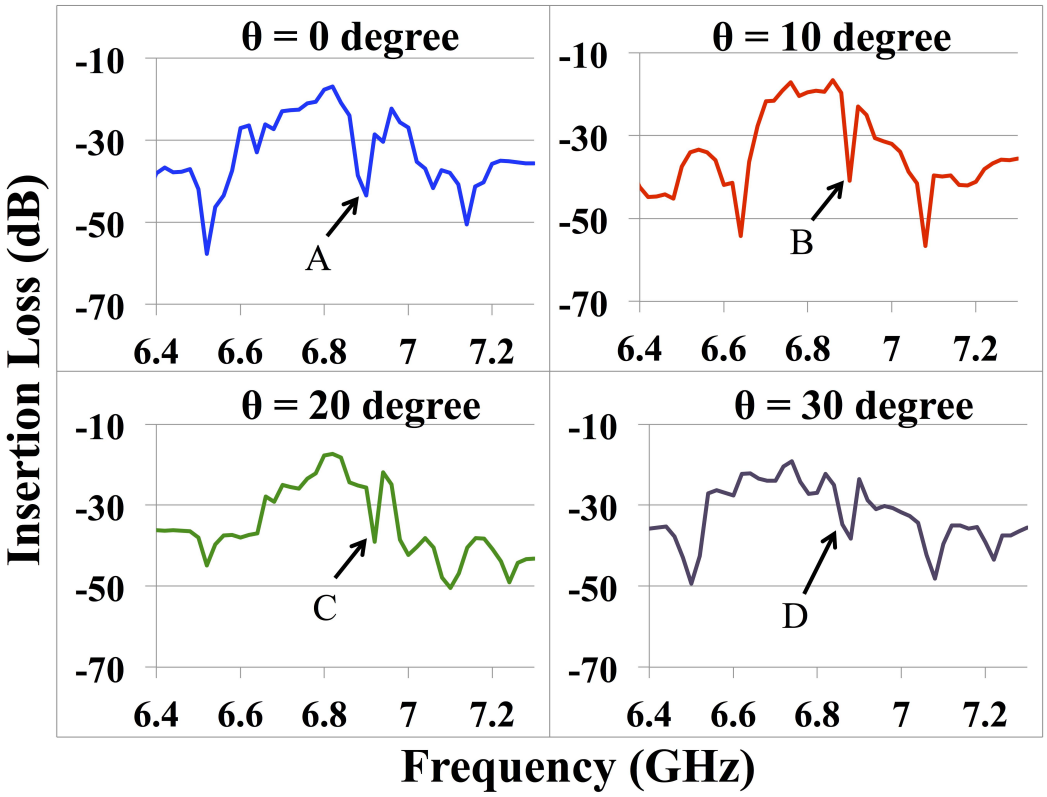

Figure 3.28: Insertion loss measurement of MSBVWs in the 2-D MC sample at the incidence angles of 0°, 10°, 20°, and 30°, and H_0=1,600 Oe.

3.6 Absorption Level Calculation in Bandgaps

As mentioned previously in section 3.1, the theoretical approach was developed to calculate complex wave numbers with given frequencies. As known, the imaginary parts of the wave numbers indicate the absorption levels of bandgaps of the MSVWs propagating in the MCs. The calculation of absorption level in 1-D MCs was reported in Ref. [29] while the calculation of absorption level in 2-D MCs has not been reported heretofore. Prof. Tsai's group is the first in developing this approach. The absorption level is calculated by utilizing the imaginary part of wave numbers obtained from Eq. 3.10 and convert to decibel unit as follow for comparison.

$$IL = 20\log(\exp(Im[k] \times l_{eff})) \tag{3.19}$$

where Im[k] is the imaginary part of the complex wave number and l_{eff} is the effective length of the 2-D MCs, which is 0.4cm in this case. As shown in Fig. 3.29, the calculated bandgap is between 8.524 and 8.557GHz and the maximum absorption level is -14.2dB as the red line shows. A close agreement with the experimental results is clearly seen from Fig. 3.29.

Note that the experimental result in Fig. 3.29 is normalized by subtracting the IL of MSFVWs in 2-D MCs by the IL in non-structured YIG thin film

as shown in Fig. 3.30. The measured bandgap is between 8.533 and 8.576 GHz, and the maximum absorption level is -12.18dB. The measurements were conducted with the setup shown in Fig. 3.22(b) with the same 2-D MCs sample used in section 3.5.

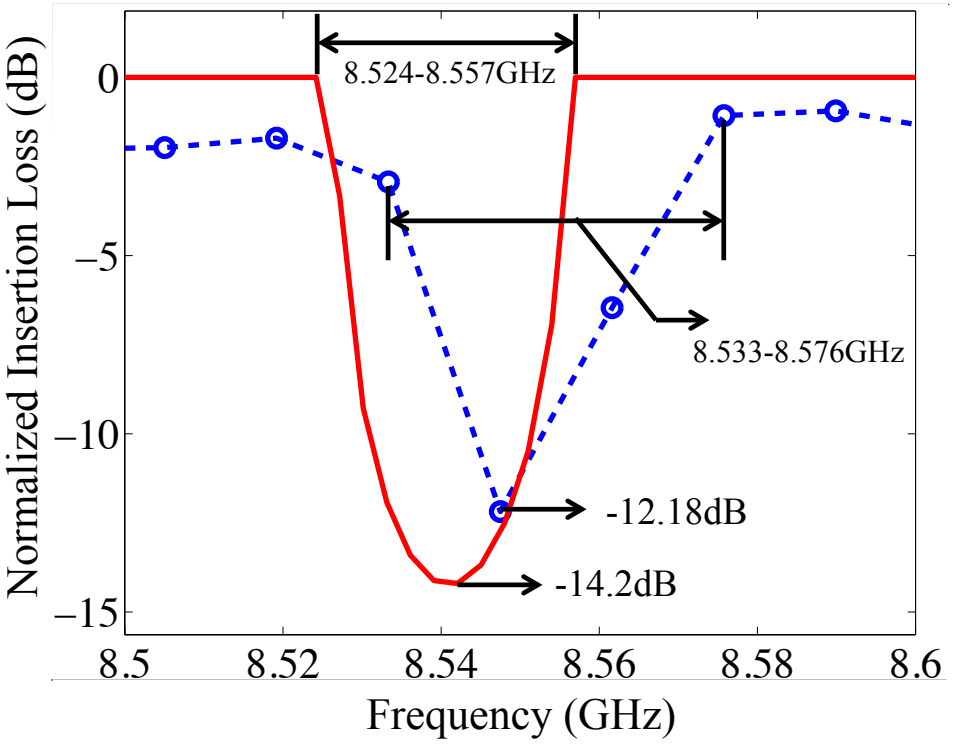

Figure 3.29: The comparison of absorption level in the theoretical and experimental results at the bandgap.

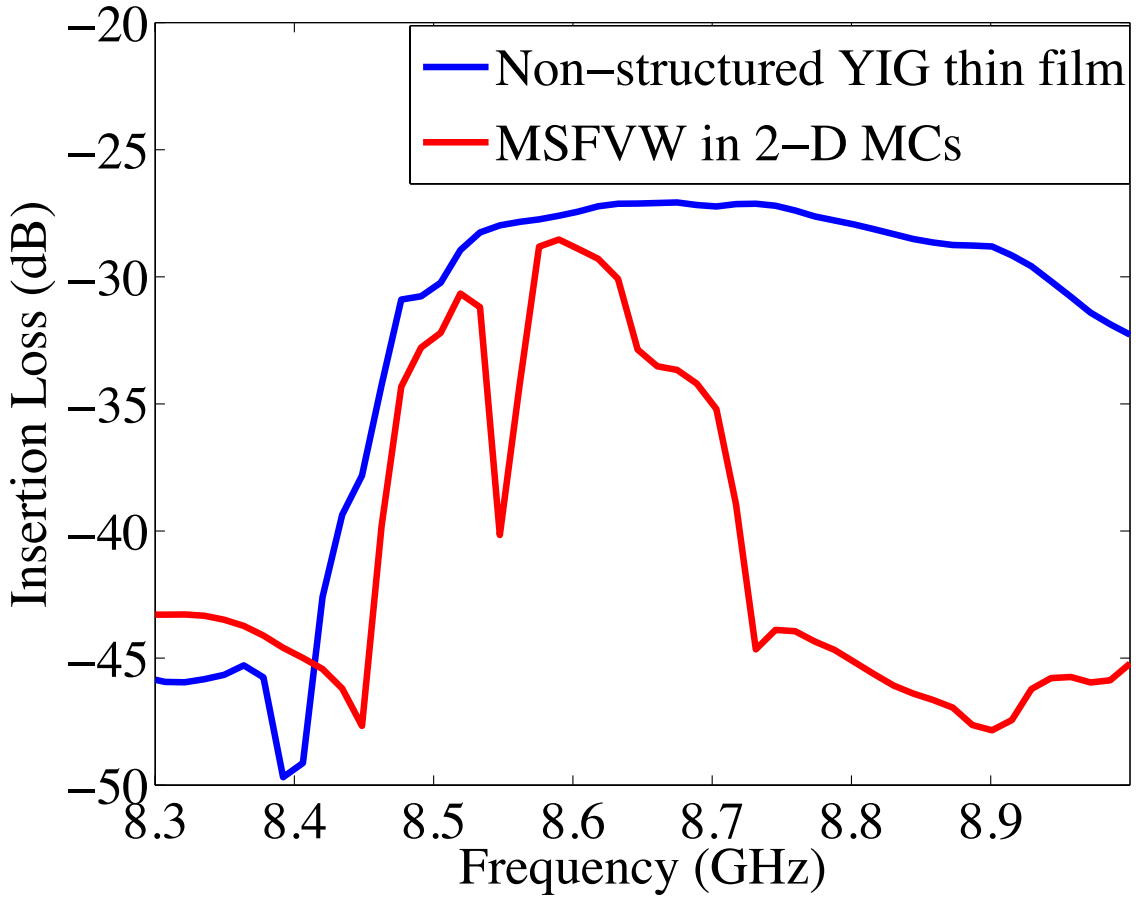

Figure 3.30: The experimental results of MSFVWs in a non-structured YIG thin film and 2-D MCs with bias magnetic filed H_0 3010 Oe. Blue line is the MSFVWs in a non-structured YIG thin film and red line is the MSFVWs in 2-D MCs.

Chapter 4

Magnonic Crystal-Based Tunable Microwave Devices

In this chapter the applications of 1-D and 2-D MCs for realization of magnetically tunable wideband microwave filters and phase shifters are presented.

4.1 MC-Based Tunable Microwave Filter

By applying a bias magnetic field (H_0) of 1,200 Oe on the 1-D MC as shown in Fig. 4.1, the MSBVW excited is seen to function as a band-pass filter (BPF) as shown in Fig. 4.2(a)(in black). Furthermore, the bandgap arising from the periodic structure of the MC facilitates filtering function of a band-stop filter (BSF) at a center frequency of 4.95 GHz with a 3 dB BW of 100 MHz. By slightly decreasing the bias magnetic field from 1,200 Oe to 1,180 Oe or

slightly increasing the field from 1,200 Oe to 1,250 Oe, the center frequency of the BSF was tuned to 4.875 GHz and 5.05 GHz, respectively, as shown in Fig. 4.2(a). Similar results were also obtained in the 2-D MC. Specifically, by setting the bias magnetic field at 1,265 Oe, a BSF embedded in a BPF with a center frequency of 4.90 GHz and a 3 dB BW of 90 MHz was measured as shown in Fig. 4.2(b), a small variation of the fields by ± 15 Oe centered at 1,265 Oe, the BSF's center frequencies were tuned to 4.9 and 4.975 GHz, respectively, with the corresponding 3 dB BW remained at 90 MHz.

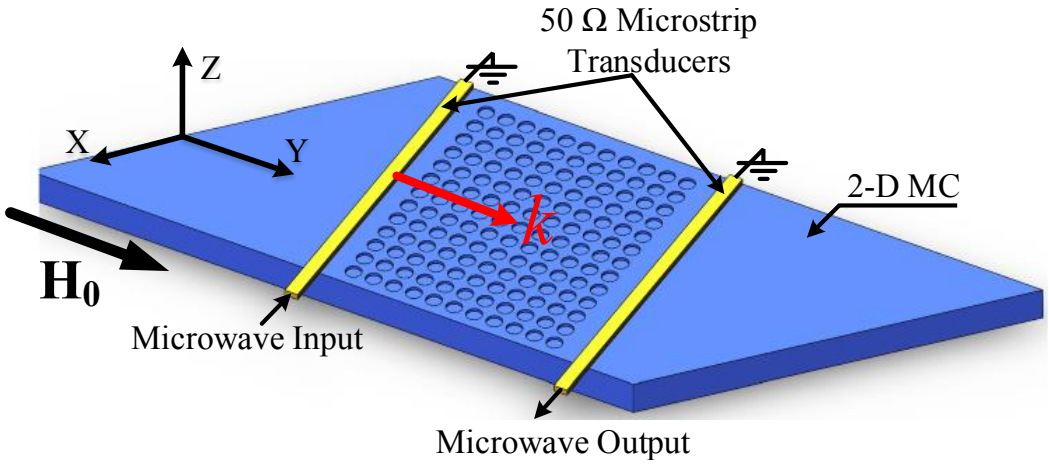

Figure 4.1: The arrangement for excitation and measurement of the MSBVWs in the 1-D and 2-D MCs

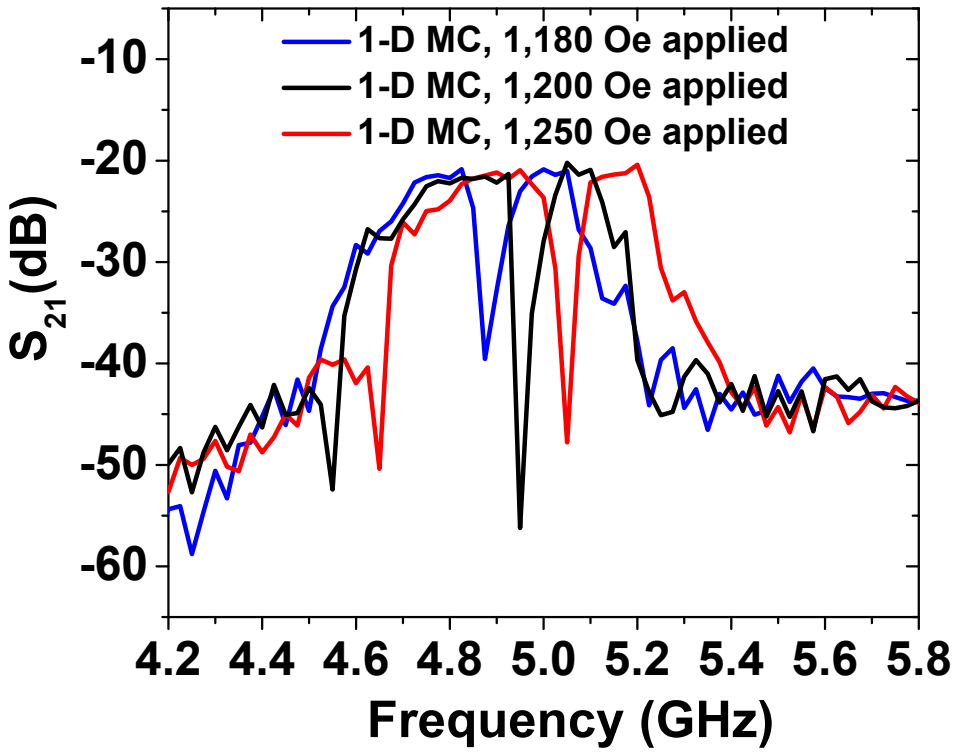

(a)

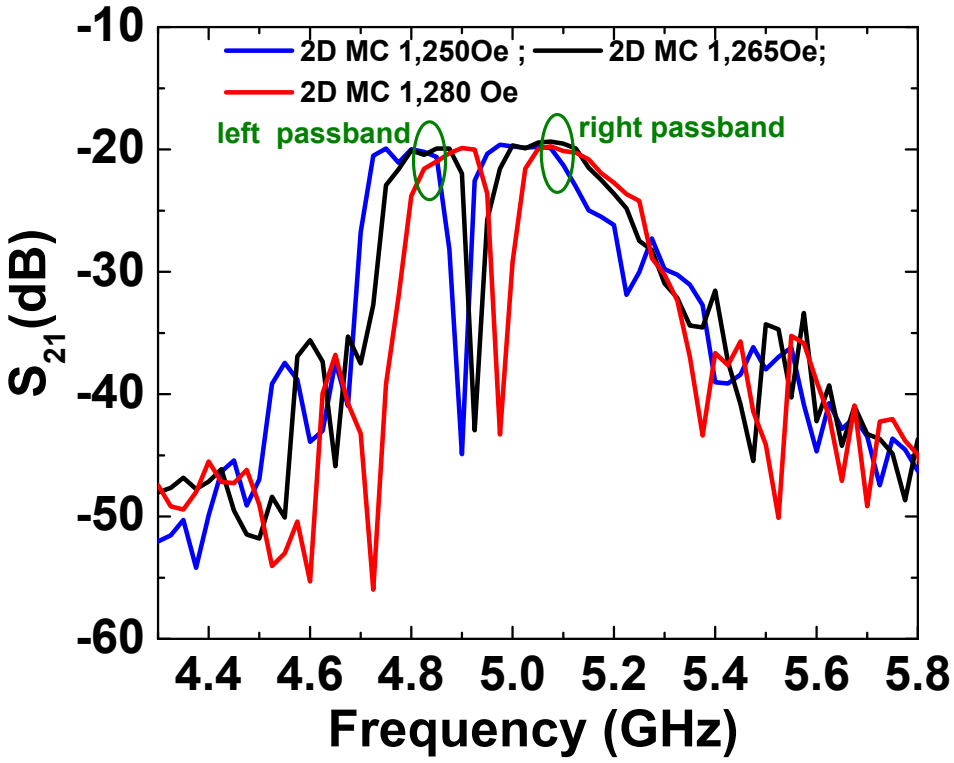

(b)

Figure 4.2: Excitation of MSBVWs to function as a tunable BPF with a BSF embedded in (a) 1-D MC with 1,180, 1,200 and 1,250 Oe applied, and (b) 2-D MC with 1,250 Oe, 1,265 Oe and 1,280 Oe applied, respectively.

4.2 MC-Based Tunable Phase Shifters

Tunable microwave phase shifters that utilize the tunable phase characteristics of the MSBVWs in YIG/GGG thin film-based 1-D and 2-D MCs on a delay line structure were first reported by Prof. Chen S. Tsai's group in Ref. [58]. The theoretical approach based on Walker's equation mentioned previously in section 3.1, namely Eq. 3.4 and Eq. 3.6, was employed to calculate the phase shifts of MSBVWs in the 1-D and 2-D MCs with the bias magnetic field as a parameter. The geometrical profiles of the 1-D and 2-D MCs used in the numerical calculation are shown in Figs. 4.3 (a)-(d).

For the configuration with the MSBVWs propagating along the Y-direction as shown in Fig. 4.1, we have $k_x = 0$, and Eq. 3.6 is rearranged into the following form:

$$(\mathbf{M}' - \mathbf{K}')\,\Psi = 0, \tag{4.1}$$

where

$$\mathbf{M}' = \left(\omega^2 - H_0^2\right)^{-1}\left[\left(4\pi M_s H_0 + H_0^2\right)\left(-k_z^2\right) + k_z^2\omega^2\right], \tag{4.2}$$

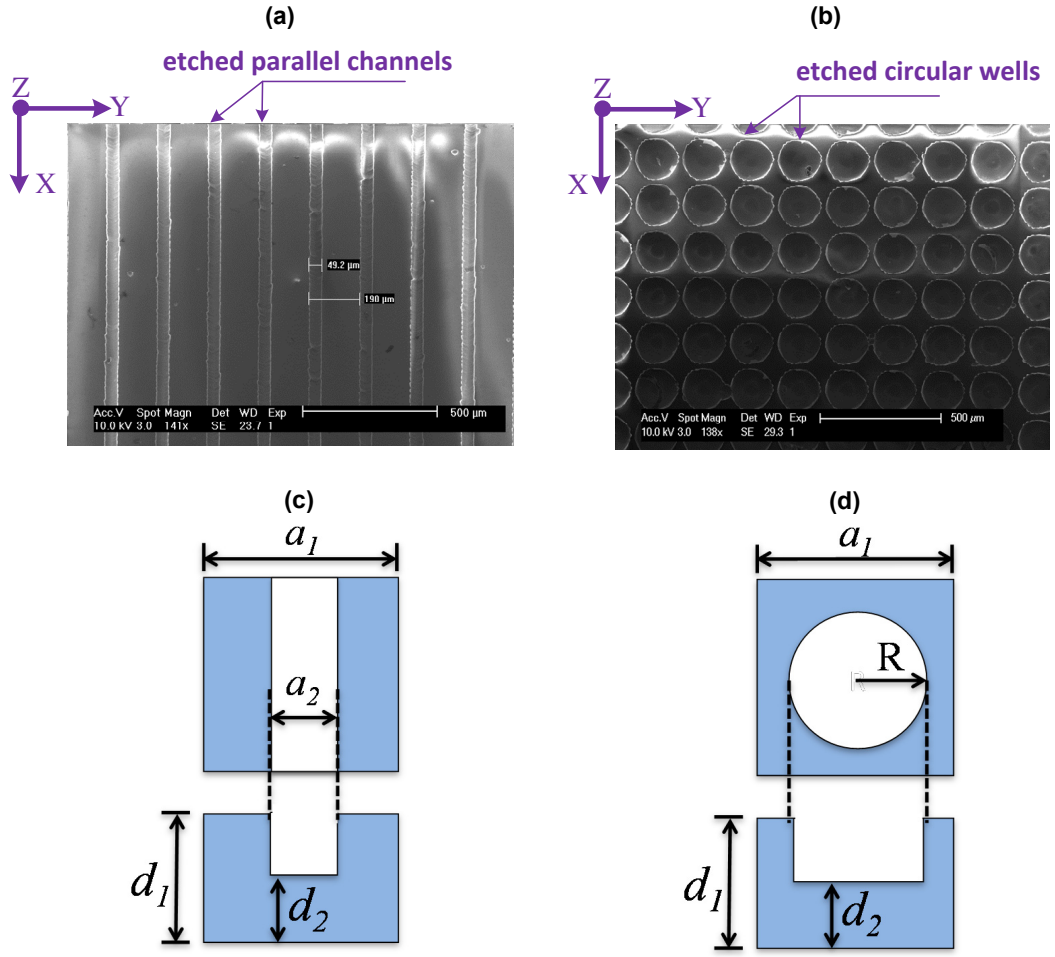

Figure 4.3: he scanning electron microscope (SEM) images of the 1-D MC with etched parallel channels (a), and the 2-D MC with etched circular wells (b). The profiles of the unit cell of 1-D MC with a_1=245 μm, a_2= 75 μm, d_1= 100 μm, and d_2= 80 μm (c), and of 2-D MC with a_1=200μm, R=64 μm, d_1= 100 μm, and d_2= 52 μm (d).

$$\mathbf{K}' \equiv -\left(k_y^2 + ik_y\frac{\partial}{\partial y}\right) + \left(\frac{\partial^2}{\partial x^2} + \frac{\partial^2}{\partial y^2}\right), \tag{4.3}$$

Now, by setting the determinant of the matrix $(\mathbf{M}' - \mathbf{K}')$ equal to zero and specifying the eigen frequency ω, $\mathbf{M}'$ in Eq. 4.2 is determined and the only unknown quantity, wave number k_y, are solved. The differential phase shift $(\triangle\phi)$ obtained by varying the bias magnetic field from H_0 to H_1 at the eigen

frequency ω_0 in the MCs is thus given by Eq. 4.4:

$$\triangle\phi|_{\omega=\omega_0} \equiv l_{eff} \times \Big[(k_y)_{H_1} - (k_y)_{H_0}\Big]_{\omega=\omega_0}, \tag{4.4}$$

where l_{eff} is the effective length of the microwave transducers structure (4 mm in this study) used to excite and receive the MSBVWs. Figs. 4.4(a) and (b) are the calculated phase shifts (ϕ) in the 1-D and 2-D MCs obtained utilizing the theoretical approach presented above. Specifically, the calculated $\triangle\phi$ at 4.82 GHz in the 1-D MC are 169.2°/cm (or 67.7° in total) as H_0 was tuned from 1,185 to 1,200 Oe and 643.2°/cm (or 257.3° in total) as H_0 was tuned from 1,200 to 1,250 Oe. Similarly, the calculated $\triangle\phi$ at 4.82 GHz in the 2-D MC are 459.4°/cm (or 183.8° in total) as H_0 was tuned from 1,245 to 1,265 Oe and 726.7°/cm (or 290.7° in total) as H_0 was tuned from 1,265 to 1,290 Oe.

The MSBVWs were excited and received by mounting the MC samples upon a pair of 50 Ω microwave transducers with 4 mm separation fabricated upon the RT/Duroid 6010 substrate as shown in Fig. 4.1. The insertion loss (S_{21})and the unwrapped phase of the MSBVWs in the 1-D and 2-D MCs were measured by using Vector Network Analyzer (HP-8510C) at a step size of 6.25 MHz.

Fig. 4.5(a) shows the measured S_{21} in the 1-D MC at the bias field H_0 of 1,185, 1,200 and 1,250 Oe, depicting tuning of the bandgaps from A to B and

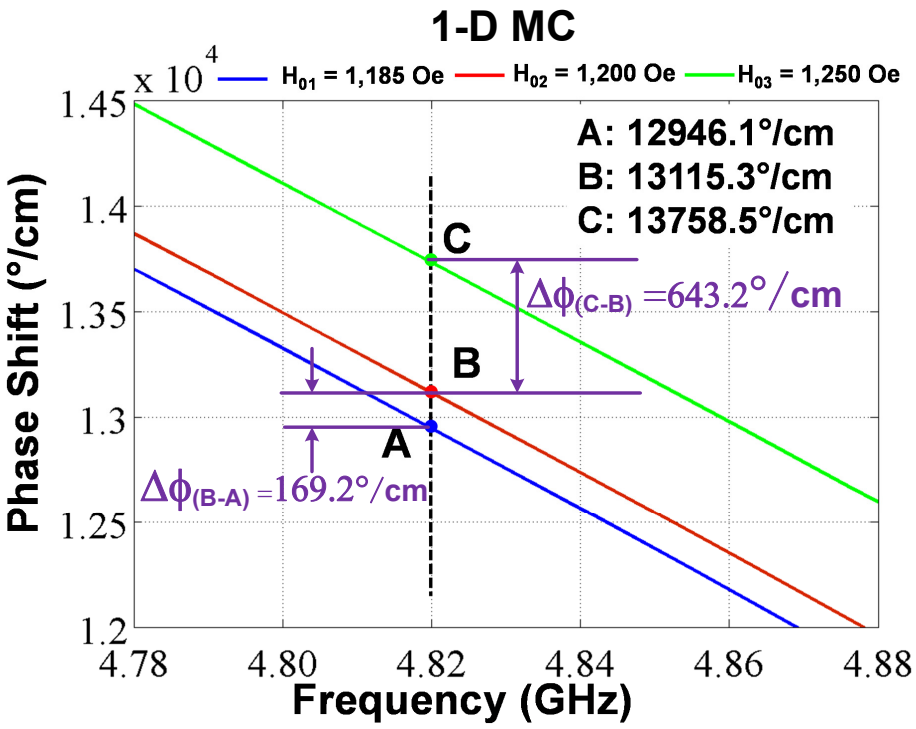

(a)

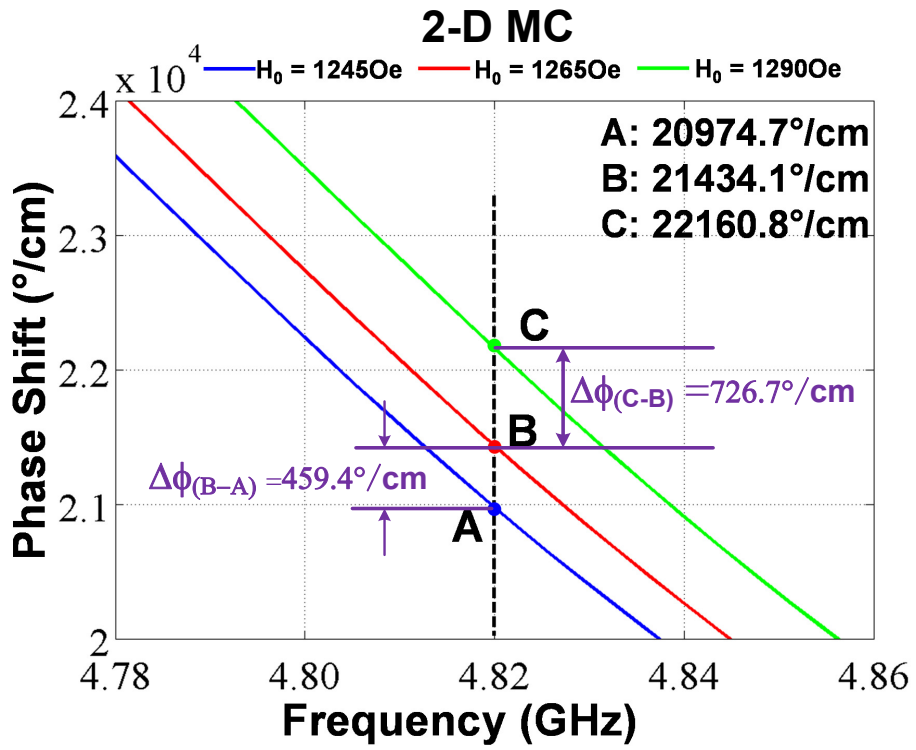

(b)

Figure 4.4: The calculated phase shifts in the 1-D MC at H_0 of 1,185, 1,200 and 1,250 Oe (a), and in the 2-D MC at H_0 of 1,245, 12,65 and 1,290 Oe (b).

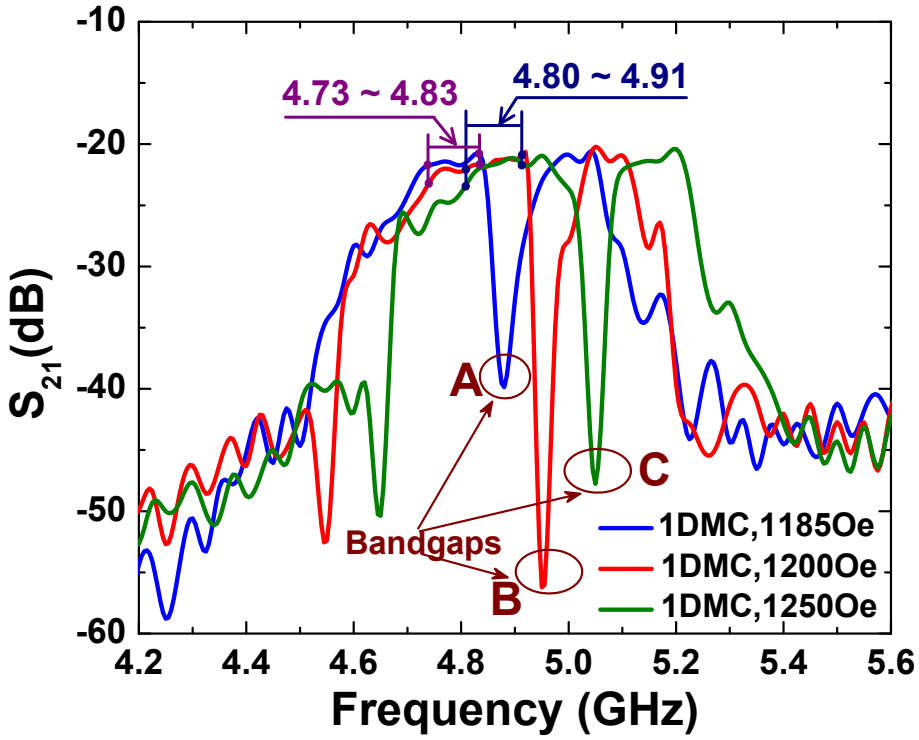

(a)

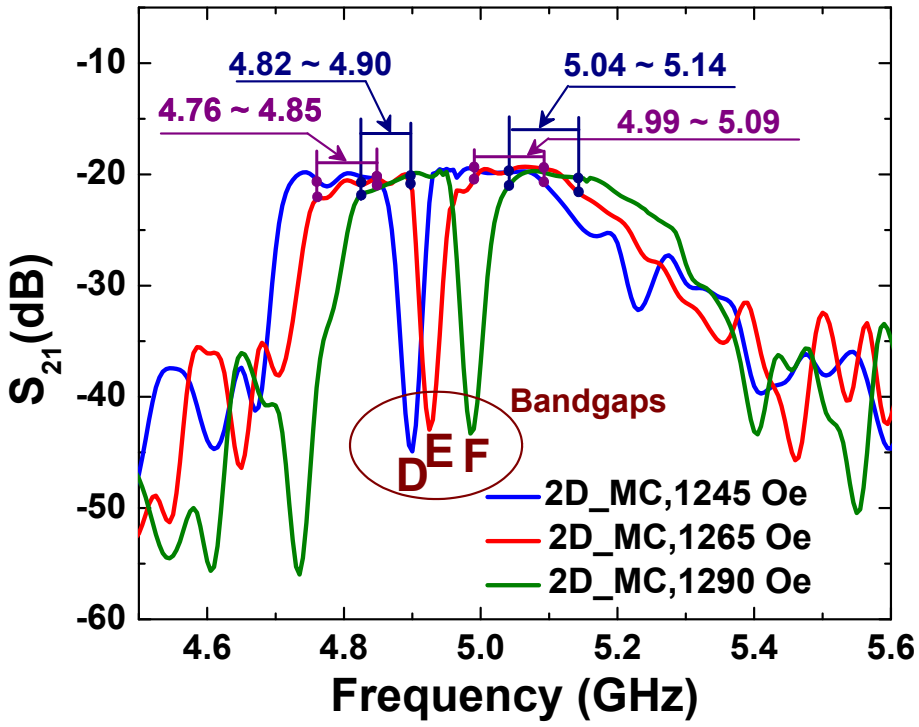

(b)

Figure 4.5: The measured S_{21}(dB) at H_0 of 1,185, 1,200 , and 1,250 Oe of the 1-D MC (a), and of the 2-D MC (b) at H_0 of 1,245, 1,265, and 1,290 Oe.

to C. When H_0 was tuned from 1,185 to 1,200 Oe, the $\triangle\phi$ was measured in the *left* passband from 4.73 to 4.83 GHz of the bandgap where the insertion loss variation ($\triangle S_{21}$) was relatively small. As shown in Fig. 4.6(a), an average differential phase shift ($\triangle\phi_{avg}$) of 80.9° and an average insertion loss variation $(\triangle S_{21})_{avg}$ of 2.08 dB/cm were measured. Further increase in the bias field by 50 Oe to 1,250 Oe produced a $\triangle\phi_{avg}$ as large as 259.3° and a $(\triangle S_{21})_{avg}$ as low as 0.78 dB/cm for the frequency range from 4.80 to 4.91 GHz as shown in Fig. 4.6(b). The corresponding phase tuning rates are 13.48°/(Oe-cm) and 12.97°/(Oe-cm), respectively.

Similarly, Fig. 4.5(b) shows the measured S_{21} in the 2-D MC at H_0 of 1,245, 1,265, and 1,290 Oe as well as the frequency ranges in which the phase shifts were measured. Specifically, as shown in Fig. 4.6(c), by biasing the 2-D MC at 1,265 Oe and lowering the bias field by 20 Oe to 1,245 Oe, a $\triangle\phi_{avg}$ of 198.4° and a $(\triangle S_{21})_{avg}$ of 1.85 dB/cm were measured from 4.76 to 4.85 GHz in the left passband of the bandgap D. By increasing H_0 further by 25 Oe to 1,290 Oe, a $\triangle\phi_{avg}$ of 255.4° and a $(\triangle S_{21})_{avg}$ of 1.49 dB/cm were obtained in the frequency range from 4.82 to 4.90 GHz. The corresponding phase tuning rates are 24.8 and 25.54 °/(Oe-cm), respectively. The measured $\triangle\phi_{avg}$ and $(\triangle S_{21})_{avg}$ in the *right* passband of the bandgap E is shown in Fig. 4.6(d). It shows the $\triangle\phi_{avg}$ and $(\triangle S_{21})_{avg}$ values of 207.2° and 0.97 dB/cm, respectively, from 4.99 to 5.09 GHz when tuning H_0 from 1,245 to 1,265 Oe. Further tuning of H_0 to 1,290 Oe resulted in a $\triangle\phi_{avg}$ of 258.3° together with a $(\triangle S_{21})_{avg}$ of

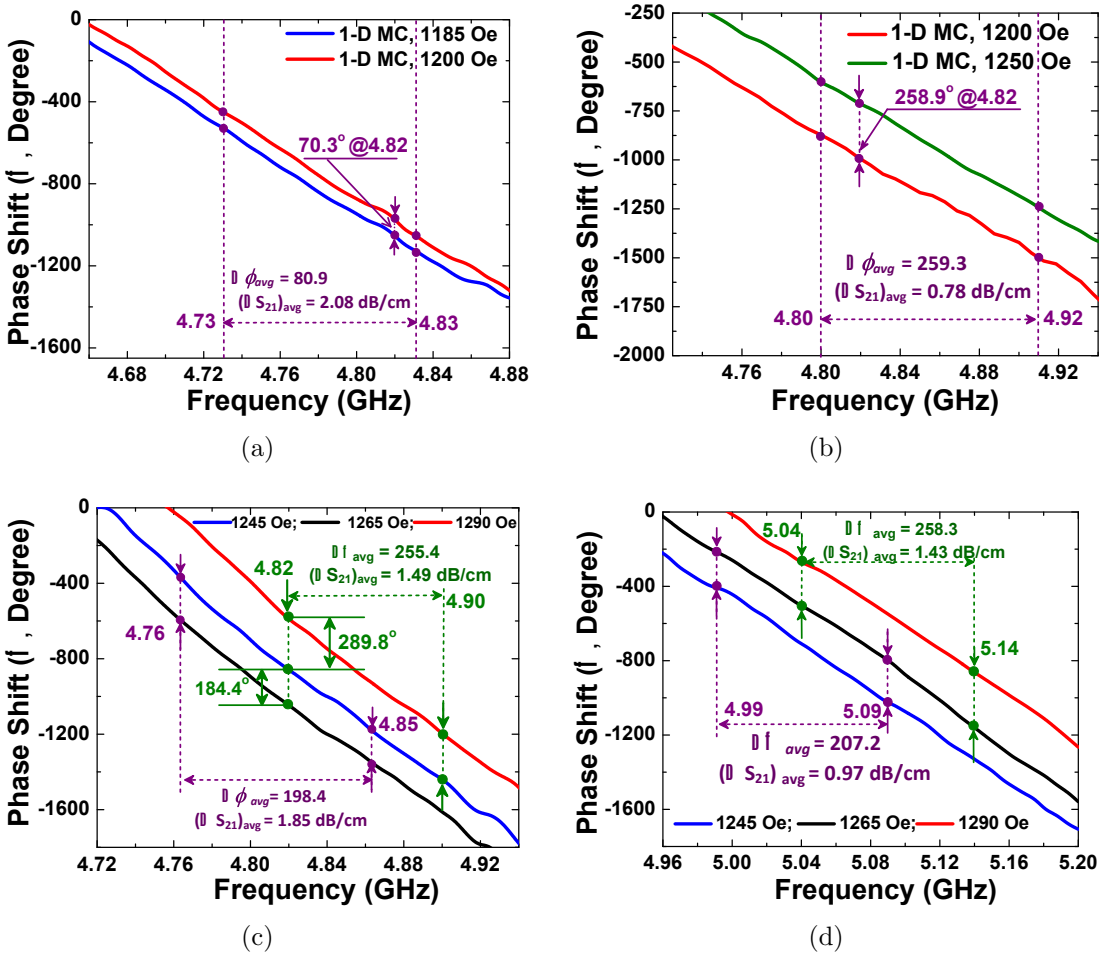

Figure 4.6: The measured phase shifts of the 1-D MC:(a) at H_0 of 1,185 and 1,200 Oe, (b) at H_0 of 1,200 and 1,250 Oe in the left passband; and of the 2-D MC: (c) left passband, and (d) right passband at H_0 of 1,245, 1,265 and 1,290 Oe.

1.43 dB/cm from 5.04 to 5.14 GHz in the right passband of the bandgap F. The corresponding phase tuning rates are 25.9 °/(Oe-cm) and 25.83°/(Oe-cm), respectively.

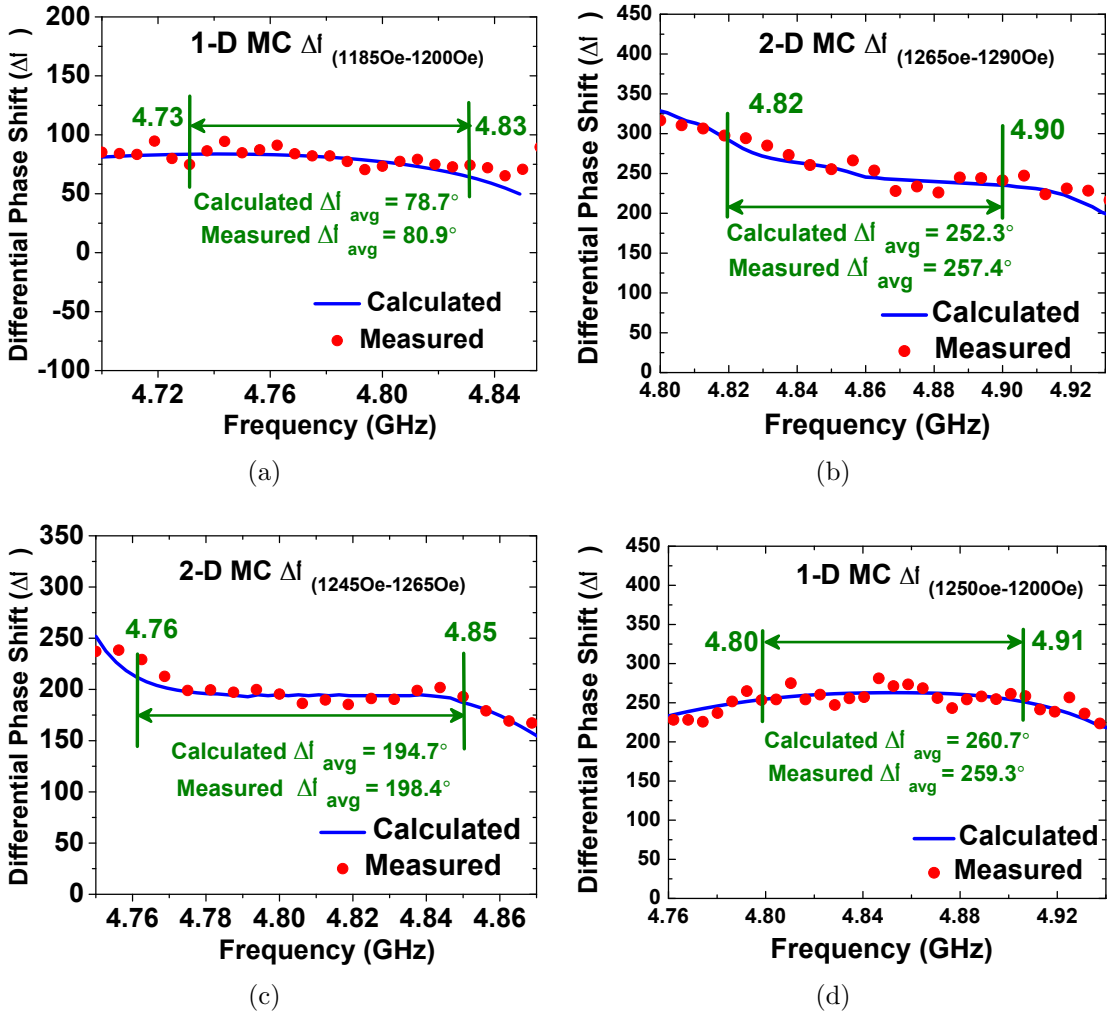

Figure 4.7: Comparison between the calculated and measured $\triangle\phi_{avg}$ in the 1-D MC: (a) from 1,185 to 1,200 Oe and (b) from 1,200 to 1,250 Oe; and in the 2-D MC: (c) from 1,245 to 1,265 Oe , and (d) from 1,265 to 1,290 Oe.

The measured and calculated $\triangle\phi_{avg}$ for the 1-D MC are shown in Figs. 4.7(a) and (b). Specifically, 80.9° versus 78.7° from 4.73 to 4.83 GHz was obtained by tuning H_0 from 1,185 to 1,200 Oe. Further increase of H_0 by 50 Oe to 1,250

Oe resulted in much larger measured $\triangle\phi_{avg}$ of 259.3° verus the calculated value of 260.7° from 4.80 to 4.91 GHz.

Similarly, the experimental results for the left passband of the 2-D MC in comparison to the calculated $\triangle\phi_{avg}$ are shown in Figs. 4.7 (c) and (d). The measured and calculated $\triangle\phi_{avg}$ from 4.76 to 4.85 GHz are 194.7° and 198.4°, respectively, by tuning H_0 from 1,245 to 1,265 Oe, while the corresponding $\triangle\phi_{avg}$ are 252.3° and 257.4° when tuning H_0 from 1,265 to 1,290 Oe in the frequency range from 4.82 to 4.90 GHz.

In short, the $\triangle\phi_{avg}$ obtained in the left passband of the 1-D MC together with that obtained in both left and right passbands of the 2-D MC are summarized in Table 4.2 and Table 4.2, showing an excellent agreement between the experimental and calculated results.

Table 4.1: Comparison of $\triangle\phi_{avg}$(°)/phase tuning rate (°/Oe-cm) between measured and calculated results in the case of 1-D MCs.

MC Type	1-D MC	
Location	Left Passband	
H_0(Oe)	1185-1200	1200-1250
Freq (GHz)	4.73-4.83	4.80-4.91
Calc(°/(°/Oe-cm))	78.7/13.12	260.7/13.1
Meas (°/(°/Oe-cm))	80.9/13.48	259.3/12.97

Table 4.2: Comparison of $\triangle\phi_{avg}$(°)/phase tuning rate (°/Oe-cm) between measured and calculated results in the case of 2-D MCs.

MC Type	2-D MC			
Location	Left Passband		Right Passband	
H_0(Oe)	1245-1265	1265-1290	1245-1265	1265-1290
Freq (GHz)	4.76-4.85	4.82-4.90	4.99-5.09	5.04-5.14
Calc(°/(°/Oe-cm))	194.7/24.3	252.3/25.23	204.1/25.5	260.4/26.04
Meas (°/(°/Oe-cm))	198.4/24.8	255.4/25.54	207.2/25.9	258.3/25.83

comparing to the conventional phase shifters reported earlier [59–70] the MC-based phase shifters presented above have demonstrated simultaneously a much larger phase tuning rate in unit degree/(Oe-cm) and a significantly smaller variation in insertion loss (dB/cm). Specifically, comparing to the best non-MC-based microwave phase shifter recently reported in Ref.[27][70], the MCs-based phase shifter was better than one order of magnitude in phase tuning rate (25.9 vs. 0.32 °/(Oe-cm)), figure of merit (26.7 vs. 0.72 °/(dB-Oe)), and much shorter propagation path (4 vs. 97.1 mm). The superior performances of the MC-based phase shifter are attributable to the larger wave numbers of the MSWs/SWs in MCs and the much shorter corresponding wavelengths (in the order of $\approx 10^{-4}$ cm) than the corresponding wavelength of the propagating microwaves (in the order of $\approx 10^{-1}$ cm) in the conventional phase shifters [43]. Thus, agile phase shifts are more easily achieved with short propagation path in the MCs-based phase shifters.

4.3 MC-based MSFVWs waveguides

The defect-free MCs have been extensively studied both theoretically and experimentally and presented in previous sections. However, reports on defective MCs are much less frequent. The additional modes created by the local defects confine the waves in designated regions and are therefore essential for the devices based on periodic structures such as the PC-based optical

waveguides. A complete theoretical analysis of the confinement of magnetostatic forward volume waves (MSFVWs) in the line-defect region of 2-D MCs with periodic variation in thickness in a YIG layer and the experimental verification were presented in Ref. [71] and this section. As MSFVWs possess isotropic dispersion relation in the YIG layers, the complexity in the analysis is significantly reduced and the effect of line defects can be studied. The theoretical approach based on Walker's equation previously mentioned is employed in the analysis, namely Eq. 3.3 and 3.6.

In a defect-free 2-D MCs, the domain of calculation covers one unit cell with periodic boundary conditions as previously shown in Fig. 3.19(b). For the defective 2-D MCs the domain of calculation covers multiple unit cells in order to include the local irregularity. For example, the 2-D MCs under study is based on a 100μm thick YIG layer with the dimensions shown in Fig. (4.8). The domain of calculation covers five unit cells with a defect at the center. The grey areas are the unetched YIG layer, and the white circle represents the etched hole to create the periodic variation in thickness. The defect at the center of the domain of calculation is created by replacing the etched hole by the unetched YIG layer.

The eigen-frequencies ω and the corresponding eigenvectors Ψ calculated from Eq. (3.6) are utilized to construct the band diagrams and the mode patterns, respectively. The band diagrams are obtained from the relationship between

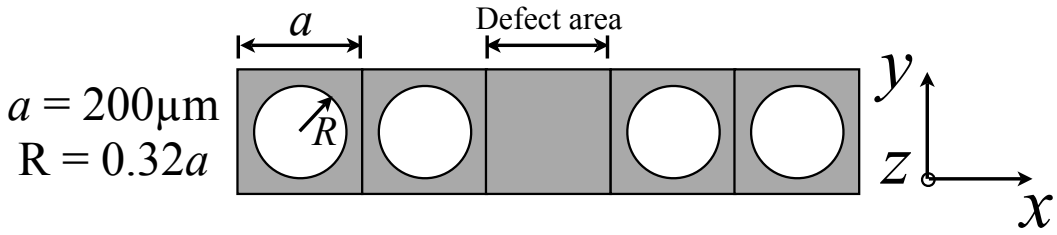

Figure 4.8: The domain of calculation of the 2-D MC with line defects. The lattice constant a is 200 μm, and the radius of the etched hole R is $0.32a$.

the wave numbers k and the eigen-frequecies ω. Each element in the eigenvector Ψ represents the magnetic potential at one point in the discrete domain of calculation and can be used to construct the mode pattern of the MSFVWs by arranging them in the domain of calculation in a correct order. Fig. (4.9) shows the calculated band diagram and selected mode patterns of the MSFVWs propagation in the defective 2-D MCs with the geometric parameters shown in Fig. (4.8). In the band diagram on the left of Fig. (4.9) the grey areas represent the pass band, meaning that the MSFVWs can propagate freely within the band. The corresponding mode pattern on the right supports this observation as it clearly shows the MSFVWs with high amplitude in the structured region. In contrast, the defect mode designated by the red line in the band diagram shows that the MSFVWs are confined within the defective region and decay as they propagate into the periodic structure. The confinement of the MSFVWs provides the basis for construction of useful devices such as waveguides.

Experiments were carried out to verify the theoretical predictions of the defect modes associated with the line defects. The periodic structures were

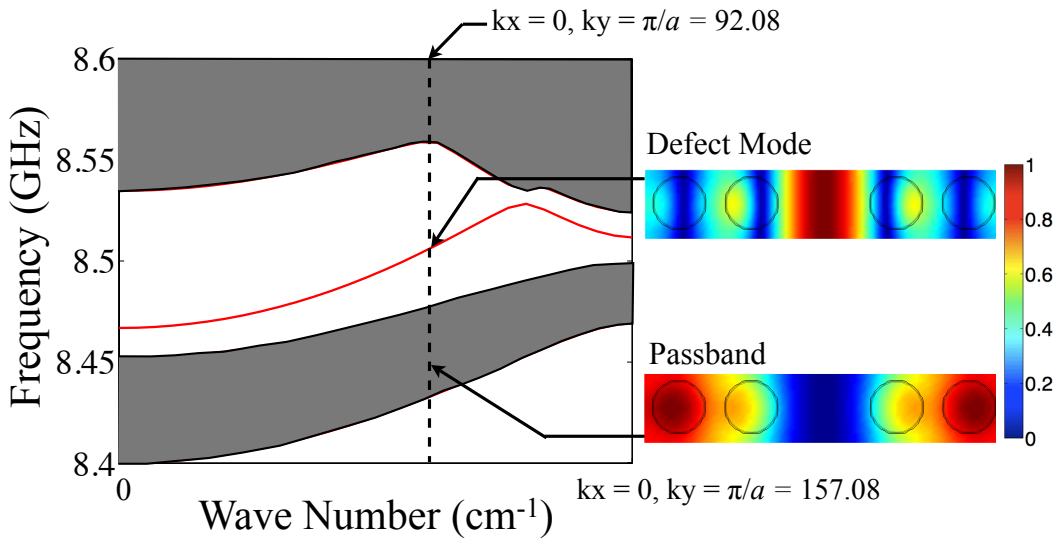

Figure 4.9: The calculated band diagram (left) and corresponding mode patterns (right) of the 2-D MCs with dimensions shown in Fig. (4.8), bias magnetic field $H_0 = 3000$ Oe, and $n = 2$. The grey areas and the red line represent the pass bands and the defect mode, respectively, in the 2-D MC.

fabricated by photolithography and subsequent wet-etching in a 100μm-thick YIG/GGG layer. The defect-free MC and the MC with line defects were prepared simultaneously to ensure a meaningful comparison as shown in Fig. 4.10(a) and Fig. 4.10(b), respectively. The 2-D MCs fabricated have the following dimensions: lattice constant $a = 200$ μm, radius of etched holes R = $0.32a$, thickness of unetched YIG layer $d_1 = 100$ μm and thickness of etched YIG layer $d_2 = 55$ μm. The bias magnetic field was applied in the direction perpendicular to the YIG layer. A pair of 50Ω microstrips were utilized to excite and receive the MSFVWs propagating in the X-Y plane of the YIG layer.

Specifically, by applying a bias magnetic field of 3000Oe, the MSFVWs were excited at the frequency range from 8.34 to 8.64GHz. Note that the cal-

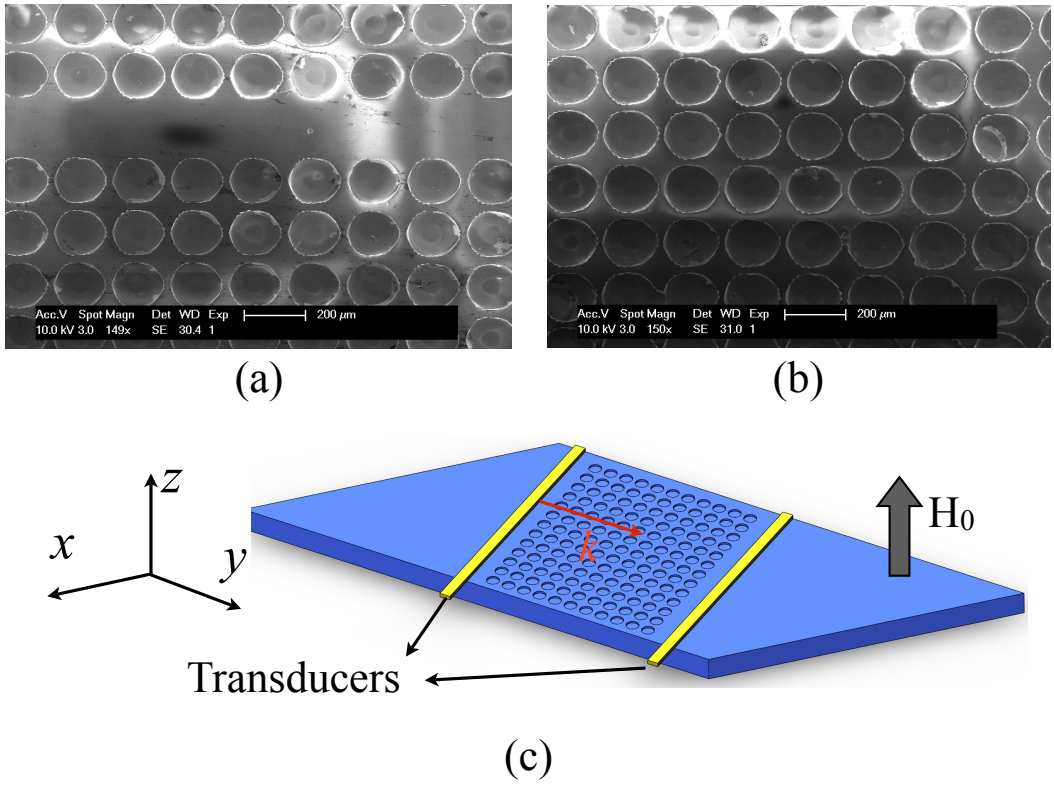

Figure 4.10: The scanning electron microscope (SEM) pictures of (a) the defect-free MC and (b) the MC with line-defects; (c) A pair of 50Ω microstrip transducers for the excitation and reception of the MSFVWs. The bias magnetic field was applied in the direction perpendicular to the YIG layer, and the MSFVWs propagated in the X-Y plane of the YIG layer.

culated bandgap of the MSFVWs in the defect-free MC using Eq. (3.6) is between 8.44 and 8.48GHz, which is in a good agreement with the measured bandgap from 8.46 to 8.50GHz as clearly shown in Fig. 4.11(a). The same good agreement was also obtained by applying a bias magnetic field of 3275Oe as Fig. 4.11(b) shows. As the theoretical band diagram shown in Fig. 4.9, the 2-D MC with line defects exhibited a defect mode in the bandgap range of the defect-free 2-D MC. Fig. 4.11(c) and (d) shows the normalized differential insertion loss obtained from Fig. 4.11(a) and (b), respectively, at the frequency range of the bandgap. Clearly, at 8.46 and 9.28GHz, the transmitted power of the MSFVWs in the 2-D MC with line defects was higher than in the defect-free 2-D MC by 6.25 and 13.46dB, respectively. This experimental result has verified and demonstrated the guiding mode resulted from confinement of the MSFVWs in the 2-D MC with line defects.

4.4 Discussion

As presented in the previous sections, MC-based devices exhibit good frequency selectivity in microwave filters and superior performance in microwave phase shifters. Specifically, the tuning rates in the above-mentioned devices were demonstrated to be much larger compared to other magnetically-tuned microwave filters and phase shifters. Finally, confinement of MSFVWs in 2-D MCs by utilizing line defects, which is essential for development of guided-

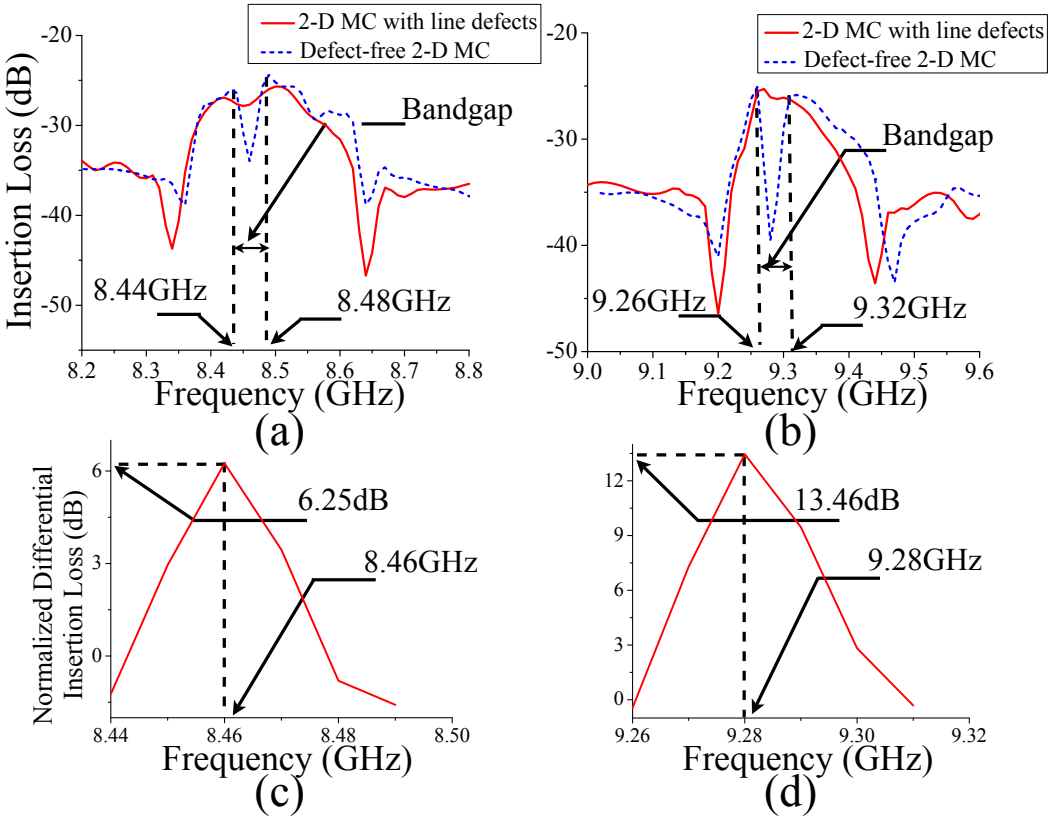

Figure 4.11: Measured insertion loss of the defect-free 2-D MC and the 2-D MC with line defects with the bias magnetic field of (a) 3000Oe and (b) 3275Oe. The normalized differential insertion loss in the bandgap regions are shown in (c) and (d), respectively.

MSW devices, was clearly demonstrated.

Chapter 5

Conclusion

The research of magnonic metamaterials is a new and emerging field. The MSVWs propagating in MCs possess the characteristics of short wavelengths (3 orders smaller than microwaves) and sensitive to bias magnetic fields. Therefore planar, miniature, and magnetically tunable devices are envisioned and constructed. In order to efficiently analyze the propagation characteristics of MSVWs in MCs, a new theoretical approach based on Walker's equation was developed and verified by experiments conducted on 1-D and 2-D MCs in YIG/GGG thin films. Excellent agreements between the theoretical and experimental results were obtained. Compared to the commercial softwares, e.g. HFSS, the simulation time required by this new theoretical approach to search for magnonic bandgaps is significantly reduced from days to minutes.

Tunable wideband microwave filters and phase shifters utilizing the 1-D and 2-D MCs in YIG/GGG thin films were explored subsequently. The bandgap arising from the periodic structure of the MC facilitates filtering function of a band stop filter (BSF) with good frequency selectivity. Thus the tunable band pass filter (BPF) with embedded BSF is realized based on the MCs. Large phase shifts at the frequency range close to bandgaps are predicted by the theoretical approach. Miniature and magnetically tunable microwave phase shifters were subsequently constructed. Superior phase tuning rate and phase shifts compared to other magnetically tuned phase shifters were demonstrated. The confinement of MSFVWs in line defects in 2-D MCs was clearly shown in the calculation and verified in the experiments. Note that confinement of the MSFVWs is the basis for other MC-based devices such as waveguides and resonators.

The complete theoretical analysis and demonstration of MC-based microwave devices as well as the device fabrication techniques established in the dissertation study should provide a valuable resource for further research and development in the new field on magnonic metamaterials.

Bibliography

[1] S. A. Nikitov, P. Tailhades, and C. S. Tsai. Spin waves in periodic magnetic structures - magnonic crystals. *Journal of Magnetism and Magnetic Materials*, 236(3):320–330, November 2001.

[2] Yu. V. Gulyaev, S. A. Nikitov, L. V. Zhivotovskii, A.A. Klimov, Ph. Tailhades, L. Presmanes, C. Bonningue, C. S. Tsai, S. L. Vysotskii, and Yu. A. Filimonov. Ferromagnetic films with magnon bandgap periodic structures: Magnon crystals. *Journal of Experimental and Theoretical Physics Letters*, 77(10):567–570, May 2003.

[3] S. A. Nikitov, C. S. Tsai, Y. V. Gulyaev, Y. A. Filimonov, A. I. Volkov, S. L. Vysotskii, and P. Taihades. YIG Thin Film-Based Two-Dimensional Magnonic and Magneto-Photonic Crystals. *Materials Research Society*, 834(Mc):1–10, 2005.

[4] V. Kruglyak and R. Hicken. Magnonics: Experiment to prove the concept. *Journal of Magnetism and Magnetic Materials*, 306(2):191–194, November 2006.

[5] Benjamin Lenk, Henning Ulrichs, Fabian Garbs, and Markus Mnzenberg. The building blocks of magnonics. *Physics Reports*, 507:107–136, June 2011.

[6] A. A. Serga, A. V. Chumak, and B. Hillebrands. YIG magnonics. *Journal of Physics D: Applied Physics*, 43(26):264002, July 2010.

[7] V. V. Kruglyak, S. O. Demokritov, and D. Grundler. Magnonics. *Journal of Physics D: Applied Physics*, 43(26):264001, July 2010.

[8] Sergej O. Demokritov and Andrei N. Slavin. *Magnonics: From Fundamentals to Applications* . Springer, 2013.

[9] Kai H. Chi, Yun Zhu, Rong W. Mao, James P. Dolas, and Chen S. Tsai. An approach for analysis of magnetostatic volume waves in magnonic crystals. *Journal of Applied Physics*, 109(7):07D320, March 2011.

[10] Kai H. Chi, Yun Zhu, Rong W. Mao, S. A. Nikitov, Y. V. Gulyaev, and Chen S. Tsai. Propagation Characteristics of Magnetostatic Volume Waves in One-Dimensional Magnonic Crystals with Oblique Incidence. *IEEE Transactions on Magnetics*, 47(9):3708–3711, 2011.

[11] Kai H. Chi, Yun Zhu, and Chen S. Tsai. Two-Dimensional Magnonic Crystal With Periodic Thickness Variation in YIG Layer for Magnetostatic Volume Wave Propagation. *IEEE Transactions on Magnetics*, 49(3):1000–1004, 2013.

[12] Eli Yablonovitch. Inhibited Spontaneous Emission in Solid-State Physics and Electronics. *Phys. Rev. Lett.*, 58(20):2059–2062, May 1987.

[13] Sajeev John. Strong localization of photons in certain disordered dielectric superlattices. *Phys. Rev. Lett.*, 58(23):2486–2489, Jun 1987.

[14] Yu. V. Gulyaev and A. A. Nikitov. Magnonic crystals and spin waves in periodic structures. *Doklady Physics*, 46(10):687–689, October 2001.

[15] V. Kruglyak. Spectrum of spin waves propagating in a periodic magnetic structure. *Physica B: Condensed Matter*, 339(2-3):130–133, December 2003.

[16] A. Kuchko, M. Sokolovskii, and V. Kruglyak. Spin wave spectrum of a magnonic crystal with an internally structured defect. *Physica B: Condensed Matter*, 370:73–77, October 2005.

[17] Rakesh P. Tiwari and D. Stroud. Magnetic superlattice with two-dimensional periodicity as a waveguide for spin waves. *Physical Review B*, 81(22):1–4, June 2010.

[18] J. O. Vasseur, L. Dobrzynski, B. Djafari-Rouhani, and H. Puszkarski. Magnon band structure of periodic composites. *Physical review. B, Condensed matter*, 54(2):1043–1049, July 1996.

[19] M. Krawczyk and H. Puszkarski. Plane-wave theory of three-dimensional magnonic crystals. *Phys. Rev. B*, 77:054437, 2008.

[20] Z. K. Wang, V. L. Zhang, H. S. Lim, S. C. Ng, M. H. Kuok, S. Jain, and A. O. Adeyeye. Observation of frequency band gaps in a one-dimensional nanostructured magnonic crystal. *Applied Physics Letters*, 94(8):083112, 2009.

[21] Sebastian Neusser, Bernhard Botters, and Dirk Grundler. Localization, confinement, and field-controlled propagation of spin waves in $Ni_{80}Fe_{20}$ antidot lattices. *Physical Review B*, 78(5), August 2008.

[22] G. Gubbiotti, S. Tacchi, G. Carlotti, N. Singh, S. Goolaup, A. O. Adeyeye, and M. Kostylev. Collective spin modes in monodimensional magnonic crystals consisting of dipolarly coupled nanowires. *Applied Physics Letters*, 90(9):092503, 2007.

[23] M. Krawczyk. Magnetostatic Waves in One-Dimensional Magnonic Crystals With Magnetic and Nonmagnetic Components. *IEEE Transactions on Magnetics*, 44(11):2854–2857, November 2008.

[24] Sebastian Neusser and Dirk Grundler. Magnonics: Spin Waves on the Nanoscale. *Advanced Materials*, 21(28):2927–2932, July 2009.

[25] S. Tacchi, M. Madami, G. Gubbiotti, G. Carlotti, H. Tanigawa, T. Ono, and M. Kostylev. Anisotropic dynamical coupling for propagating collective modes in a two-dimensional magnonic crystal consisting of interacting squared nanodots. *Physical Review B*, 82(2), July 2010.

[26] A. V. Chumak, A. A. Serga, S. Wolff, B. Hillebrands, and M. P. Kostylev. Design and optimization of one-dimensional ferrite-film based magnonic crystals. *Journal of Applied Physics*, 105(8):083906, 2009.

[27] Ki-Suk Lee, Dong-Soo Han, and Sang-Koog Kim. Physical Origin and Generic Control of Magnonic Band Gaps of Dipole-Exchange Spin Waves in Width-Modulated Nanostrip Waveguides. *Physical Review Letters*, 102(12), March 2009.

[28] Sang-Koog Kim, Ki-Suk Lee, and Dong-Soo Han. A gigahertz-range spin-wave filter composed of width-modulated nanostrip magnonic-crystal waveguides. *Applied Physics Letters*, 95(8):082507, August 2009.

[29] A. V. Chumak, A. A. Serga, B. Hillebrands, and M. P. Kostylev. Scattering of backward spin waves in a one-dimensional magnonic crystal. *Applied Physics Letters*, 93(2):022508, 2008.

[30] A. V. Chumak, P. Pirro, A. A. Serga, M. P. Kostylev, R. L. Stamps, H. Schultheiss, K. Vogt, S. J. Hermsdoerfer, B. Laegel, P. A. Beck, and B. Hillebrands. Spin-wave propagation in a microstructured magnonic crystal. *Applied Physics Letters*, 95(26):262508, 2009.

[31] A. V. Chumak, T. Neumann, A. A. Serga, and B. Hillebrands. Current-controlled dynamic magnonic crystal. *J. Phys. D: Appl. Phys.*, 42:1–4, 2009.

[32] Atsushi Maeda and Masami Susaki. Magnetostatic Wave Propagation in Yttrium-Iron-Garnet With Microfabricated Surfaces. *IEEE Transactions on Magnetics*, 42(10):3096–3098, November 2006.

[33] S. R. Seshadri. A transmission line model for magnetic waves on a thin film. *Journal of Applied Physics*, 60(5):1758, May 1986.

[34] T. Holstein and H. Primakoff. Field Dependence of the Intrinsic Domain Magnetization of a Ferromagnet. *Phys. Rev.*, 58(12):1098–1113, 1940.

[35] J. H. E. Griffiths. Anomalous High-frequency Resistance of Ferromagnetic Metals . *Nature*, 158:670–671, 1946.

[36] C. Kittel. On the Theory of Ferromagnetic Resonance Absorption . *Phys.Rev.*, 73(2):155–161, 1948.

[37] L. R. Walker. Magnetostatic Modes in Ferromagnetic Resonance . *Phys.Rev.*, 105(2):390–399, 1957.

[38] M.J. Hurben and C.E. Patton. Theory of Magnetostatic Waves for in-plane Magnetized Anisotropic Films. *Journal of Magnetism and Magnetic Materials*, 163(1-2):39–69, 1996.

[39] Charles Kittel. *Introduction to Solid State Physics, 8th Edition.* Wiley, 2004.

[40] David M. Pozer. *Microwave Engineering, 3rd Edition.* John Wiley Sons, Inc., Hoboken, New Jersey, 2004.

[41] Heisenberg W.

[42] Michael G. Cottam. *Linear and Nonlinear Spin Waves in Magnetic Films and Superlattices*. World Scientific, 1994.

[43] Daniel D. Stencil. *Spin Waves - Theory and Applications*. JSpringer Science+Business Media, LLC, 2009.

[44] L. R. Walker. Resonant Modes of Ferromagnetic Spheroids. *Journal of Applied Physics*, 29(3):318—-323, 1958.

[45] P. Röschmann and H Dötsch. Properties of Magnetostatic Modes in Femimagnetic Spheroids. *PHys. Stat. Sol. (b)*, 82(11):11–57, 1977.

[46] R. W. Damon and J. R. Eshbach. Magnetostatic modes of a ferromagnetic slab. *J. Phys. Chem. Solids*, 19(3/4):308–320, 1981.

[47] B. E. Storey, A. O. Tooke, A. P. Cracknell, and J. A. Przystawa. The determination of the frequencies of magnetostatic modes in rectangular thin films of ferrimagnetic yttrium iron garnet. *J. Phys. C: Solid St. Phys.*, 10:875–888, 1977.

[48] J. A. Duncant, B. E. Storey, A. O. Tooke, and A. P. Cracknell. Magnetostatic modes observed in thin single-crystal films of yttrium iron garnet at Q-band frequencies. *J. Phys. C: Solid St. Phys.*, 13:2079–2095, 1980.

[49] Yasuyuki Okamura, Masaya Ishida, and Sadahiko Yamamoto. Magnetooptic rib waveguides in YIG:an experiment. *Applied Optics*, 23(1):124–126, 1984.

[50] Akiyuki Tate Yujiro Katoh, Naoto Sugimoto and Atsushi Shibukawa. [110]-Directed Ridge Formation of Epitaxial Y3Fe5O12 Film Grown on [111]-oriented Gd3Ga5O12. *Jpn. J. Appl. Phys.*, 31(5B):L652–L654, 1992.

[51] Akiyuki Tate Naoto Sugimoto, Yujiro Katoh and Atsushi Shibukawa. Preparation of Substituted Y3Fe5O12 Waveguide Directional Coupler Using Ion-Beam Etching. *Jpn. J. Appl. Phys.*, 32(1A/B):L65–L67, 1993.

[52] Sang-yeob Sung, Xiaoyuan Qi, John Reinke, Samir K. Mondal, Sun Sook Lee, and Bethanie J. H. Stadler. Mater. res. soc. symp. proc. volume 834, pages J4.2.1–6, 2005.

[53] Yun Zhu, Gang Qiu, K. H. Chi, B. S. T Wang, and C. S. Tsai. A Tunable X-Band Band-Pass Filter Module Using YIG/GGG Layer on RT/Duroid Substrate. *IEEE Transactions on Magnetics*, 45(10):4195–4198, 2009.

[54] Chen S. Tsai and Gang Qiu. Wideband Microwave Filters Using Ferromagnetic Resonance Tuning in Flip-Chip YIG-GaAs Layer Structures. *IEEE Transactions on Magnetics*, 45(2):656–660, 2009.

[55] Yun Zhu, Gang Qiu, K. H Chi, B. S .T Wang, and C. S. Tsai. A Compact X-Band Tunable Bandpass Filter Module Using a Pair of Microstrip Composite Bandpass Filters in Cascade. *IEEE Transactions on Magnetics*, 46(6):1424–1427, 2010.

[56] Yun Zhu, Rong W. Mao, and Chen S. Tsai. A Varactor and FMR-Tuned Wideband Band-Pass Filter Module With Versatile Frequency Tunability. *IEEE Transactions on Magnetics*, 47(2):284–288, 2011.

[57] W. S. Ishak. Magnetostatic surface wave devices for UHF and L band applications. *IEEE Trans. Magn.*, MAG-19:1880–1882, 1983.

[58] Y. Zhu, K. H. Chi, and C. S. Tsai. Magnonic Crystals-Based Tunable Microwave Phase Shifters. *Applied Physics Letters*, 105(2):022411, 2014.

[59] Hoton How, Wei Hu, Carmine Vittoria, Leo C Kempel, and Keith D Trott. *Journal of Applied Physics*, 85(8):2–4, 1999.

[60] J.D. Adam, L.E. Davis, G.F. Dionne, E.F. Schloemann, and S.N. Stitzer. *IEEE Transactions on Microwave Theory and Techniques*, 50(3):721–737, 2002.

[61] Xu Zuo, Ping Shi, S. A. Oliver, and C. Vittoria. *Journal of Applied Physics*, 91(10):7622, 2002.

[62] T. J. Fal and R. E. Camley. *Journal of Applied Physics*, 104(2):023910, 2008.

[63] Anton L Geiler, Jianwei Wang, Jin Sheng Gao, Soack Dae Yoon, Yajie Chen, and Vincent G Harris. *IEEE Transactions on Magnetics*, 45(10):4179–4182, 2009.

[64] Zihui Wang, Young-Yeal Song, Yiyan Sun, Joshua Bevivino, Mingzhong Wu, V. Veerakumar, Timothy J. Fal, and Robert E. Camley. *Applied Physics Letters*, 97(7):072509, 2010.

[65] J. H. Leach, H. Liu, V. Avrutin, E. Rowe, U. Ozgur, H. Morkoc, Y.-Y. Song, and M. Wu. *Journal of Applied Physics*, 108(6):064106, 2010.

[66] Bijoy K. Kuanr, T. J. Fal, Z. Celinski, and R. E. Camley. *Journal of Applied Physics*, 111(7):07A508, 2012.

[67] Yun Zhu, Gang Qiu, and Chen S. Tsai. *Journal of Applied Physics*, 111(7):07A502, 2012.

[68] C.Y. Zhu, H. Liu, V. Avrutin, C.Z. Lu, U. Ozgur, and H. Morkoc. *Electronics Letters*, 48(9):508, 2012.

[69] M.A Popov, I. V. Zavislyak, and G. Srinivasan. *Progress In Electromagnetics Research C*, 25(November 2011):145–157, 2012.

[70] Xi Yang, Jing Wu, Yuan Gao, Tianxiang Nan, Ziyao Zhou, Shawn Beguhn, and Nian X Sun. *IEEE Transactions on Magnetics*, 49(7):3882–3885, 2013.

[71] K. H. Chi, Y. Zhu, and C. S. Tsai. Confinement of Magnetostatic Forward Volume Waves in Two-Dimensional Magnonic Crystals with Line Defects. *Journal of Applied Physics*, 115(17):17D125, May 2014.